

Effects of surface properties and loaded nanoparticles on the evaporation of sessile droplets

By

ZHIHAO ZHANG

Thesis submitted to the University of Nottingham for the degree of

Doctor of Philosophy

September, 2024

Abstract

Droplet evaporation is one of the most common physical processes in nature. Maxwell was the first scientist to deduce the equations of droplet evaporation based on the diffusion process in the still air in 1877. In recent decades, droplet evaporation has been getting more and more attention from researchers since the coffee-ring effect was discovered and explained by Deegan in 1997. Nowadays, the physical phenomenon of droplet evaporation is used widely in various industrial and scientific fields, such as photoresist surfaces, spray cooling, inkjet printing, biofluid diagnostics, DNA screening, forensics, chemical screenings, and crystal fabrication. Therefore, it is essential to reveal the mechanism of the factors which could affect the droplet evaporation dynamics and sedimentary pattern.

Although sessile droplet evaporation is a simple phenomenon to observe from the outside, it contains complicated internal physical mechanisms. Therefore, the research methods in this thesis would span from the mesoscopic scale to the macro scale for different research issues, making it more comprehensive to analyse the overall evaporation process. This thesis uses experimental research as the main research method to study the two parts that affect the evaporation process of sessile droplets: substrate surface properties (solid) and liquid properties (liquid). For surface characteristics, due to the wide application of biomimetic functional surfaces, research on the design of bionic surfaces has gradually received attention. The microstructure and surface roughness play critical roles in affecting the droplet wettability and evaporation dynamics, but the precise relationship between them still needs more research. So, in this thesis, The mechanism by which the arrangement and design of

biomimetic surface microstructures affect droplet evaporation dynamics will be clarified. Besides, the nanofluid droplet will also be studied in the thesis owing to the nanofluid's wide application in industrial and scientific research. In recent studies on the evaporation of nanofluid droplets, it can be found that the mechanism of the effect of loaded nanoparticles on the interfacial heat and mass transfer process needs to be more clearly described. Based on the considerable application value of advanced functional carbon materials in fields such as energy and electronics, the influence mechanism of carbon-based nanoparticles, such as carbon nanotubes and graphene, on the droplet evaporation process should be explored urgently. In addition to measuring the heat and mass transfer processes at the interface and triple line positions during the evaporation of sessile droplets, this thesis also explores the regulatory mechanism of the deposition pattern of droplets loaded with nanoparticles, such as the promotion or inhibition of the coffee ring effect, which has essential research significance in fields such as inkjet printing and flexible electronic device preparation.

Over the past few decades, researchers have invested a lot of effort in studying the effects of various factors on the evaporation process of sessile droplets. Even so, these issues have not been fully revealed to this day. Therefore, the research topics of this thesis are mainly reflected in the influence mechanism of droplet evaporation dynamics, the heat and mass transfer process at the liquid-vapour interface, and the analysis of nanoparticle deposition patterns, which aims to provide help and guidance for solving these problems.

Acknowledgements

I want to thank my supervisor, Professor. Yan Yuying, for his great help in research direction and methodology. It was his guidance that led me into this fascinating research field. It is my most extraordinary luck to meet him on the road of scientific research, and I will never forget his concern for my life and career, as well as his platform and support as much as possible. I admire his passion, persistence in sports, and positive attitude towards life. I would also like to thank Dr Mark Alston for always encouraging me and supporting my work, and his humour is impressive. Dr Zheng Xiaofeng also helped me immensely; his optimistic attitude has always influenced me. In addition, I would like to thank Professor. Khellil Sefiane for his guidance. I have significantly benefited from his profound knowledge of the professional field.

At this point, my graduation project and thesis have ended. I have many things and people I want to thank. Without them, I would not have grown to where I am now. In particular, I want to thank my group members and visiting scholars, who gave me the perseverance to overcome all difficulties when I was in trouble. Finally, I would like to thank my parents for their understanding and support. Your care in life and spiritual encouragement are my motivation for studying.

Table of Contents

Abstract i

Acknowledgements iii

Table of Contents iv

List of Publications viii

List of Figures ix

List of Tables xiii

Chapter 1. Introduction 14

1.1 Background 14

1.2 Research methodology 17

1.2.1 Research methods on the influence of surface roughness and structure 17

1.2.2 Research methods on the influence of nanofluid 19

1.3 Research aim and objectives 21

1.3.1 Research aims 21

1.3.2 Research objectives 22

Chapter 2. Literature review 25

2.1 Physical description of droplet interface 25

2.1.1 Liquid-vapour interface 25

2.1.2 Liquid-solid interface 26

2.1.3 Contact line region 30

2.2 Basic physical process of droplet evaporation 33

2.2.1 Marangoni flow and buoyancy convection 33

2.2.2 Evaporative cooling effect 34

2.2.3 Diffusion and Stefan flow 35
2.3 Effect of contact surface on evaporation characteristics of sessile droplets 37
2.3.1 Hydrophobicity of substrate surface 37
2.3.2 surface roughness and topography 42
2.3.3 Internal thermal conductivity and external heating of the substrate 47
2.3.4 Other kind of substrate properties 50
2.4. Effect of liquid properties on evaporation characteristics of sessile droplets 52
2.4.1 Evaporation process of droplets loaded with nanoparticles 53
2.4.2 Evaporation process of a droplet with added surfactant 57
Chapter 3. Effect of photoresist microstructure arrangement on droplet evaporation dynamics 61
3.1 Chapter introduction 61
3.2 Materials and experimental setup 62
3.3 Results and discussion 67
3.3.1 Effect of surface biomimetic pillar arrangement on droplet wetting properties 67
3.3.2 Effect of surface biomimetic pillar height on droplet wetting properties 72
3.3.3 Effect of surface roughness on droplet heat and mass transfer process 79
3.4 Chapter summary 85
Chapter 4. Effect of the photoresist microstructure configuration on droplet evaporation dynamics 88
4.1 Chapter introduction 88
4.2 Material and experimental setup 89
4.3 Results and discussion 93
4.3.1 Effect of microstructure configuration on droplet wetting performance 93

4.3.2 Effect of microstructure arrangement on biomimetic surface wettability 98
4.3.3 Effect of microstructure arrangement on interfacial heat transfer 102
4.4 Chapter summary 108
Chapter 5. Effect of surface roughness on silica nanoparticle-laden droplet evaporation dynamics 110
5.1 Chapter introduction 110
5.2 Experimental setups and methodology 111
5.2.1 Substrate surface preparation 112
5.2.2 Silica nanofluid preparation 114
5.3 Results and Discussion 114
5.3.1 The effect of surface roughness on the droplet wettability 114
5.3.2 The effect of surface roughness on the droplet interfacial heat transfer 122
5.3.3 The effect of surface roughness on the nanofluid droplet sedimentary pattern 126
5.4 Chapter summary 131
Chapter 6. Effect of loaded carbon-based nanoparticles on the evaporation dynamics of sessile droplets 134
6.1 Chapter introduction 134
6.2 Experimental methods 135
6.2.1 Experimental setup 135
6.2.2 Nanofluid preparation 136
6.3 Results and discussion 137
6.3.1 Effect of different carbon-based nanoparticles on the heat and mass transfer process 137
6.3.2 Effect of substrate temperature on the droplet evaporation dynamics 145

6.3.3 Macroscopic effects of carbon-based materials on the sedimentary pattern 154

6.4 Chapter summary 159

Chapter 7. Conclusion and outlook 161

7.1 Conclusion 161

7.2 Outlook 164

Reference 166

List of Publications

1. **Zhang, Z.,** Wang, X., & Yan, Y. (2021). A review of the state-of-the-art in electronic cooling. **e-Prime-Advances in Electrical Engineering, Electronics and Energy**, 1, 100009.

2. **Zhang, Z.**, Yan, Y., & Magnini, M. (2023). An experimental investigation of the effect of surface roughness on sessile droplet evaporation. **In International Heat Transfer Conference Digital Library**. Begel House Inc.3.

3. **Zhang, Z.**, & Yan, Y. (2024). The effect of surface roughness on sessile droplet evaporation dynamics of silica nanofluid. **International Journal of Heat and Mass Transfer**, 234, 126156.

4. **Zhang, Z.**, & Yan, Y. (2024). Effect of loaded carbon-based nanoparticles on the evaporation dynamics of sessile droplets. **International Journal of Thermal Sciences**. (Under review).

5. **Zhang, Z.**, & Yan, Y. (2024). Effect of photoresist biomimetic surface roughness on droplet evaporation dynamics. **Journal of Bionic Engineering**. (Under review).

6. **Zhang, Z.**, & Yan, Y. (2024). Effect of photolithographic biomimetic surface microstructure on wettability and droplet evaporation process. **Biomimetics**. (Accepted)

List of Figures

Fig. 1. 1 (a) Number of articles published with “droplet” and “evaporation” as keywords from 2011 to 2020 based on the database of Scopus®. (b) classification of factors affecting the evaporation process of the sessile droplet. 14
Fig. 1. 2 The schematic diagram of the research plan process about the influence of surface roughness and patterned surface..... 19
Fig. 1. 3 The schematic diagram of the research plan process about the influence of surface roughness and patterned surface..... 21
Fig. 2. 1 The balance of droplet surface tension based on Young’s equation……28
Fig. 2. 2 The different wetting conditions of sessile droplets..... 29
Fig. 2. 3 Schematic of two kinds of sessile droplet wetting phenomenon based on the non-ideal solid surface: (a) Wenzel's model; (b) Cassie–Baxter model. 30
Fig. 2. 4 Schematic diagram of the study area and scaling of the contact line region..... 31
Fig. 2. 5 Schematic diagram of droplet evaporation modes: (a) CCA mode; (b) CCR mode; (c) SS mode. 33
Fig. 2. 6 Contour picture of the temperature distribution and vapour mass fraction with a streamline of the evaporating droplet when the contact angle (CA) and the substrate temperature (Tw) is (a) CA = 10°, Tw = 45.6℃; (b) CA = 70°, Tw = 45.6℃; (c) CA = 110°, Tw = 40℃ [97]. 39
Fig. 2. 7 (a) Schematic diagram of droplet spreading and wicking on the surface of the nanowire; (b) electron microscope image of irregular nanowires; (c) electron microscope image of regular nanowires [115] 41
Fig. 2. 8 Three-dimensional shape around the static contact line at the nanometer scale photo by helium ion microscopy [138] 47
Fig. 2. 9 Droplet evaporation process on the (a) hydrophilic surface and (b) superhydrophobic surfaces with two kinds of temperature gradients (ΔT) [155] 49
Fig. 2. 10 the evaporation process of the same volume of the water droplet on the (a) dry and (b) LCS surface [167]..... 51
Fig. 2. 11 Schematics of particle behaviour in a droplet at (a) low and (b) high concentration [194]. .. 56
Fig. 2. 12 schematic about the influence mechanism of surfactants on droplet wetting and pinning [26]. 60
Fig. 3. 1 Experimental process and equipment schematic diagram……63
Fig. 3. 2 (a) Plant surfaces or animal skins with unique surface properties in nature; (b) Photoresist micro-pillar preparation process based on photolithography; (c) Different biomimetic surfaces under the microscope; (d) Biomimetic surface profile measured by an optical profilometer..... 65
Fig. 3. 3 Changes of contact angle and dimensionless contact diameter of (a) 0.25 μL; (b) 0.5 μL; (c) 0.75 μL; (d) 1.0 μL DI water droplet on biomimetic surfaces over time..... 69

Fig. 3. 4 Variation of work of adhesion (WPLS) with (a) 0.25 μL; (b) 0.5 μL; (c) 0.75 μL; (d) 1.0 μL DI water droplets on different biomimetic surfaces over time. 72
Fig. 3. 5 Changes of contact angle and dimensionless contact diameter of (a) 0.25 μL; (b) 0.5 μL; (c) 0.75 μL; (d) 1.0 μL DI water droplet on biomimetic surfaces over time. 75
Fig. 3. 6 Variation of work of adhesion (WPLS) with (a) 0.25 μL; (b) 0.5 μL; (c) 0.75 μL; (d) 1.0 μL DI water droplets on different biomimetic surfaces over time. 77
Fig. 3. 7 (a) Changes in the initial equilibrium contact angles of droplets of different volumes on biomimetic surfaces with roughness degrees; (b) the work of adhesion corresponding to different initial equilibrium contact angles. 79
Fig. 3. 8 The temperature difference between the central and contact line region of (a) 0.25 μL; (b) 0.5 μL; (c) 0.75 μL; (d) 1.0 μL droplet on different biomimetic surfaces. 82
Fig. 3. 9 Evolution of the temperature distribution at the liquid-vapour interface of a 0.5 μL droplet on the (a) PBS-SH1, (b) PBS-SH3, and (c) PBS-S3 surfaces. 83
Fig. 3. 10 Average evaporation rate of (a) 0.25 μL; (b) 0.5 μL; (c) 0.75 μL; (d) 1.0 μL droplet located on different biomimetic surfaces. 85
Fig. 4. 1 Bio-inspired preparation process of biomimetic functional surface……..……...90
Fig. 4. 2 Photoresist biomimetic surface production process. 91
Fig. 4. 3 Changes of contact angle and contact line of a 1.0 μL droplet on SS-1 and CS-3 surfaces at a substrate temperature of (a) 50°C; (b) 60°C; (c) 70°C; (d) 80°C. 96
Fig. 4. 4 (a) Dimensionless height of a 1.0 μL droplet over time for different surfaces and substrate temperatures; (b) Initial equilibrium contact angle of a 1.0 μL droplet on different surfaces and substrate temperatures. 98
Fig. 4. 5 Changes of contact angle and contact line of a 1.0 μL droplet on different surfaces at a substrate temperature of (a) 50°C; (b) 60°C; (c) 70°C; (d) 80°C. 100
Fig. 4. 6 (a) The initial equilibrium contact angle of the droplet changes under different surface and substrate temperature conditions; (b) The initial adhesion work of the droplet changes under different surface and substrate temperature conditions. 102
Fig. 4. 7 Temperature distribution of the droplet liquid-vapour interface on the CS-3 and SS-3 surfaces at different periods when the substrate temperature is (a) 50 °C and (b) 80 °C. 103
Fig. 4. 8 When the substrate temperature of the CS-3 surface is (a) 50°C, (c) 60°C, (e) 70°C, (g) 80°C, the temperature distribution at the centre-line of the droplet liquid-vapour interface at different periods; when the substrate temperature of the SS-3 surface 106
Fig. 4. 9 (a) Temperature difference at the droplet liquid-vapour interface in the initial state under different surface and substrate temperature conditions; (b) Variation of the overall average evaporation rate of the droplet with the surface and substrate temp 108
Fig. 5. 1 The optical profiling of the sample surface.……..……...…111
Fig. 5. 2 Evolution of the contact angle of a sessile droplet with a volume of (a) 2, (b) 4, (c) 6, (d) 8 μL when located on substrates with different roughness. 117

Fig. 5. 3 The height shrinkage process of the (a) 2 μL, (b) 4 μL, (c) 6 μL, and (d) 8 μL droplets. 119
Fig. 5. 4 Variation of adhesion work at the liquid-solid interface of a (a) 2 μL; (a) 4 μL; (a) 6 μL; (a) 8 μL droplet during evaporation. 122
Fig. 5. 5 The temperature change of the droplet top region T_{top} with time and the maximum temperature difference in liquid-vapour interface $T_{diff,max}$ when the droplet volume is (a) 2 μL; (b) 4 μL; (c) 6 μL; (d) 8 μL. 125
Fig. 5. 6 The evolution of interface temperature distribution of (a) 2 μL; (b) 4 μL; (c) 6 μL; (d) 8 μL droplet on the S4 surface with time. 125
Fig. 5. 7 The sedimentary pattern after the evaporation of 2 μL silica nanofluid droplet on the (a) S1, (b) S2, (c)S3, and (d)S4 surfaces, respectively. 127
Fig. 5. 8 Dimensionless height of the cross-section of the sedimentary ring after evaporation of a 2 μL silica nanofluid droplet on the (a) S1, (b) S2, (c) S3, (d) S4 surface. 129
Fig. 5. 9 Microscope images of the sedimentary coffee-ring patterns of (a) 4; (b) 6; and (c) 8 μL silica nanofluid droplets placed on the S4 surface; Microscope images of the sedimentary coffee-ring patterns of (d) 4; (e) 6; and (f) 8 μL silica nanofluid droplets placed on the S1 surface; (g) and (h) is the optical profile of the selected area. 131
Fig. 6. 1 Changes in contact angle and contact line during evaporation for (a) 0.5 μL, (b) 1.0 μL, (c) 1.5 μL DI water, MWCNTs, and MLG nanofluid droplets and (d) the carbon-based nanoparticles comparison. 140
Fig. 6. 2 Temperature difference at the edge and top of liquid-vapour interface of (a) 0.5 μL, (b) 1.0 μL, (c) 1.5 μL DI water, MWCNTs, and MLG nanofluids with time. 143
Fig. 6. 3 (a) 0.5 μL, (b) 1.0 μL, (c) 1.5 μL droplet dimensionless volume changes with time of DI water and carbon-based nanofluid, (d) the average evaporation rate of DI water and carbon-based nanofluid droplet with different volume. 145
Fig. 6. 4 Changes in contact angle and contact line of 0.5 μL (a) DI water and (b) carbon-based nanoparticle-laden droplets during evaporation. 147
Fig. 6. 5 Changes in contact angle and contact line of 1.0 μL (a) DI water and (b) carbon-based nanoparticle-laden droplets during evaporation. 149
Fig. 6. 6 Changes in contact angle and contact line of 1.5 μL (a) DI water and (b) carbon-based nanoparticle-laden droplets during evaporation. 149
Fig. 6. 7 Based on different substrate temperatures, the maximum temperature difference between the top and edge of (a) 0.5 μL, (b) 1.0 μL, (c) 1.5 μL DI water droplet, (d) 0.5 μL, (e) 1.0 μL, (f) 1.5 μL MWCNTs nanofluid droplet, and (g) 0.5 μL, (h) 1.0 μL, (i) 1.5 μL MLG nanofluid droplet. 152
Fig. 6. 8 Dimensionless volume changes under different substrate temperatures of (a) 0.5 μL, (b) 1.0 μL (c) 1.5 μL DI water and carbon-based nanofluid droplets, (d) the average evaporation rate of DI water and carbon-based nanofluid droplets with different volume and temperature conditions. 154
Fig. 6. 9 When the substrate temperature is 50 °C, the sedimentary pattern of (a) 0.5 μL, (b) 1.0 μL, (c) 1.5 μL MLG nanofluid droplets, and (d) 0.5 μL, (e) 1.0 μL; (f) 1.5 μL MWCNTs nanofluid droplets. 156

Fig. 6. 10 Effect of the deposition distribution of (a) MWCNTs nanoparticles and (b) MLG nanoparticles on the surface roughness of regions 1-4 under different volume conditions. 157
Fig. 6. 11 Under different volume conditions, the sedimentary patterns of MLG nanofluid droplets when the substrate temperature is (a) 60 °C, (c) 70 °C, (e) 80 °C, and the sedimentary patterns of MWCNTs nanofluid droplets when the substrate temperature is (b) 60 °, (d) 70 °C, (f) 80 °C. 158
Fig. 6. 12 Variation trend of average surface roughness inside and outside the coffee ring in the deposition pattern of (a) 0.5 μL, (b) 1.0 μL, (c) 1.5 μL droplets under different substrate temperature conditions. 159

List of Tables

Table 2. 1 The summary of the water droplet evaporation process is based on different wettability. 40

Table 2. 2 The summary of substrate surface topographies commonly used. 44

Table 2. 3 Summary of materials commonly used for droplet evaporation considering the thermal conductivity·····48

Table 2. 4 Summary of nanofluid droplet commonly used (unless noted specifically, all solvent is water). 55

Table 3. 1 Parameters of biomimetic surface photoresist micro-pillars·····65

Table 3. 2 Some physical properties of the DI water under the condition of 60℃ 65

Table 4. 1 Basic physical properties of photoresist SU-8 2010·····90

Table 4. 2 Biomimetic surface microstructural parameters. 91

Table 4. 3 Physical properties of deionized water at different temperatures 93

Table 5. 1 Surface roughness measurement data of copper disc samples·····113

Table 6. 1 Silicon wafer polishing surface parameters·····136

Table 6. 2 Basic physical parameters of nanoparticles 136

Chapter 1. Introduction

1.1 Background

Droplet evaporation is one of the most common physical processes in nature, and Maxwell was the first scientist who based on the diffusion process in the still air to deduce the equations of droplet evaporation in 1877 [1]. In recent decades, droplet evaporation has been getting more and more attention from researchers since the coffee-ring effect was discovered and explained by Deegan et al. [2] in 1997. Nowadays, the physical phenomenon of droplet evaporation is used widely in various industrial and scientific fields, such as photoresist surfaces [3], spray cooling [4], inkjet printing [5], biofluid diagnostics [6], DNA screening [7], forensic [8], cell and chemical screenings [9], crystal fabrication [10], etc. As shown in Fig. 1.1 (a), the number of scientific papers published in the field of droplet evaporation has increased continuously in the last ten years, as archived in the Scopus database. In the foreseeable future, there will also be more scientific researchers carrying out studies on the process of droplet evaporation in various fields such as physics, chemistry, engineering, biology, medicine, etc.

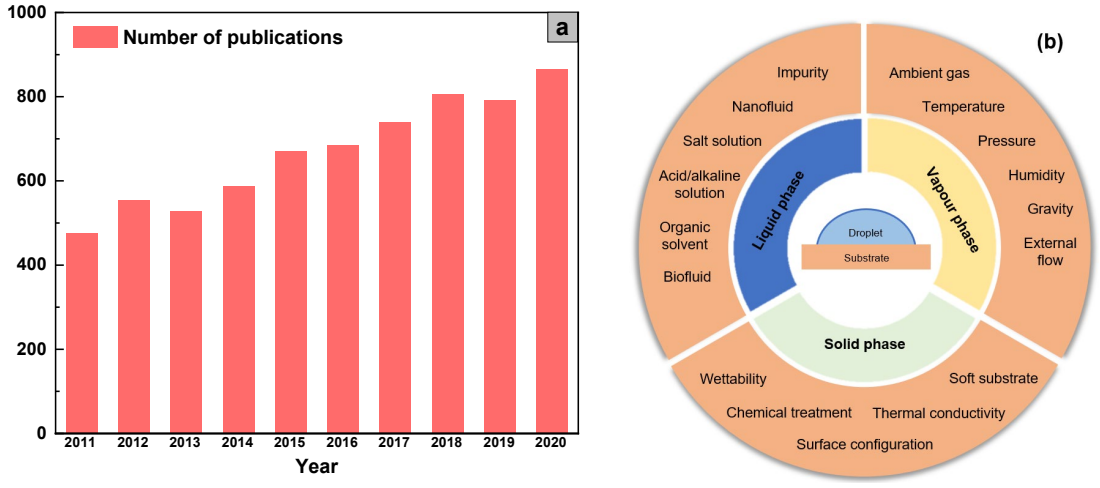


Fig. 1. 1 (a) Number of articles published with "droplet" and "evaporation" as keywords from 2011 to

2020 based on the database of Scopus®. (b) classification of factors affecting the evaporation process of the sessile droplet.

The physical phenomenon of droplet evaporation involves lots of physical processes. From the perspective of thermofluids, the process of sessile droplet evaporation could be divided into the heat and mass transfer process in its inside and interface position. Except for the inside droplet fluid flow and heat transfer processes, such as Marangoni flow and buoyant convection, need lots of physical mechanisms to explain. The research of droplet interfacial heat and mass transfer has always been a complex cross-scale behaviour and multidisciplinary study. Like the quote said by the Austrian scientist and 1945 Nobel Physics prize winner Pauli, "God made the bulk; surfaces were invented by the Devil" [11]. So, surface and interface science research is a huge challenge and significant in studying droplet evaporation. Physical chemistry and condensed-matter physics were the origins of surface science, and they could be applied to analysing the interface characteristics and surface chemical reactions nowadays [12]. For the sessile droplet evaporation, the liquid-solid interface, liquid-vapour interface and triple line (liquid-solid-vapour interface) are the main research objects in heat and mass transfer. For the liquid-solid interface, the wetting phenomenon research has attracted a lot of attention [13]. The research on wetting and wettability has been carried out for more than 200 years by British scientist Young [14] and French scientist Laplace [15]. And the wetting state could be well described by the Wenzel model and Cassie-Baxter model. The influence of wettability, such as hydrophobic and hydrophilic surface, on the sessile droplet evaporation also has been studied a lot, but it is still a complicated question. Under different surface wettability, the sessile droplet would

appear at different contact angles and profiles. The movement of the contact line would also be changed, so the process of internal flow, heat transfer, and liquid-vapour interface diffusion during droplet evaporation would be influenced, which increase the difficulty of research greatly. Except for the wettability of the solid surface, as shown in Fig. 1.1 (b), the solid surface configuration such as topography and chemical treatment, all would affect the wetting phenomenon and then influence the sessile droplet evaporation process [16, 17]. The thermal conductivity of the substrate could also affect the sessile droplet evaporation process [18]. Simultaneously, the droplet characteristics will also have a significant impact on its wetting and evaporation process. In this thesis, pure water is mainly used as a solvent, and the solute for the pure sessile droplet is divided into solid and liquid solutes, as seen in Fig. 1.1 (b). Although some solutes are soluble in water and some are insoluble, both could affect the liquid-vapour interface diffusion rate, movement of the contact line, and the internal flow mode. Besides, the influence mechanism of solutes on the coffee-ring effect, which is significant in manufacturing, has also been studied in depth [19], which could guide the development of coffee-ring effect suppression [20] and self-assembly technology [21]. For the liquid solutes, the concentration would affect the sessile droplet evaporation kinetics. Besides, for the different volatility of the solution and solutes, the influence of evaporation order on the evaporation rate also needs to be considered [22]. The surfactant solutions also attracted many researchers to study due to their significant application value in droplet drying and sediment control [23]. The presence of surfactants affects the evaporation rate of the sessile droplet and the surface tension of the liquid-vapour interface [24]. The pinning and depinning of the triple line also could be influenced [25]. Nowadays, the influence of surfactants on evaporation kinetics

would appear contrary conclusion, the current issues in this field are still under discussion and try to explain perfectly [26]. Besides, biofluid evaporation such as blood or protein solutions also gained more attention in the last decades [27]. Its non-Newtonian fluid properties also pose many challenges to research [28], revealing the mechanism of sediment pattern is of great help to medical diagnosis. Except for some thermodynamic parameters of the vapour phase, the change of gravity has also been proven to affect the sessile droplet evaporation process [29]. Besides, it is worth saying that the research on droplet evaporation could also have a guiding role in preventing and controlling the spread of COVID-19 [30]. Naturally, as a fluid flow and diffusion problem, external airflow could also influence the evaporation kinetics obviously [31], and the sessile droplet evaporation under different kinds of ambient gas will also be discussed and reviewed in this thesis. So far, there have been a lot of studies discussing sessile droplet evaporation. However, the research on heat and mass transfer at the interface of sessile droplets during evaporation from the perspective of bionic microstructure surfaces and the classification of loaded carbon-based nanoparticles still needs to be supplemented and deepened.

1.2 Research methodology

1.2.1 Research methods on the influence of surface roughness and structure

For the influence of surface properties on the sessile droplet evaporation, as shown in Fig. 1.2, the two key issues are paramount: i) the fabrication of the roughness and patterned surface with different kinds of wettability; ii) the surface properties observation and measurement. Several surface factors need to be considered for the

fabrication of the surface. The first kind of surface is the rough surface, which would be fabricated by the grinding & polishing mechanic and sandpaper, and the operation and process would follow the standard specifications. The material of the rough surface would be a regular metal sheet like copper, and the heated condition would also be considered. Secondly, wettability also played an essential role in studying sessile droplet evaporation. A way to control hydrophobicity precisely is through surface micro-treatment processing. As shown, it could design and fabricate the microstructures on the surface, which would obtain a series of surfaces with different kinds of wettability. So, these surface properties would provide ample options for studying the effect of surface material, roughness, and configuration on the sessile droplet wettability and evaporation dynamics. For these kinds of surfaces, the rough surface would be fabricated in the group's lab, and the structured surface and biomimetic microstructures would be designed by us and fabricated through cooperation with the other departments or universities.

Meanwhile, except for the design and fabrication of the surface, the measurement of the surface characteristics is also very important for analysing the relationship between the sessile droplet evaporation dynamics and the critical parameters of the surface, which would be helpful for future surface design and revealing the fundamental factors and laws that affect the evaporation process. As shown below, the key parameters that need to be known in the study plan are the roughness degree, contact angle (surface wettability), micro-structure parameters, and pattern shape & ratio. The contact angle and surface energy would be observed and calculated in the Lab, and the other parameters could be measured in the nmRC centre of the University of Nottingham,

which could make the nano- & micro-scale imaging and compositional analysis like atomic force microscopy (AFM) and Zeta Profilometer. Therefore, the surface characteristics would be measured and fabricated with the design.

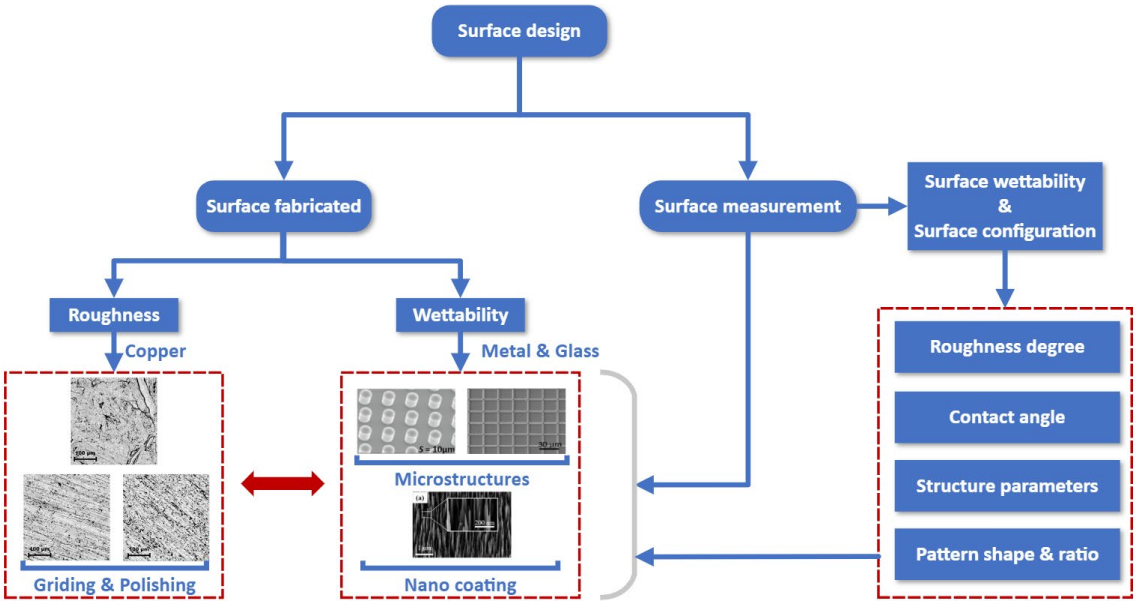


Fig. 1. 2 The schematic diagram of the research plan process about the influence of surface roughness and patterned surface.

1.2.2 Research methods on the influence of nanofluid

Then, as mentioned above, the nanoparticles (nanofluid) also have a significant impact on the sessile droplet evaporation. For the study of the effect of nanofluid on the sessile droplet evaporation, there would be an effective way to divide the influencing factors into nanoparticles type and based fluids type, as shown in Fig. 1.3, the study of the effect of nanofluid on the sessile droplet evaporation dynamics would be based on the surface effect firstly, it means the influence of surface would be unified, so the effect of wettability, thermal conductivity, and surface energy would not need to be considered on the nanofluid droplet evaporation study. For the nanoparticle type, nanomaterials

that are currently widely used and have excellent application prospects will be used, such as carbon-based nanoparticle carbon nanotube, and graphene (or graphene oxide). These kinds of nanoparticles are easy to get and sufficient to cover industry and scientific research applications. Especially for the graphene-based nanofluid droplet, it would have some unique thermal and evaporation dynamics characteristics owing to graphene's remarkable properties. The graphene-based nanofluid droplet's rheological behaviour and dynamic viscosity would also deserve to be studied. At the same time, the based fluid of the nanofluid would also have a significant effect on the sessile nanofluid droplet evaporation dynamics. In the research plan, surfactants are also included in the study in addition to deionized water (DI water). The surfactant also has a huge influence on droplet stability, and research about its effect on the nanofluid droplet evaporation process is now hotly pending. The parameter of adding surfactant would also be used as an adjustment to control the effect of nanoparticles and fluid concentration on the evaporation process.

Meanwhile, the nanofluid sessile droplet would have a unique fluid mechanism characteristic compared to the pure water droplet. As shown in Fig. 1.3, the evaporation dynamics, sediment analysis, and inside nanoparticle movement will be studied in the research plan. Firstly, the evaporation dynamics is an essential issue for the study plan, and the unique thing that needs to be considered is that the nanofluid can sometimes exhibit shear thickening behaviour. The physical properties would differ, so the evaporation dynamics would not rely on previous studies. Secondly, the sediment pattern and inside particle movement are unique phenomena for nanofluids to study. The measurement of the sediment and movement would use the camera to record; the

critical issue is to describe or predict the sediment pattern and movement of the nanoparticles during the evaporation process based on the different kinds of surface wettability, nanoparticles, and fluids. For the study of nanofluid sessile droplet evaporation, the physical properties measure is also a critical issue that needs to be handled owing to its effect on the theoretical analysis, and these kinds of properties of the nanofluid still also be measured in the Lab or cooperated with the nmRC centre of the UoN.

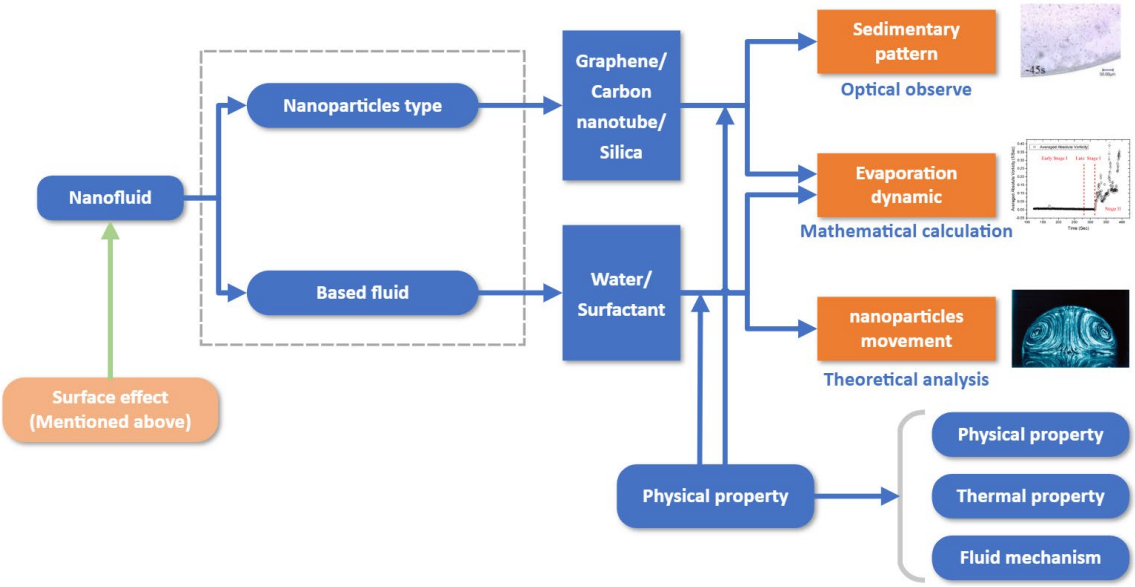


Fig. 1. 3 The schematic diagram of the research plan process about the influence of surface roughness and patterned surface.

1.3 Research aim and objectives

1.3.1 Research aims

Based on the previous introduction, it could be seen that a lot of work has been done to reveal the law of sessile droplet evaporation dynamics and the factors that could have a huge effect on the process. The research papers on droplet evaporation have been

rising for decades. The reason for this would mainly be that the droplet evaporation processes have a considerable application background in the industrial and scientific fields, which have also been introduced in detail in the introduction of this review. However, until now, the process of sessile droplet evaporation still has not been understood completely, owing to the problematic and complex physical law in the interface heat and mass transfer of the sessile droplet during evaporation. Besides, the other components, like the nanoparticle inside the droplet, also could have a significant influence on the evaporation mechanism of the droplet due to the inherent complexity of the solid-liquid two-phase flow, impact on the solid-liquid-vapour interface moving, and the change of heat and mass transfer characteristic of the droplet interface. However, complicated issues like these have a significant meaning for practical applications in industrial and scientific fields. Therefore, revealing this tricky fundamental physics problem of the sessile droplet can greatly help the research and design of industrial applications and technology products like cooling and medical tests.

1.3.2 Research objectives

As mentioned above, there are still a lot of fundamental physics issues that need to be handled and revealed for the evaporation process of sessile droplets on biomimetic surfaces that are loaded with nanoparticles. In this section, a series of specific objectives are listed which could be helpful for further solving these physics and engineering issues:

(i) Surface roughness is a common characteristic in industrial and scientific study; it's

essential to reveal the droplet evaporation dynamics dependent on the roughness degree and have a transparent droplet analytical theory on such rough surfaces.

(ii) At present, more knowledge is needed about the mechanism of the influence of biomimetic surface microstructure on the wettability change of sessile droplets, and this process can be studied from the perspective of surface roughness.

(iii) The design of biomimetic functional surfaces shows excellent application potential in regulating surface wettability and heat transfer capacity. Therefore, revealing the relationship between surface microstructure parameters and sessile droplet evaporation dynamics is important for proposing surface design rules.

(iv) The evaporation process of nanofluid sessile droplets is unique, and surface roughness significantly affects its evaporation dynamics. Therefore, it is necessary to explore the mechanism of surface roughness's influence on the coffee ring effect of the loaded nanoparticles and the characteristics of the final deposition pattern.

(v) The effect of adding nanoparticles on the heat and mass transfer processes at the liquid-vapour interface of sessile droplets compared with pure water will also be investigated.

(vi) Carbon-based nanoparticles (carbon nanotubes/graphene) are energy materials with excellent application prospects. A comparative study of the effects of carbon-based nanoparticles on the evaporation dynamics of sessile droplets is conducted. At the same

time, the effects of different carbon-based nanoparticle materials on the deposition pattern will also be studied.

Chapter 2. Literature review

It is easy to understand that the heat and mass transfer processes are bound to undergo during sessile droplet evaporation. The critical issue is that these two processes are carried out at the interface. Therefore, an understanding of the interface between the droplet and its surrounding environment is necessary. Then, the inside flow, interfacial heat, and mass transfer mechanism will be discussed in this section to explain the evaporation process.

2.1 Physical description of droplet interface

2.1.1 Liquid-vapour interface

The liquid-vapour interface is stable when the droplet is in equilibrium, while the liquid-vapour interface will deform during the droplet evaporation. Therefore, the change in the liquid-vapour interface would break the force balance. Then, a tension force will be generated in the direction that parallels the dynamically changing surface to achieve a new equilibrium called surface tension γ (unit: $\mathrm{N/m}$), also can bed surface energy). The concept of surface tension is essential in the research of interface. Maxwell believes that the concept of surface tension was first proposed by Johann Andreas von Segner, a mathematician in Hungarian [32]. Surface tension can also be explained from a micro-scale perspective [33]. There are attractive forces (red line) and repulsive forces (yellow line) between water molecules inside the liquid, and the forces will balance each other to keep equilibrium. However, due to the lack of surrounding liquid molecules, a balance between the upward repulsive force and the downward attractive force is needed for the water molecules at the liquid-vapour interface. Then, it should be noted that the repulsive force is short-range and isotropic [34], and the

attractive force are long-range and anisotropic [33], making the forces parallel to the interface is not balanced, then the surface tension is causing. By the way, it worth noticing that determining the liquid-vapour interface area and even the droplet volume is vital for the analysis of the evaporation process. For the calculation of the liquid-vapour interface area (A) and the droplet volume (W), most studies choose the formula proposed by Shanahan et al. [35] in 1995:

$$A = \frac{2\pi R^2}{(1+\cos\theta)}, W = \frac{\pi R^3}{3}\frac{(1-\cos\theta)^2(2+\cos\theta)}{\sin^3\theta} \quad (2.1)$$

For the sessile droplet, the liquid is diffusive to the environment from the liquid-vapour interface, and this process is determined by the interfacial heat and mass transfer process on the surface essentially. Therefore, recognising the physical mechanism of heat transfer and mass transfer of the liquid-vapour interface would greatly help the study of sessile droplet evaporation.

2.1.2 Liquid-solid interface

Wetting, the ability of the liquid to remain in contact with the solid surface, which is caused by the intermolecular interaction on the liquid-solid interface [36], also means that liquid molecules are attracted to the surface by van der Waals forces after the liquid contact with the solid surface [37]. Therefore, from the microscopic viewpoint, the size of the intermolecular force will inevitably affect the wetting characteristics of the droplet when the solid wall attracts the liquid droplet through the intermolecular force. The difference in intermolecular interaction leads to excess energy at the interface, that is, surface energy (unit: J/m^2) [38]. Simultaneously, according to the definition of Gibbs free energy in thermodynamics [39], surface energy can also be defined as the increase in Gibbs free energy with the increase of unit surface area under constant

temperature, pressure and composition. By the way, it is worth noticing that the concepts of surface energy and surface free energy are easy to confuse, and surface free energy can be defined as the increase in Helmholtz free energy with the increase of unit surface area [40]. Surface energy is an intensive thermodynamic property, which means it is only related to the atomic arrangement, composition, temperature, and pressure itself but has nothing to do with system quality [41].

The distinction between surface energy and surface tension is unnecessary for liquids, but it is essential to distinguish them for the solid surface. The solid surface could divide into low surface energy surfaces with low specific surface free energies and high surface energy surfaces with high specific surface free energies for the liquid-solid interface [53]. From the viewpoint of qualitative, a high-energy surface usually has chemical binding energy on the order of about 1 eV, and a low-energy surface generally has chemical binding energy on the order of kT, where k is Boltzmann constant, and T is temperature [42]. Therefore, solid-to-liquid adhesion and liquid-inside cohesion compete, resulting in different wetting states when the sessile droplets evaporate on the solid surfaces with different surface energies. In other words, cohesion will cause water to attract each other, and adhesion will cause water to be attracted to other substances. Therefore, the droplet will be easier to wet on the high-energy surface because the droplet's adhesion work is more excellent than the cohesion work compared with the low-energy surface [43, 44].

In 1805, based on the ideal smooth surface, the British scientist Thomas Young proposed Young’s equation, which could be expressed as [14]:

$$\gamma \cos \theta_Y = \gamma_{SV} - \gamma_{SL} \tag{2.2}$$

where θ_Y is Young's contact angle, γ_{SV}, γ_{SL}, and γ is the surface tension of solid-vapour, liquid-solid and liquid-vapour interface, respectively. Young believes that the surface tension of liquid-vapour, liquid-solid and solid-vapour would meet the mechanical equilibrium in the horizontal direction after a sessile droplet located on the ideal solid surface and reaches a steady-state, which could be seen in Fig. 2.1.

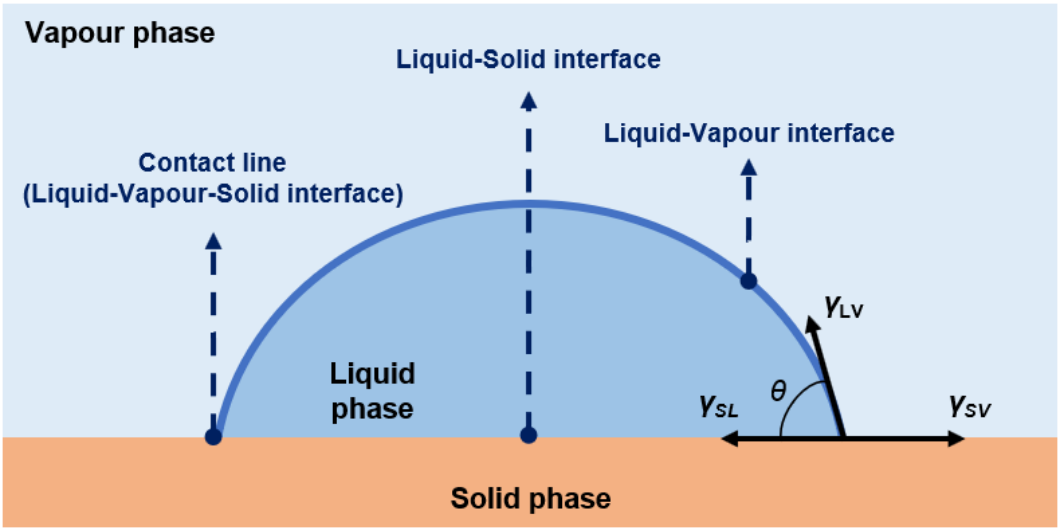


Fig. 2. 1 The balance of droplet surface tension based on Young's equation.

Thomas Young has also studied the wetting phenomenon of the droplets on surfaces. He believed that two kinds of phenomenon, complete wetting (liquid spreads on the solid surface) and partial wetting (the liquid appears to be hemispherical on the solid surface), would appear for the sessile droplet [14]. The wetting phenomenon could be described by the spread coefficient S [45]:

$$S = \gamma_{SV} - (\gamma_{LS} + \gamma) = \gamma(\cos \theta_{eq} - 1) \tag{2.3}$$

where θ_{eq} is the equilibrium contact angle. As shown in Fig. 2.2 (a), S > 0 means the surface is totally wetted. Then, as shown in Fig. 2.2 (b-c), the solid surface is partially wetted if S < 0 (0°< θ <180°), and when 0°< θ <90° and 90°< θ <180° indicates that the

solid surface is hydrophilic and hydrophobic, respectively. When $S < -2\gamma_{LV}$ means the surface is non-wetting entirely, as shown in Fig. 2.2 (d), this phenomenon does not exist in the actual situation.

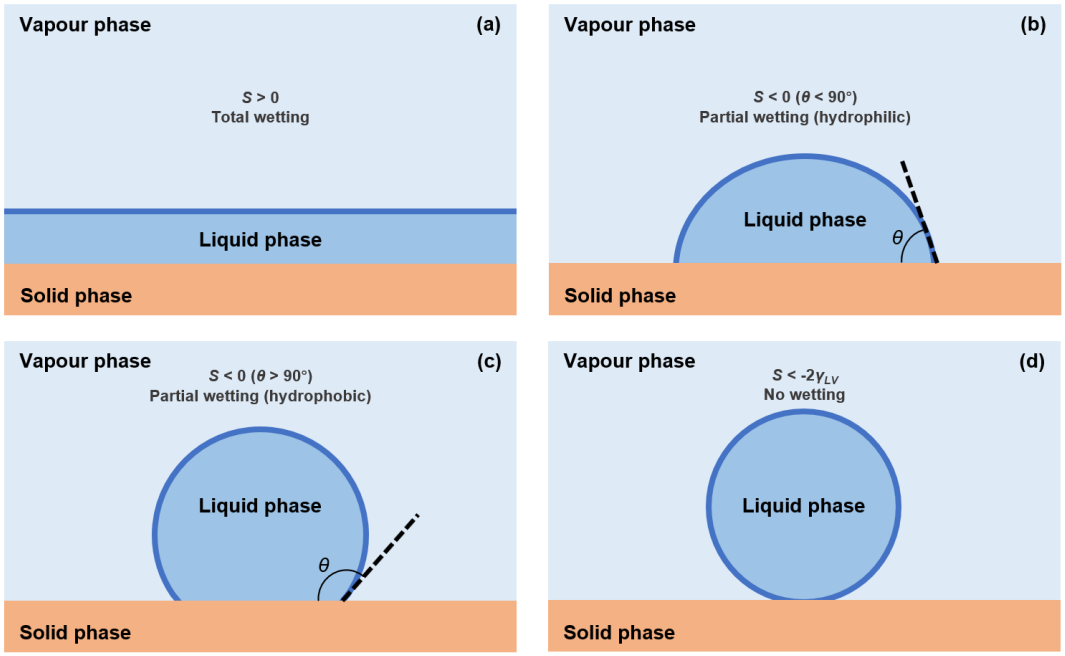


Fig. 2. 2 The different wetting conditions of sessile droplets.

As mentioned above, Young's equation is built based on the droplet on an ideal surface, which is hard to achieve in practice. Therefore, as shown in Fig. 2.3 (a), for the sessile droplet on the rough surface, Wenzel put forward the conception of the roughness factor in 1936 [46]. Then, combined with Young's equation proposed Wenzel's model, which can be expressed as:

$$\cos\theta_W = r\cos\theta_Y \tag{2.4}$$

where θ_w is (Wenzel) apparent contact angle when droplet corresponds to Wenzel's model, r is the roughness factor, identified as the ratio of actual surface area to the geometric surface area. However, the Wenzel model cannot describe the droplet wetting state appropriately for the chemically heterogeneous surface. Therefore, as shown in

Fig. 2.3 (b), Cassie and Baxter based on the chemically heterogeneous surface, which is flat and contains two chemical components, the Cassie-Baxter model has been proposed and could be expressed as [47, 48]:

$$\cos\theta_{12}^{*} = f_1 \cos\theta_1 + f_2 \cos\theta_2 \tag{2.5}$$

where θ_1 and θ_2 are the contact angle on the corresponding materials, f_1 and f_2 are the proportion of the corresponding material components ($f_1 + f_2 = 1$). So, the droplet could appear as Cassie-Baxter state if component 1 and 2 are regarded as solid and air, respectively, and the Cassie-Baxter model could be modified as [49, 50]:

$$\cos\theta_{CB} = f_1 \cos\theta_1 + f_1 - 1 \tag{2.6}$$

where θ_{CB} is the (Cassie-Baxter) apparent contact angle.

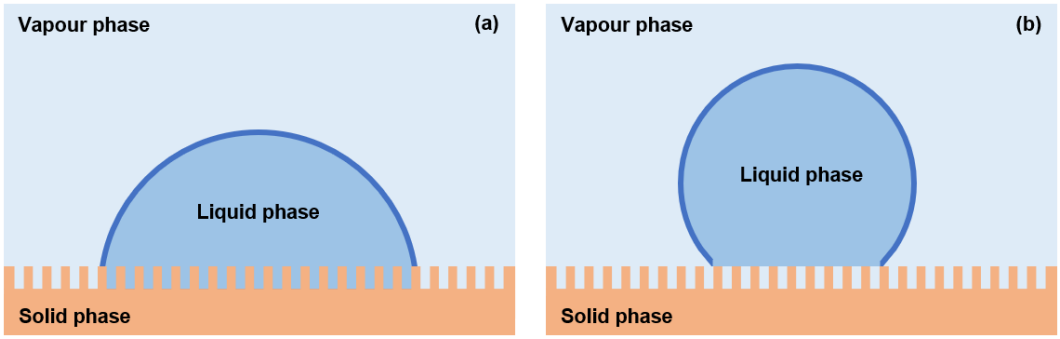


Fig. 2. 3 Schematic of two kinds of sessile droplet wetting phenomenon based on the non-ideal solid surface: (a) Wenzel's model; (b) Cassie–Baxter model.

2.1.3 Contact line region

The contact line, also known as the triple line (TL), refers to the area where the liquid droplet contacts the solid-liquid-vapour three-phase of the substrate surface. The research on the contact line region is a multi-scale problem, as shown in Fig. 2.4 drawn about the research papers. The classical fluid mechanics method cannot effectively describe the flow near the moving contact line because the moving contact line does

not conform to the no-slip boundary condition, which makes the stress calculation appear unconstrained [51, 52]. To solve this problem, methods such as artificially truncating the solution on the molecular scale can be adopted [53] or using relaxation methods for the non-slip boundary near the contact line [54]. In addition to the macro scale, the conception of microscopic molecular motion is also used to explain the triple line's physical mechanism, called molecular kinetic theory (MKT) [51, 55, 56]. It indicates that the motion of liquid molecules and their constituent atoms makes the triple line movement. Many studies have proved the validity of MKT [57, 58]. As shown in Fig. 2.4, the thin film is usually mentioned in the contact line research, also known as precursor film [59]. It is a microscopic film in front of the contact line [60]. The concept of precursor film was generally considered to be proposed by Hardy in 1919 [43, 61], who divided precursor film into primary film and secondary film, whose thickness is on the order of 1 μm and 50-500 μm, respectively [62]. Readers interested in precursor film research can refer to the review paper by Popescu et al. [59].

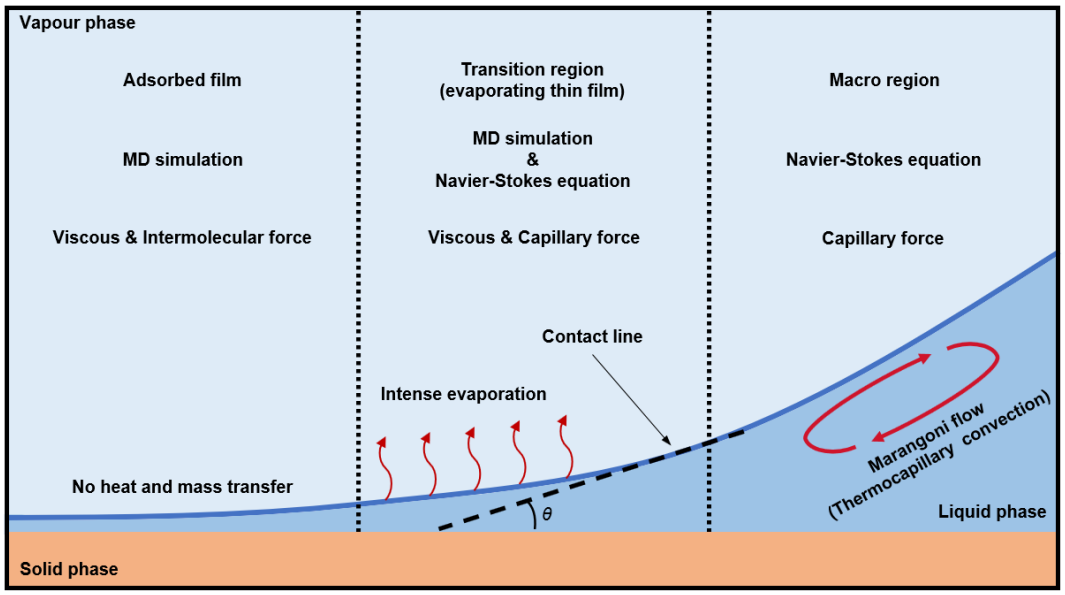


Fig. 2. 4 Schematic diagram of the study area and scaling of the contact line region.

Similarly, the change of contact angle and contact line near the triple line region also influences the droplet evaporation. In 1977, British scientists Picknett and Bexon proposed that the droplet evaporation process on the ideally homogeneous surface could be divided into two evaporation modes: the constant contact area mode and the constant contact angle (CCA) evaporation mode [63]. The constant contact area mode also can be called constant contact radius (CCR) evaporation mode [64], as shown in Fig. 2.5 (a) and (b). Besides, Shanahan et al. [35, 65] found that the evaporation process of sessile droplet would go through the stick-slip process of the triple line due to the phenomenon of contact angle hysteresis, which also is called stick-slip (SS) evaporation mode, as shown in Fig. 2.5 (c). For the SS mode, the contact line movement is a fascinating phenomenon. Shanahan and Sefiane [66] proposed a basic theory to depict the relationship between Gibbs free energy principle and the "stick-slip" phenomena of the droplet. It always could be called the "Shanahan–Sefiane model" [67]. Gibbs free energy can be expressed as:

$$G = \gamma A + \pi R^2(\gamma_{SL} + \gamma_{SV}) = \gamma\pi R^2\left[\frac{2}{(1+\cos\theta)} - \cos\theta\right] \tag{2.7}$$

Gibbs excess free energy can be expressed as:

$$\delta\widetilde{G} = \frac{\delta G}{2\pi R} = \frac{\gamma R(\delta\theta)^2}{2(2+\cos\theta_0)} \tag{2.8}$$

The energy barrier U can be evaluated as:

$$G_c = \gamma\pi R_c^2\left[\frac{2}{(1+\cos\theta)} - \cos\theta_0\right] < 2\pi R_c U \tag{2.9}$$

$$U \sim \gamma R_c\left[\frac{1}{(1+\cos\theta_0)} - \frac{\cos\theta_0}{2}\right] \tag{2.10}$$

The Shanahan–Sefiane model indicated that if the contact radius r reaches the critical radius R_c after a series of sticking and slipping processes, the droplet would not have sufficient excess free energy to surmount the energy barrier U. After that, the triple line would still anchor at the R_c, the contact angle of the sessile droplet would steadily

reduce to zero, and the evaporation process ends [35].

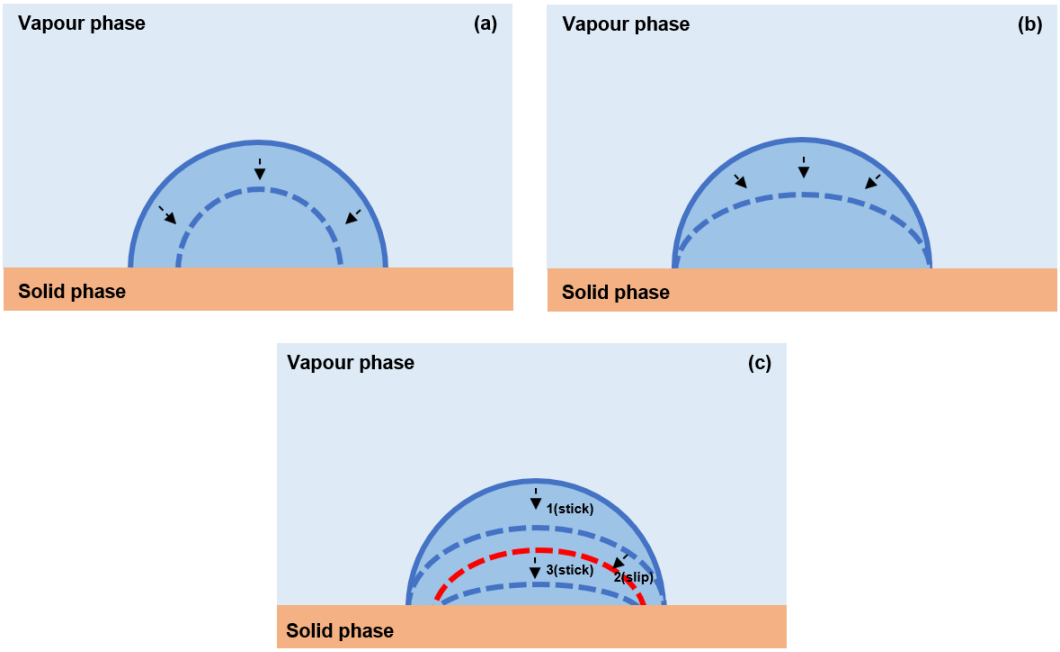


Fig. 2. 5 Schematic diagram of droplet evaporation modes: (a) CCA mode; (b) CCR mode; (c) SS mode.

2.2 Basic physical process of droplet evaporation

2.2.1 Marangoni flow and buoyancy convection

Marangoni flow is a classic fluid mechanism issue and has an essential effect on the field of welding [68], crystals growth [69], and electron beam melting [70]. The Marangoni flow is named based on the researcher, the Italian physicist Carlo Marangoni, who studied this phenomenon during his PhD degree [71]. By the way, it is worth noticing this phenomenon has been discovered and described earlier as the form of "tears of wine" by the British physicist James Thomson, who is a fellow of the Royal Society and the older brother of William Thomson (Lord Kelvin) [72].

The Marangoni flow in the droplet is that a surface tension gradient appears along the droplet surface (e.g., liquid-vapour interface), usually caused by the non-uniform temperature or substance concentration distribution. Therefore, these surface changes will cause a gradient of surface energy, which generates shear stress and then pushes the fluid to circulate flow along with the interface. The Marangoni flow can be divided into thermal Marangoni flow and solutal Marangoni flow depending on whether it is caused by temperature or concentration change [73, 74]. As mentioned above, the difference in surface temperature leads to the thermal Marangoni flow. By the way, for the surface tension gradient caused by non-uniform surface temperature, the thermal Marangoni flow can also be called thermocapillary convection [75].

Buoyancy is a universal physical force in nature, and it was first proposed and studied by Archimedes around 200 BC [76]. The appearance of buoyancy requires two key factors: 1) the gravity field and 2) the density variation. In other words, for the buoyancy flow, both the uneven distribution of temperature and concentration will cause density changes in the corresponding space. Therefore, the flow instability caused by buoyancy and the convection resulting can be called buoyant convection, which is widespread in our lives and industrial applications [77, 78].

2.2.2 Evaporative cooling effect

During the droplet evaporation, the droplet liquid-vapour interface will have the heat transfer process, and the evaporative cooling effect would also exist. The evaporative cooling effect, so-called the interface cooling effect, is a crucial influence process that

needs to consider during the evaporation of droplets. The evaporative cooling effect at the droplet interface could establish a temperature gradient that induces buoyancy-driven convection inside the droplet [79]. Two factors can cause the evaporative cooling effect from the material properties: 1） the substrate thermal conductivity; 2) the droplet thermal resistance [80]. From the physical mechanism, the evaporative cooling effect is associated with the latent heat of vaporization, also known as enthalpy of vaporization ΔH_{vap}, it can be written as: $\Delta H_{vap} = \Delta U_{vap} + p\Delta V$. When the droplet is evaporating in the environment, the liquid-vapour interface needs to continuously absorb heat from the environment. During this process, the latent heat of vaporization is increasing with the evaporation rate. Therefore, the interface temperature is further reduced.

2.2.3 Diffusion and Stefan flow

During the droplet evaporation, to analyse from a microscopic perspective, the mass transfer of the sessile droplet interface is the process of how liquid molecules across the liquid-vapour interface become vapour molecules and diffuse from the liquid-vapour interface (the surface of the droplet) to the air space. Therefore, if the sessile droplet is not be affected by the surrounding environment in the open space, such as forced convection or multiphysics, its evaporation could be regarded as the vapour diffusive from the interface to the environment, which could be predicted by Fick's law [81, 82]:

$$J = -D \cdot \nabla \tag{2.11}$$

Furthermore, based on Eq. (11), when assuming two binary mixtures of A and B that do not react chemically, the general expression of Fick's law also can be written as [83]:

$$\dot{m}''_A = Y_A(\dot{m}''_A + \dot{m}''_B) - \rho D_{AB}\nabla Y_A \quad (2.12)$$

where ρ is density, $\dot{m}''_A$ and $\dot{m}''_B$ are the mass fluxes of matter A and B, respectively. Y_A and Y_B are the mass fractions of matter A and B, respectively. D_{AB} means the binary diffusivity, which is measured in m^2/s. Therefore, focusing on droplet evaporation, it is easy to find that the evaporation rate depends on the concentration gradient between the droplet liquid-vapour interface and the ambience far away if the external convection is ignored.

Stefan flow is also one of the mass transfer mechanisms that should be considered in droplet evaporation [84]. For a mixed gas (e.g., vapour and air mixed), assuming that the total mss flow is $,v_0$, then each of these gas flows can be divided into 1) the diffusion flow due to concentration gradient; 2) the flow of the substance component caused by the overall flow of the mixed gas. Consider liquid A and the mixture of vapour species A and air species B flow across the top of the liquid-vapour interface. Based on Fick's law, it can be expressed as [83]:

$$\dot{m}''_A = Y_A\dot{m}''_A - \rho D_{AB}\frac{dY_A}{dx} \quad (2.13)$$

Therefore, taking the problem of droplet evaporation as an example, the Stefan flow not only means the diffusion flow of the vapour but also includes the mass flow of vapour, which is carried by the overall flow of the mixed gas. Besides, Hu et al. compared the results of FEM analysis of the droplet evaporation process with the analytical solution. They derived a simple approximate expression for the evaporation rate, which can be described as:

$$\dot{m}(t) = -\pi RD(1-H)c_v(0.27\theta^2 + 1.30) \quad (2.14)$$

Where H is the relative humidity of the ambient air, c_v is the saturated water vapour

concentration, R is the contact-line radius, and D is the water vapour diffusivity.

2.3 Effect of contact surface on evaporation characteristics of sessile droplets

The droplet evaporation dynamics are strongly related to the solid surface characteristics, such as hydrophobicity, configuration, roughness, thermophysics, and even chemicals. Many influencing factors can produce these characteristics changes in the substrate surface, such as the nanocomposites [85], physical processing [86], and chemical synthesis [87].

2.3.1 Hydrophobicity of substrate surface

In the process of droplet evaporation, the wettability of the substrate surface will not only affect the characteristics like contact angle and contact radius of the droplet, the detailed research about this could refer to the review by Cheng et al. [88], but also can make an effect on the evaporate rate [89, 90]. Many studies on droplet evaporation dynamics have been carried out from the hydrophobic to hydrophilic surfaces, including mixed hydrophilic and hydrophobic surfaces. In this chapter, the surface materials commonly used in the related research have listed in Table 2.1. It must remind that some evaporation time and evaporation mode listed in Table 2.1 are not the total lifetime of droplet because the precise lifetime data have not provided in the relevant literature. Still, the evaporation time listed in Table 2.1 indicates the final stage of droplet evaporation, which can also be used as an approximate guide.

Firstly, the researchers compared the evaporation process of droplets on hydrophilic and hydrophobic surfaces [91, 92]. Gibbons et al. [93] compared the process of droplet evaporation on the hydrophilic and superhydrophobic surface. They found that the total evaporation time on the hydrophilic surface is shorter, and the most significant heat flux existed in the contact line region. Similarly, Dash et al. [94] investigated the evaporation characteristics of sessile water droplets on hydrophobic and superhydrophobic surfaces experimentally. The results showed that compared with the hydrophobic surface, on the superhydrophobic surface, the total evaporation time is longer in the range of substrate temperature of 293-333 K. Besides, many studies have shown that the evaporation rate decreases as the hydrophobicity increases [95, 96]. Pan et al. [97, 98] considered two transmission mechanisms, buoyancy convection and evaporative cooling effect, within the range of contact angle of 10°-160° through numerical simulation and the results as shown in Fig. 2.6. The results indicated that the droplet on hydrophilic surfaces (smaller contact angles) would be influenced by buoyancy convection greater rather than the evaporative cooling effect, and the evaporation process would be promoted as shown in Fig. 2.6 (a) and (b). Then, as shown in Fig. 2.6 (c) and (d), the effect of evaporative cooling becomes more evident with the increase of surface hydrophobicity (contact angle increased), thus inhibiting the evaporation process. Similarly, Sobac et al. [99] has carried out droplet evaporation experiments with a range of contact angle of 17°-135°, revealed that the influence of contact angle on evaporation should begin to consider when the contact angle more than 40°. By the way, it's interesting to notice that He et al. [100] designed to place and squeeze droplets between two parallel hydrophobic/superhydrophobic surfaces. They found that the droplet will have residue on the upper surface during evaporation, but it's will not happen on superhydrophobic

surface. And the evaporation time of droplet on parallel superhydrophobic surface will short than it on parallel hydrophobic surface.

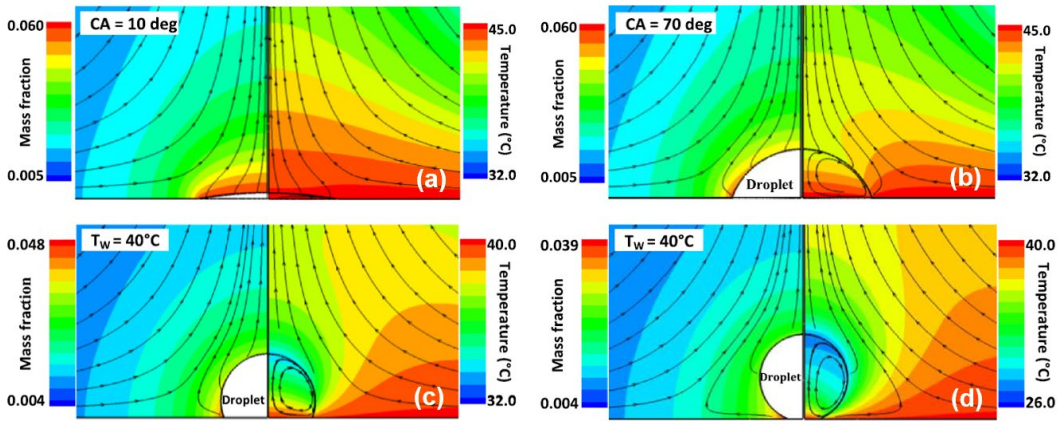


Fig. 2. 6 Contour picture of the temperature distribution and vapour mass fraction with a streamline of the evaporating droplet when the contact angle (CA) and the substrate temperature (Tw) is (a) CA = 10°, Tw = 45.6°C; (b) CA = 70°, Tw = 45.6°C; (c) CA = 110°, Tw = 40°C [97].

Besides, the surface wettability also could influence the evaporation mode during droplet evaporation. Kulinich et al. [101] indicated that the hydrophobic surface associated with high contact angle hysteresis (CAH) and the hydrophilic surface associated with low CAH corresponds to the CCR and CCA mode of droplet evaporation, respectively. It could be explained from an intuitive perspective that a surface with high CAH corresponds to a "sticky state", and a surface with low CAH corresponds to a "slippery state". Kashaninejad et al. [102] based on four different values of the eccentricity of microhole arrays to design polydimethylsiloxane (PDMS) surface, and found that compared with smooth PDMS surface, the droplet evaporates on the microhole-patterned surfaces will not go through the process of CCA mode, and the trend of mode change was partially correlated with the trend of CAH on the microhole-patterned surfaces. Yu et al. [103] also found that for pure water droplet, the duration of the CCR mode would be shorter when pillar-to-pillar or hole-to-hole

spacing of PDMS surfaces is increasing.

Table 2. 1 The summary of the water droplet evaporation process is based on different wettability.

CA	Surface material	Volume	Lifetime	Mode	Ref.
~160°	Silicon wafer & Teflon	3 μL	~2200 s	CCA	[80]
~150°	Glaco mirror coat zero (912 W/m^2)	80 μL	~1920 min	CCA	[104]
~150°	Carbon nanofiber (CNF)	1.6 μL	~1000 s	CCR/Mixed	[105]
~138°	PDMS surface	1.90-3.05 μL	~1900 s	CCR/Mixed	[103]
~130°	Multiwalled carbon nanotubes	2 μL	~1800 s	CCR/Mixed	[106]
~120°	Silicon wafer & Teflon (40 ℃)	3 μL	~677 s	CCA/Mixed	[94]
~110°	Indium Tin Oxide (1153 W/m^2)	3 μL	~426	CCR/Mixed	[107]
~108°	Cytop	3 μL	~2500 s	CCR/Mixed	[108]
~91°	PFDTS & SiO_2	1 μL	~940 s	CCR/CCA	[109]
~83°	Polysulfone	10 μL	-	CCR/SS	[67]
~82°	Polypropylene	10 μL	-	CCR/SS	[67]
~63°	Stainless steel A304	10 μL	~2250 s	CCR/Mixed	[67]
~62°	Aluminum Al2024	10 μL	~2250 s	CCR/Mixed	[67]
~55°	Oct-silicon wafer	3 μL	~1800 s	CCR/CCA	[110]
~49°	Aluminium (40 ℃)	4 μL	~380 s	-	[111]
~28°	Glass	3 μL	~870 s	CCR/Mixed	[108]
<10°	Silica-coated copper (101 ℃)	9 μL	~38 s	-	[112]

In addition to the research on hydrophilic/hydrophobic surfaces, the wicking phenomenon also attracts many researchers to study. Wicking is defined by Washburn in 1920s as a phenomenon when the droplet is absorbed and spread passively on the superhydrophilic and porous surface, and a thin film appeared [113]. Auliano et al. [114] shown that by changing the height of Si nanowires on the surface to adjust wicking capability, up to 82% reduction in evaporation time can be achieved. As shown in Fig. 2.7, Chen et al. [115] based on the ZnO nanowires surface, compared with regular nanowires, the irregular nanowires could make the droplet spread wicked more quickly, which due to the irregular distribution could promote the process of wicking and spreading. Poudel et al. [116] based on the porous nanochannels surface, found that the evaporation flux of thin film on the nanochannel-pores is about two orders of magnitude higher than that of the liquid-vapour interface of the droplet, which can make the surface obtained about 77 W/cm^2 of the heat dissipation capacity. Therefore, the hydrophilic surface wicking phenomenon can enhance the evaporation capacity of droplets, which would have considerable application potential in the field of thermal management [117].

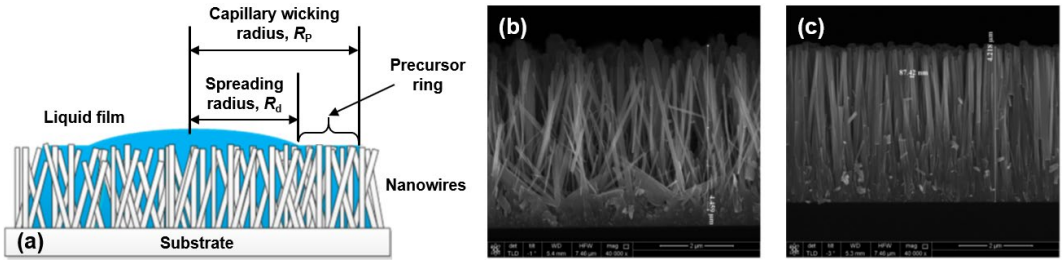


Fig. 2. 7 (a) Schematic diagram of droplet spreading and wicking on the surface of the nanowire; (b) electron microscope image of irregular nanowires; (c) electron microscope image of regular nanowires [115] .

Besides, the heterogeneous surface (biphilic surface) also be studied to explore the

effect on condensation [118] and evaporation[119, 120]. Cui et al. [106] fabricate the hydrophilic surface with multiwalled carbon nanotubes, and part of the surface is changed to hydrophobic by electrowetting. They found that the droplet on the heterogeneous surface can keep the contact area constant (contact line pinned) and improve the evaporation rate due to the increased meniscus radius of the liquid-vapour interface. Aboubakri et al. [121] also design three kinds of mixed wetting surface, which on the hydrophobic silicon substrate, the hydrophilic small size spots with circle, square, and rhombic shape are fixed up, respectively. The results shown that the square-shaped spots cannot make heat transfer of surface be enhanced, and the circle spots which size is one-sixteenth times of the radius of the droplet has the most obvious effect of improving heat transfer.

2.3.2 surface roughness and topography

As described above, using the physical or chemical method could change the original natural topography of the surface, thereby further changing the surface wettability, and the droplet evaporation dynamics could also be affected. Therefore, the substrate surface configuration has a significant effect on the droplet evaporation process [122]. This chapter would discuss the common see influence factors of the substrate in the research of sessile droplet evaporation, such as surface geometry, roughness, and the chemical pattern.

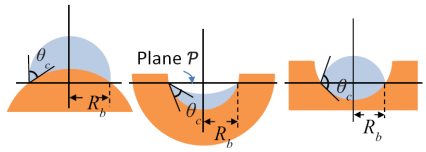
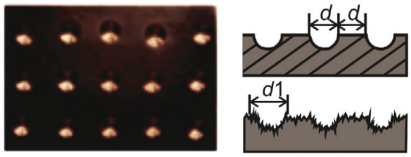
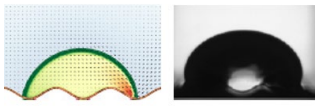
Many scholars have researched the influence of surface topography on the sessile droplet evaporation process. Misyura et al. [123] design a wave-shaped wall structure

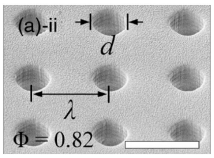
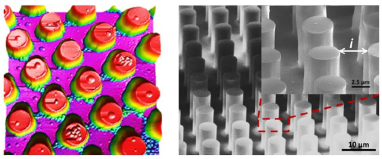
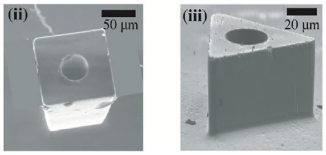
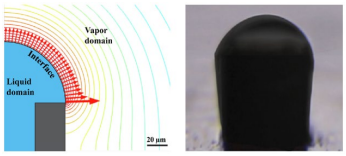
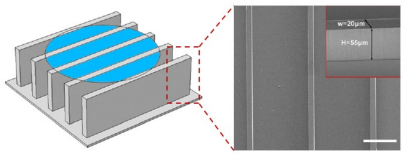
and found that as the decrease of distance between wave peaks, then the area of the droplet bottom surface and the evaporation rate increase simultaneously. Shen et al. [124] found that for a droplet evaporating on the curved substrate, the evaporation time would be longer with the increase of tangential angles of the curved surface, which may be owing to the thermal resistance from the bottom surface of the substrate to the liquid-vapour interface be enlarged. Besides, the surface configuration always can influence the shape of the droplet. Shan et al. [125] based on circular, square, and triangular cross-sections of micropillar substrate, let the contact line exhibited as asymmetric geometry during evaporation. The results showed that the asymmetric droplets could enhance the transport of evaporation significantly. Especially for triangular micropillars, compared with square and circular, due to the larger perimeter-to-area ratio and surface curvature, the evaporation flux can increase by 8% and 45% when the substrate temperature is 60°C, respectively, this phenomenon also proved by Sáenz et al. [126] earlier. It needs to say that the changes in surface configuration are various, so it isn't easy to describe all forms of the structure surface configuration. Therefore, in Table 2.2 just the substrate surface configurations which are commonly used in the research of sessile droplet evaporation are listed.

Also, the substrate surface geometry could affect the movement of the contact line and change of contact angle [127, 128]. Kuznetsov et al. [127] found that if the cavities and protrusions of the surface are smaller, then the movement speed of the contact line would be higher. They also found that even if some surface with greater roughness, the contact line movement could also be faster. The reason is that compared with the ordered texture surface, the cavities would fill by gas in the roughness surface, which

caused a homogeneous wetting phenomenon and made lower hydrodynamic resistance. Wang et al. [128] found that the sharp edge of the PDMS substrate could significantly influence the wetting and dewetting process of the droplet. For the proper edge angle of the substrate, the contact angle of liquid with high surface tension could reach 180°. They also revealed that both the maximum contact angle and pinned degree of contact line would increase with the substrate edge be sharper. In addition, for the change in contact line and contact angle, Kumar et al. [129] found that the change of micropillars on the surface could make the wetting state switch between Cassie–Baxter and Wenzel state, and the phenomenon of droplet wetting state could change in the micropillar surface also found by other researchers [130]. Jiang et al. [131] fabricated pillared and pored surfaces by soft lithography technique with PDMS. They found that the contact line would not be distorted on the pored surface but be distorted on the pillared surface significantly, and the degree of distortion changed with the density of pillars.

Table 2. 2 The summary of substrate surface topographies commonly used.

Schematic diagram	Configuration	Ref.
	Convex/concave substrate	[132]
	Dimples substrate	[95]
	Wavy surface	[133]

	Pored surface	[131]
	Micropillar (cylinder column)	[134]
	Micropillar (square/triangular column)	[125]
	Micropillar with pipeline	[82]
	Line-shaped microstructure	[135]

The research of surface roughness is of great significance and meaning. It can affect wear behaviour or structural integrity and could use to reflect the tool's working condition. At present, many studies have shown that surface roughness can affect not only the flow and heat transfer characteristics of fluids but also the wettability [136, 137]. Therefore, the effect of roughness on droplet evaporation is naturally considered and studied [92, 112]. Wang et al. [86] based on the Wenzel model as expressed in Eq. (4) analyses that the CA would be greater with the increase of surface roughness when droplet CA less than 90°, and the CA would be smaller with the increase of surface roughness when droplet CA more than 90°. Therefore, in their experimental study, the droplet evaporation rate is faster on the 1200 pp surface than on the 400 pp surface ("pp" represents abrasive paper grits in their research). For the substrate surface roughness, the macroscale and the research based on the microscale can also help people

understand the wetting mechanism of droplets better, especially near the triple line of the droplet. As shown in Fig. 2.8, Liu et al. [138] revealed that even if the roughness of atomic level existed on the solid surface, it could still cause static hysteresis and the distortion of the contact line. Zhang et al. [139] based on the polytetrafluoroethylene (PTFE) colloid droplet, also found that the roughness could promote the droplet evaporation rate. They also indicated that the coffee-ring effect would be promoted on the rough surface compared with the smooth surface. This phenomenon is due to the surface roughness inhibiting the internal recycling flow and strengthening the pinning of the contact line, making the nanoparticles remain in the edge of droplet more easily. Hu et al. [140] based on the V-grooved surfaces which contain the parameters of depth and pitch to study the influence of surface roughness on the thin film evaporation of droplet and found that the rate of heat transfer would monotonic increasing with groove depth, but for the groove pitch a critical value existed and surface roughness could restrain the thin film evaporation if the pitch is less than the critical value. Besides, the roughness also could make effect on the thermal management, such as the Leidenfrost temperature also could increase with the roughness and thereby influence the spray cooling performance [141].

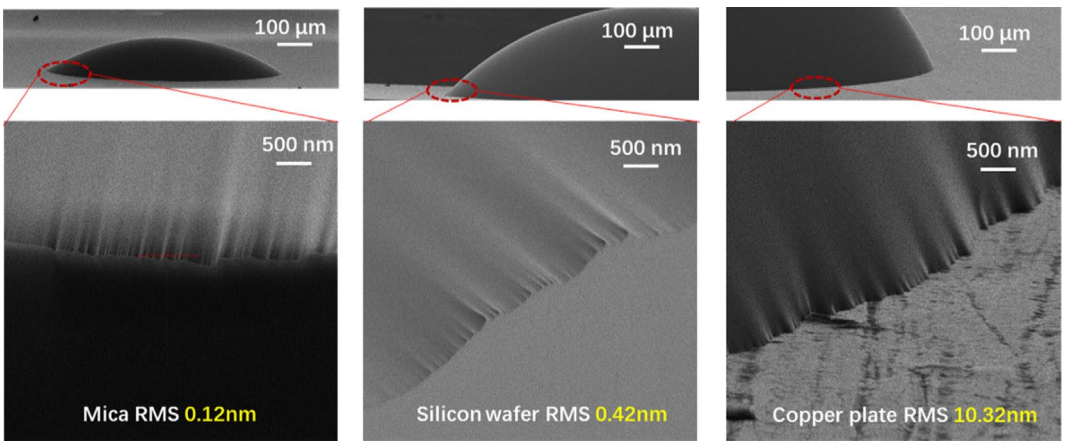


Fig. 2. 8 Three-dimensional shape around the static contact line at the nanometer scale photo by helium ion microscopy [138] .

2.3.3 Internal thermal conductivity and external heating of the substrate

For the heat transfer process, the substrate material thermal conductivity could influence the droplet internal and interfacial heat transfer process during the droplet evaporation. Thereby the mass transfer of droplet also is affected. For the thermal condition, many kinds of research have shown that it strongly influences droplet evaporation. Shen et al. [142] found that the droplet evaporation rate is higher for the substrates with higher thermal conductivity through numerical simulation. David et al. [143] got the same results through experiments and found this phenomenon more apparent for larger droplet volume. Besides, lots of research reveals that the substrate thermal conductivity is directly proportional to the evaporation rate [144, 145]. Based on the experimental research, Gleason et al. [146] found that not only cannot ignore the effect of evaporative cooling on the surface with low thermal conductivity, they also quantitatively shown that the surface temperature will be reduced effectively within 1000 μm from the triple line. Sáenz et al. [147] reveal that the average surface temperature would essentially constant during CCA mode, and would increase during CCR mode which can make droplet be thinner, so the evaporation rate would increase more rapidly for CCR mode when the substrate heating is also increased. Saada et al. [148] concluded that regardless of whether it is pinning or depinning droplet, the decrease of the thermal substrate conductivity or the increase of substrate thickness will have a cooling effect that could expand the cold region of the droplets near the liquid-vapour interface. In other words, for the substrate with very high thermal conductivity

or very thin thickness, the evaporation rate would be fast, and the energy supply from the substrate. However, for the substrate almost adiabatic or large thickness, the evaporation rate would be slow, and the energy supply from the vapour phase. The substrate materials used in the research of substrate thermal conductivity effect are listed in Table 2.3.

Table 2. 3 Summary of materials commonly used for droplet evaporation considering the thermal conductivity

Substrate	Thermal conductivity	Size (L*W*H)	Liquid	Ref.
Glass	1.05 W/m·K	50*50*0.5 mm	Water	[149]
Silicon	139.4 W/m·K	50*50*0.5 mm	Water	[149]
Aluminium	237 W/m·K	10*10*1 mm	Methanol	[143]
Copper	401 W/m·K	10*10*10 mm	Water	[150]
Titanium	21.9 W/m·K	10*10*1 mm	Acetone	[144]
Stainless steel	15 W/m·K	150*150*1 mm	Water	[151]
Macor	1.46 W/m·K	10*10*1 mm	Water	[144]
Telfon	0.25 W/m·K	- * - *3 mm	Water	[152]
PTFE	0.25 W/m·K	10*10*1 mm	Methanol	[143]
PDMS	0.23 W/m·K	- * - *4 mm	Ethanol & polystyrene	[153]
POM	0.31 W/m·K	10*10*10 mm	Water	[150]
EPS	0.03 W/m·K	- * - *3 mm	Water	[152]

The heating from the substrate can also significantly influence the droplet evaporation [154] [155], as shown in Fig. 2.9. Kadhim et al. [111] reveal that whether it is a

hydrophilic or hydrophobic surface, the total evaporation time will decrease when the substrate temperature increases from 40℃ to 60℃. Also, many studies confirm this conclusion [156]. In addition to the constant temperature, some researchers also have carried out studies on the constant heat flux boundary condition [157]. Gao et al. [107, 158] studied the heat flux range of 1000-7000 W/m^2 and found that the droplet size could significantly affect the evaporation time under low heat flux, but this effect would be weakened with the increase of heat flux. Besides, with the increase of the heat flux, the evaporation time would be shorter naturally and found that the CCA mode does not happen during the evaporation for both hydrophobic and hydrophilic surface under the range of heat flux. Besides, the non-uniform temperature distribution of the substrate also be considered by Pradhan et al. [159], they found that the temperature difference can induce the flow inside the droplet, and the flow direction could affect by droplet volume.

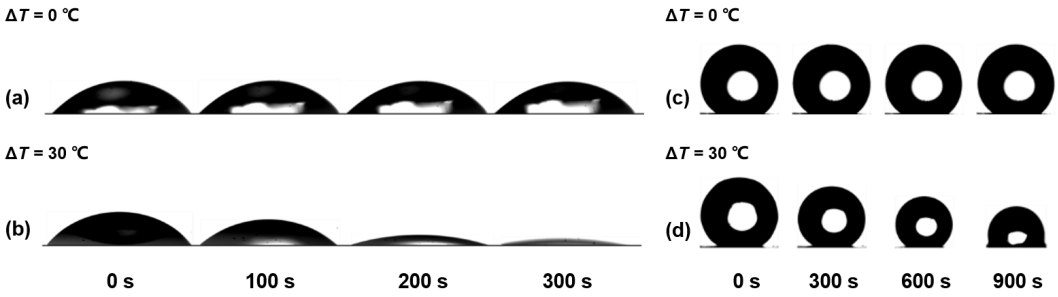


Fig. 2. 9 Droplet evaporation process on the (a) hydrophilic surface and (b) superhydrophobic surfaces with two kinds of temperature gradients (ΔT) [155] .

Besides, laser heating also attracted many researchers because the photothermal effect has the advantages of non-contact control and rapid control response, realising the precise control of the droplet evaporation or movement. Jiao et al. [160] revealed that the droplet temperature increase rate and the maximum interface temperature were

raised with the laser power linearly so that the evaporation rate could be good controlled. They also found that some satellite droplets could generate near the contact line during the local laser heating. Besides, Liu et al. [161] compares substrate heating with laser heating and found that different heating methods can influence nanofluid droplet deposition pattern.

2.3.4 Other kind of substrate properties

So far, for the substrate, the effect of hydrophobicity, configuration, thermal conductivity and external heating has been introduced above. Of course, it still has some kinds of substrates that have unique characteristics that could affect the wetting or evaporation process of the sessile droplet, such as substrate coated by lubricating fluid [162], porous media [163] and some materials which have unique properties [89, 164]. In this chapter, some current research about these unconventional substrates will be introduced, and readers could refer to the review papers [162, 165] or books [42, 64] if interested in these substrates influence.

Guan et al. [166] focus on slippery liquid-infused porous surfaces (SLIPS), a microtextured surface immersed by lubricating liquid. They found an ideal constant contact angle mode abided by the small sessile droplets (D ~ 2 mm) during evaporation. Sharma et al. [167] also put the water droplet on the lubricating fluid coated slippery (LCS) surface. As shown in Fig. 2.10, they found that the total evaporation time would be longer than the droplet put on the dry surface, which due to the formation of the wetting ridge (WR) and cloaking film could suppress the evaporation process. They also indicated that only CCA and mixed mode on the LSC surface existed, but on the

dry surface, the CCR mode would also appear, as shown in Fig. 2.10 (a) and (b). However, Chen et al. [168] based on the vary soft PDMS films substrate, found that the evaporation kinetics can be influenced by vertical and horizontal motions of the WR simultaneously. The pinning force was associated with the vertical rise of the WR and resulted in a CCR mode, and the authors also found that on the very soft substrate, the WR can be dragged by the contact line horizontally and which is the reason for the mixed mode.

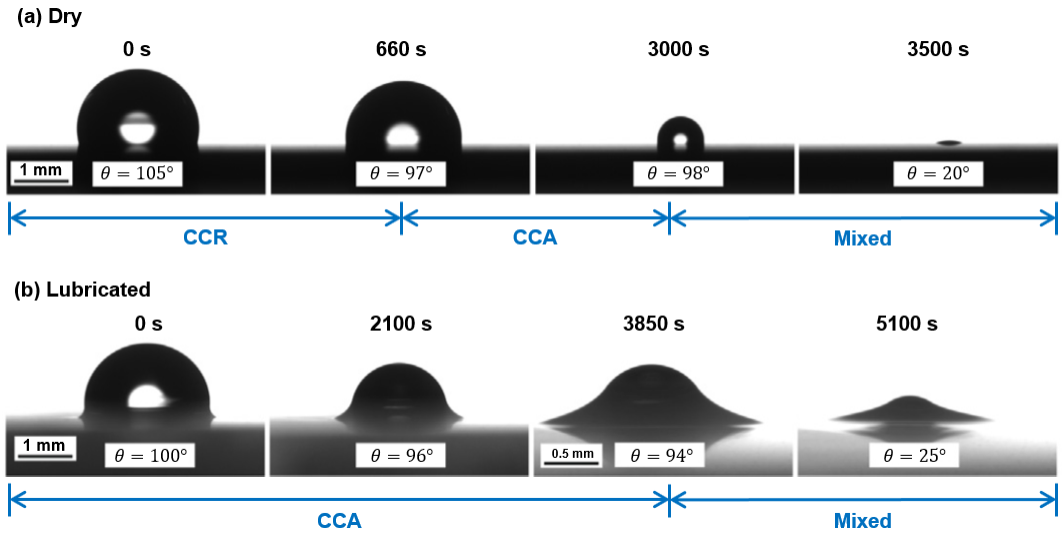


Fig. 2. 10 the evaporation process of the same volume of the water droplet on the (a) dry and (b) LCS surface [167].

The effect of porous media also attracted lots of researchers to study. Pham et al. [169] found that the liquid droplet shedding properties would maintain longer with the porous substrate thickness based on the lubricant-infused porous surface. Arrabito et al. [170] proposed a novel method that put the DNA-rich aqueous droplets on the hydrophilic nylon porous substrate to make DNA that existed inside the droplet covered homogeneously. Besides, the heat transfer rate of droplet evaporation could also be promoted on the porous substrate due to its higher wicking rate [171], and the time scale

of the spreading and wicking process after the droplet touched the porous substrate is microsecond and millisecond, respectively [171]. Zhou et al. [172] indicated that the coffee-ring effect would disappear with the increase of pore diameter and depth of the porous structure, so the wetting ability of porous substrate could be adjusted by changing the structure parameters, by the way, the process of spreading and penetration is a competitive relationship [173]. Goh et al. [174] found that the droplet on the graphene nanoplatelets (GNPs) coated surface could achieve high evaporation rates due to the wetting and spreading ability be improved and the wetted area also is enlarged. The experimental results showed that the cooling effective could promote 4866% compared to the bared surface under the substrate temperature of 75 ℃.

2.4. Effect of liquid properties on evaporation characteristics of sessile droplets

The influence of substrate configuration and physical properties on droplet evaporation have been discussed in section 3, which indicates that the solid phase would have a crucial impact on the evaporation dynamics. Naturally, it is not difficult to consider that the liquid phase would also influence the evaporation process significantly. The droplet liquid thermofluid physical properties, such as viscosity, thermal conductivity, and mass diffusivity, would vary with the liquid composition changes, and the interfacial heat and mass transfer characteristics could also be influenced during the sessile droplet evaporation. This section will mainly discuss the influence mechanism of loaded nanoparticles and added surfactants on the droplet interface heat and mass transfer and the change of evaporation mode based on the research in this thesis.

2.4.1 Evaporation process of droplets loaded with nanoparticles

Nowadays, nanofluid has been used widely after Choi et al. [175] proposed it in 1995, whose initial purpose was to improve the fluid heat transfer characteristics. Naturally, nanofluid not only applied in the field of chip cooling, vehicles thermal management, fuel cells and solar collectors etc. [176], but the influence of nanofluid properties on droplet evaporation also attracted a lot of researchers' attention [177]. The main scientific problems of nanofluid droplet evaporation are how the nanoparticles influence the evaporation dynamics and the particles deposition pattern after evaporation. Therefore, the deposition of nanoparticles can refer to the review of Zhong et al. [177] and would not be focused mainly on in this section. Therefore, the nanofluid droplet evaporation process, included the impact of nanoparticles on the interfacial heat and mass transfer and the evaporation mode, would be discussed in detail.

It is not difficult to realize that nanoparticles can impact the evaporation rate and have been studied widely in recent decades. Wei et al. [178] revealed that insoluble nanoparticles could make the evaporation process deviation from the classical d^2 law. Zhu et al. [179] found that the evaporation time would extend with nanoparticle concentration. This trend may explain by the study of Wang et al. [180] based on the molecular dynamics simulation, which reveals that the evaporation rate could be suppressed at the liquid-vapour interface where the nanoparticles exist caused the latent heat of evaporation increase. However, Sefiane et al. [181] based on the ethanol solvent and Al nanoparticles, revealed that even though the pure liquid droplet evaporation rate is faster than nanofluid during pining stage, but the overall droplet evaporation time of nanofluid is less than pure fluid. This could attribute to the pinning time of pure liquid

is less than nanofluid (pinned stage lasted about 80-90% of the total lifetime). Shin et al. [182] also found that the total evaporation time would decrease with the increase of concentration for the Al_2O_3-water nanofluid droplet on the hydrophilic glass substrate. They explained that it might be due to the perimeter increasing with the concentration and expanding the contact area, improving the heat transfer performance. Zaaroura et al. [183] found that the evaporation rate of the gold nanofluid droplet on the unheated surface is lower than water but higher when the substrate is heated. They also found the higher evaporation rate is also associated with the higher life of the convection cell. It's related to the thermal Marangoni flow and the Brownian motion, which is also revealed by Jiang et al. [184].

The above contradictory conclusions about the influence of nanoparticles on the evaporation time may be due to the nonlinear relationship between the concentration of nanoparticles and the evaporation rate. Chen et al. [185] found that the Ag-water nanofluid droplet evaporation rate would not be influenced by low concentration. Still, it could decrease when the concentration continued to increase during the evaporation, which means that a transition or critical point existed in the nanofluid droplet evaporating process. This phenomenon is also shown in the research of Chen et al. [186], who based on graphene-PEG-water nanofluid, found that the droplet evaporation rate would reach the maximum at the concentration of 0.25 mg/ml and would decrease with the increase of concentration. Recently, Xu et al. [187] proposed the phenomenon of critical concentration in their research of solar-driven nanofluid droplet evaporation. They indicated that the evaporation rate would increase with the increase of nanofluid concentration until ~10 ppm. When the concentration is beyond 10 ppm, the

evaporation rate will become constant due to the effective nanoparticle layer that can absorb solar energy no longer change. Besides, there also have a lot of nanofluid droplet evaporation research based on all kinds of nanoparticles. Some of the common to see in the studies have listed in Table 2.4.

Table 2. 4 Summary of nanofluid droplet commonly used (unless noted specifically, all solvent is water).

Material	Concentration	Volume	Time	CA	Sub. Temp.	Ref.
Gold	100 ppm	~1.98 μL	~340 s	~84.8°	35.6 °C	[188]
Ag	0.1% <100 nm	~3 μL	~1340 s	~140°	22 °C	[189]
Fe_3O_4	1.0% -	~2.0 μL	~2760 s	~60°	25 °C	[190]
CuO	0.5% ~80 nm	~10 μL	~47 s	~73.5°	86.1 °C	[191]
Al_2O_3	0.4% ~40 nm	~0.5 μL	~310 s	~34°	22 °C	[192]
TiO_2-ethanol	0.1% <50 nm	~3 μL	~240 s	~44°	20 °C	[193]
SiO_2	~272 nm	~2.5 μL	~2120 s	~150°	22 °C	[194]
GNP*	0.1% -	~3 μL	~360 s	~10°	22 °C	[189]
Polystyrene	0.23% ~24 nm	~7 μL	~2600 s	~67.5°	25 °C	[195]

* Graphene Nanoplatelets (GNP)

Besides, Yan et al. [196] based on solar-driven gold nanofluid droplet evaporation, found that the evaporation would follow CCR mode on the hydrophilic surface. A similar process was also observed by Liu et al. [197] and Sefiane et al. [181] on heated glass and PTFE substrate, but on the hydrophobic surface would transform into SS mode. It may be due to the residual surface energy cannot be counteracted by pinning

force which is weakened during evaporation. Besides, Saroj et al. [190] based on the Fe_3O_4 nanofluid, found that SS and CCR mode and the CCA mode could also be observed on the PDMS substrate. They have also shown that both the static and receding contact angle of the nanofluid droplet could decrease with the increase of concentration, and consistent with the research by Shin et al. [182]. Moffat et al. [193, 198] based on the pure ethanol liquid droplet, found that the evaporation mode would change from CCA to the SS after the TiO_2 nanoparticles are added. They explained that it might be due to the pinning by nanoparticles' deposition being weak or the viscosity increased with the concentration. Yamada et al. [194] also revealed that with the increase of nanoparticles concentration, the contact line would be moving more continuously but not jump, which can be seen in Fig. 2.11 (a-c) and (d-f). It may due to contact line movement would be limited due to a large number of nanoparticles are deposited on the triple line region with high concentration, as shown in Fig. 2.11 (g-h). Therefore, the movement of the contact line would be more continuous with the concentration. The change of contact angle is for the same reason.

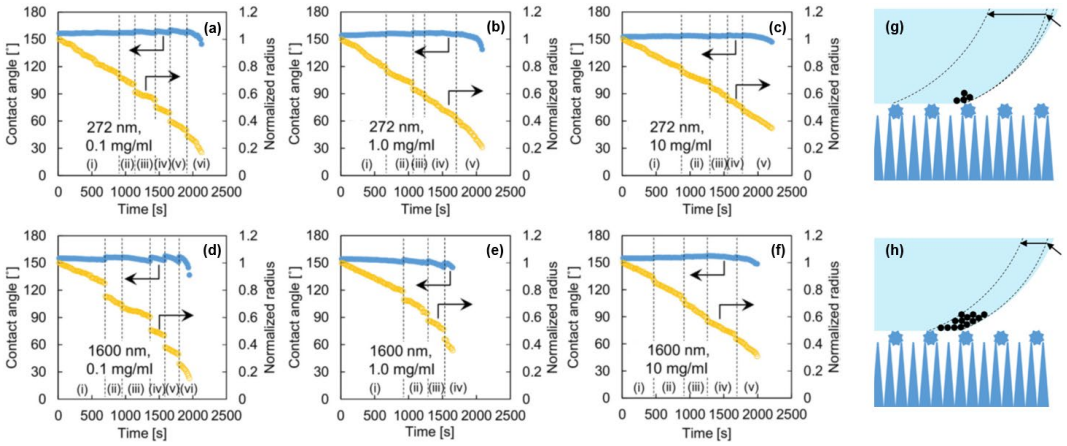


Fig. 2. 11 Schematics of particle behaviour in a droplet at (a) low and (b) high concentration [194].

Besides, there has a research focus on the nanoparticles combined with fuel droplet,

which improves its thermo-physical properties, such as the thermal conductivity, and found nanoparticle could improve the evaporation performance for colloidal suspension fuel droplets [199]. Therefore, the nanofluid droplet evaporation process has common to see in life. It is not difficult to conclude that all the nanoparticle concentration parameters, such as material, size, structure and even chemical properties, could influence the heat and mass transfer and wetting ability of nanofluid droplet during evaporation. It still has many nanofluid droplets' mechanism and characteristics that need to be studied deeply and have great significance to industry and scientific research.

2.4.2 Evaporation process of a droplet with added surfactant

Surfactants are self-assembled molecular clusters called micelles in solution. It could be adsorbed to the interface between the solution and other vapour or solid-phase [200]. It has been widely used in the industry and life [201, 202]. For sessile water droplets containing surfactants, the presence of surfactants will change the droplets' geometry during evaporation and affect the heat and mass transfer process and the surface tension distribution of the liquid-vapour interface. Therefore, the evaporation dynamics would be influenced interactively.

Many researchers have studied how surfactants can influence the droplet's evaporation rate for years. Moroi et al. [203] found that the surfactant could make the evaporation rate of the air-water interface covered by insoluble monolayer decrease and have no effect on the kind of air-water and air-surfactant solution interface, which also be found by Lunkenheimer et al. [204]. Gutiérrez et al. [205] also found that non-ionic and ionic

surfactant solutions could suppress the evaporation rate. However, Fang et al. [206] found that the surfactant can accelerate the evaporation of water droplets, which was also proved earlier [207, 208]. In response to this apparent contradiction, Nguyen et al. [26] noticed and proposed a new model which focused on the Hildebrand solubility parameter that could analyse the energy density of cohesion and does not need to consider the effect of both hydrophobicity of surface and the mode of evaporation. It can effectively solve the contradiction of the surfactant in the literature. Similarly, Zhou et al. [209] also observed this non-linear relationship between the evaporation rate and surfactant concentration. They found that the droplet evaporation time with surfactant on the hydrophilic cotton leaves would decrease when the concentration ranged from 0% to 0.01% but increased from 0.01% to 0.10%. This phenomenon may be due to the surfactant molecules, which could enlarge the liquid-vapour interface area initially, but with the increase of concentration, a self–assembled structure would be formed, and then the evaporation process would be suppressed.

Besides, the effect of surfactant on the contact line region was also studied in detail. Gokhale et al. [210] revealed that surfactant solutions mainly existed at the solid-liquid and liquid-vapour interface near the contact line. Simultaneously, they also found that compared with the pure ethanol liquid droplet, the contact line would be pinned after adding the surfactant so that the contact angle would decrease during the evaporation. The pinning of the contact line for the droplet with surfactant could be explained by Fig. 2.12, proposed by Nguyen et al. [26]. It can be seen that the concentration would increase during evaporation. Surfactant micelles take shape when the surfactant concentration is over the critical micelle concentration (CMC), which means that under

specific concentrations, the surface tension of water will decline [211]. The surfactant micelles will flow to the triple line region through the capillary flow, so the triple line is pinned due to the accumulation of surfactant finally, and the evaporation rate could also be influenced. Semenov et al. [212] put the SILWET L77 surfactant solution droplet on the hydrophobic surface. They found that the initial contact angle would be reduced with the increase of surfactant solution concentration. The evaporation process contains four stages (spreading, CCR, CCA and mixed modes), and CCR and CCA modes occupy the primary time during the evaporation. The surface tension would also be significantly influenced by surfactant, which could affect the evaporation mode. Marin et al. [213] found that the surface tension would decrease after adding the non-ionic surfactant polysorbate 80 (P80) into a large droplet, and the surface tension gradients would disappear when the concentration over the CMC. However, when the ionic sodium dodecyl sulfate (SDS) is in a small droplet, the surface tension would increase with the concentration below the CMC and decrease significantly at the triple line region when the concentration is above 2 CMC. Kim et al. [24] also found that a vital Marangoni recirculation would form inside biopolymer droplets with the existed of surfactant, which meets the previous study by Sefiane et al. [214], indicated that due to the non-uniform evaporation, the concentration of surfactant also would not be distributed evenly at the liquid-vapour interface so then the solute Marangoni flow be triggered.

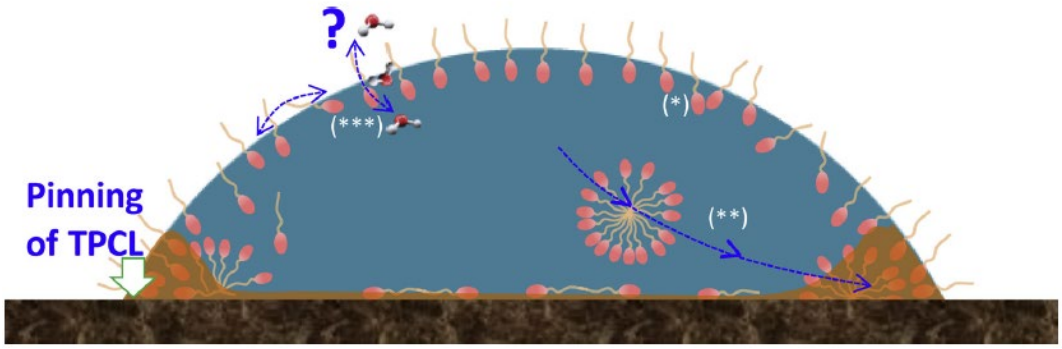


Fig. 2. 12 schematic about the influence mechanism of surfactants on droplet wetting and pinning [26].

Chapter 3. Effect of photoresist microstructure arrangement on droplet evaporation dynamics

Control of the wetting properties of functional surfaces is a desired functionality in many applications. In this chapter, the photoresist SU-8 was used as fabrication material. A silicon wafer was used as a substrate to prepare a biomimetic surface with hydrophilic properties and micro-pillars arranged in array morphology. The evaporation dynamics and heat and mass transfer processes of deionised water droplets on the bioinspired hydrophilic photoresist micro-pillar substrate were experimentally studied

3.1 Chapter introduction

Among the many parameters that affect the morphology of solid surfaces, surface roughness, as a parameter that determines surface texture and flatness, significantly affects the physical and chemical properties of the surface [215]. Naturally, research on the effect of roughness on biomimetic surface properties has also been widely conducted [216]. However, based on the literature review in Chapter 2, most of these studies on biomimetic surface roughness are based on biomimetic hydrophobic or superhydrophobic surfaces. In contrast, studies on biomimetic hydrophilic surfaces are rare. In addition, regarding the preparation process of bionic surfaces, many studies are based on etching micro-pillar structures to study the impact of surface configuration on the physical and chemical properties of bionic surfaces as well as droplet wettability and heat and mass transfer processes [217]. In this process, different materials will be tried to prepare micro-pillar structures, and the impact of their structural parameters on biomimetic surface properties will be studied [218]. As mentioned above, in addition to numerical simulation methods, the current preparation of surface bionic

microstructures is based on common metal or non-metallic materials. In contrast, based on semiconductor and electronic technology, the biomimetic structured surfaces prepared directly based on photoresist materials are rare. In summary, biomimetic functional surfaces are being increasingly studied due to their broad applicability and unique characteristics [219-221]. Among them, the design and processing of microstructures on bionic surfaces has become a significant research field. However, most of these studies are usually based on achieving hydrophobic or super-hydrophobic functions, and there are few studies on conventional hydrophilic biomimetic surfaces. In addition, various etching techniques are usually used to achieve pattern engraving on the substrate in the design of biomimetic surface microstructures. However, as an essential material in electronics, the production and research of biomimetic microstructures directly on photoresists based on photolithography technology is sporadic. Therefore, it becomes necessary to research photoresist-based biomimetic functional surfaces. Based on the above, in this chapter, SU-8 photoresist was selected to prepare hydrophilic biomimetic surface microstructures, and the surface roughness of the biomimetic surface was regulated by quantitatively controlling the spacing and height of the surface micro-pillars. The study in this chapter hopes to guide the design, fabrication and application of bionic functional surfaces based on photoresists.

3.2 Materials and experimental setup

The experimental devices and operation process used in this study are shown in Fig. 3. 1. The IR camera (FLIR A655sc, United States) is used to observe the temperature distribution of the liquid-vapour interface of the droplets. The droplet shape analyser

(Biolin Theta Flex, Sweden) measures the nanofluid droplet contact angle, contact line, and volume changes. Besides, the optical profilometer (KLA Zeta 20, United States) is also used in the study to measure the sedimentary pattern after evaporation. Meanwhile, the substrate is placed on a temperature-controlled heating panel. In this experiment, the temperature control in this article is achieved through a constant temperature water bath. A tubular heater is placed inside the water tank for heating. The internal sensor converts the water temperature into a resistance value, amplified by an integrated amplifier. It outputs a control signal to control the heating power of the electric heating tube to keep the water at a constant temperature between 50 ℃ and 80 ℃. Silicone grease (RS PRO, UK) is used between the substrate and the heating panel, reducing contact thermal resistance. And the droplets were extracted and placed using pipettes (Eppendorf Research plus, Germany) during the experiments. The ambient temperature of each test in the laboratory was controlled at 22 ± 2 °C, and the relative humidity was controlled at 55 ± 5%. In addition, in all experiments in this thesis, the emissivity of the infrared camera is uniformly set to 0.95.

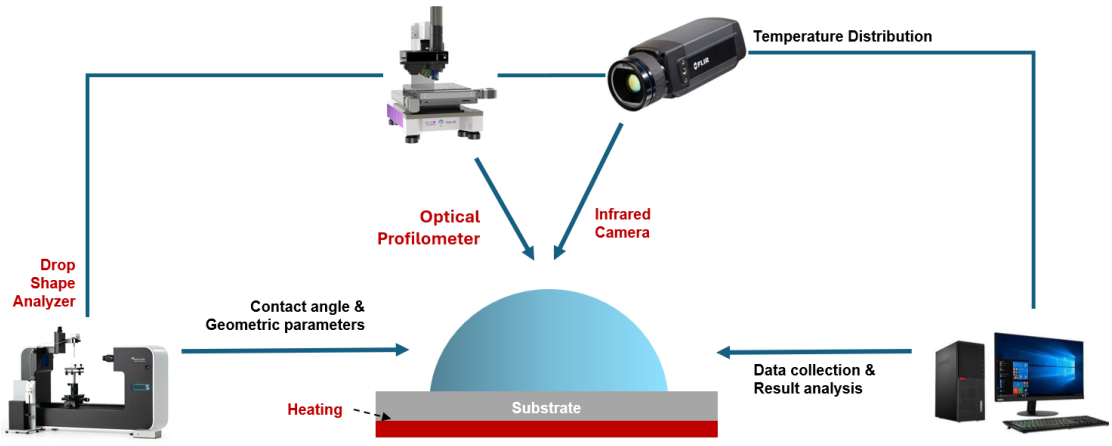


Fig. 3. 1 Experimental process and equipment schematic diagram.

Bionics is the invention of new science and technology based on the study of the structure and function of organisms. This process is also due to natural species richness and unique biological properties, and some typical examples are shown in Fig. 3.2 (a). The regular production of microstructures on the surface can maximise the quantitative control of the overall structural parameters of the biomimetic surface, such as roughness, which is conducive to subsequent research. Therefore, this study selected the method of etching micro-pillars on silicon wafers to realise the production of biomimetic functional surfaces and to carry out research on droplet wetting and heat and mass transfer characteristics. This study used negative photoresists SU-8 2010, which has the advantages of high chemical resistance, temperature resistance and good mechanical stability [222], to fabricate micro-pillars and the specific processing flow and method are shown in Fig. 3.2 (b). It is worth mentioning that due to the complexity of the micro-pillar processing process, it is difficult to control the height of the micro-pillars with extremely high accuracy. Therefore, in this thesis, the height of the micro-pillars is characterised by calculating the overall average height. Finally, six types of biomimetic surfaces were fabricated in this study, as shown in Fig. 3.2 (c). besides, a 3D optical profilometer also explicitly characterised its surface morphology, as shown in Fig. 3.2 (d). The specific configuration parameters of these bionic functional surfaces are shown in Table 3.1.

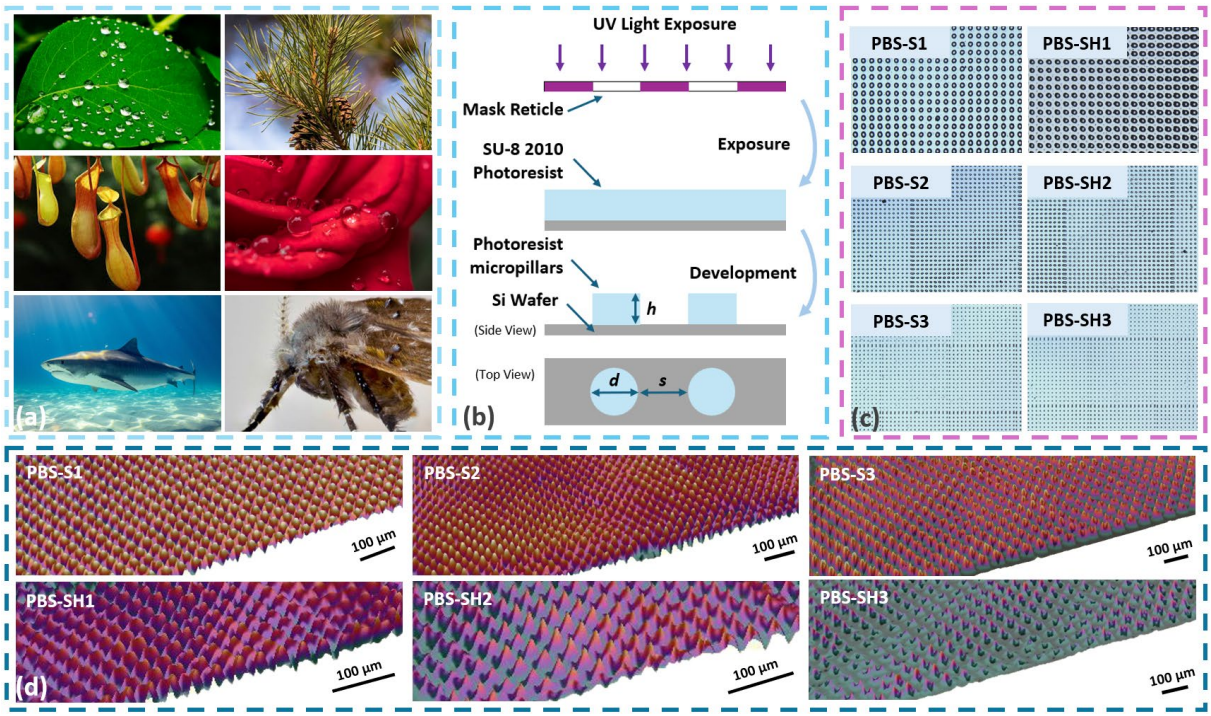


Fig. 3. 2 (a) Plant surfaces or animal skins with unique surface properties in nature; (b) Photoresist micro-pillar preparation process based on photolithography; (c) Different biomimetic surfaces under the microscope; (d) Biomimetic surface profile measured by an optical profilometer.

Table 3. 1 Parameters of biomimetic surface photoresist micro-pillars

	PBS-S1	PBS-S2	PBS-S3	PBS-SH1	PBS-SH2	PBS-SH3
Spacing **s** (μm)	15	20	40	15	20	40
Diameter **d** (μm)	20	20	20	20	20	20
Average height **h** (μm)	50	50	50	40	40	25
Roughness factor **r**	3.565	2.963	1.873	3.052	2.571	1.436

Table 3. 2 Some physical properties of the DI water under the condition of 60°C

	Density	Viscosity	Heat capacity	Surface Tension
DI water	0.98321 g/cm^3	0.4688 mPa·s	4.1843 J/(g·K)	66.18 mN/m

Besides, the droplet wetting study is mainly divided into the Wenzel state and the Cassie-Baxter state, and the Wenzel state equation could be defined as [46]:

$$\cos\theta_m = r\cos\theta_Y \tag{3.1}$$

and the roughness factor r in this study could be defined as:

$$r = \frac{(d+s)^2 + \pi \cdot d \cdot h}{(d+s)^2} \tag{3.2}$$

At the same time, the adhesion work is defined based on the Dupré equation [223] can be described as:

$$W_{AB} = Y_A + Y_B - Y_{AB} \tag{3.3}$$

where A and B mean phase or object, when the two objects are solid and liquid, respectively, the work of adhesion can also be described as:

$$W_{SL} = \sigma_S + \sigma_L - \sigma_{SL} \tag{3.4}$$

where σ_S means surface free energy, σ_L means surface tension of liquid, and σ_{SL} means interfacial tension between solid and liquid phase. Then, the simplified work of adhesion per unit area could be described as:

$$W_{PSL} = W_{SL}/A \tag{3.5}$$

where A is defined as the two-dimensional contact area of the liquid-vapour interface. Meanwhile, the average evaporation rate E_{avg} is defined as:

$$E_{avg} = M_0/T_{total} \tag{3.6}$$

$$M_0 = \rho_0 \cdot V_0 \tag{3.7}$$

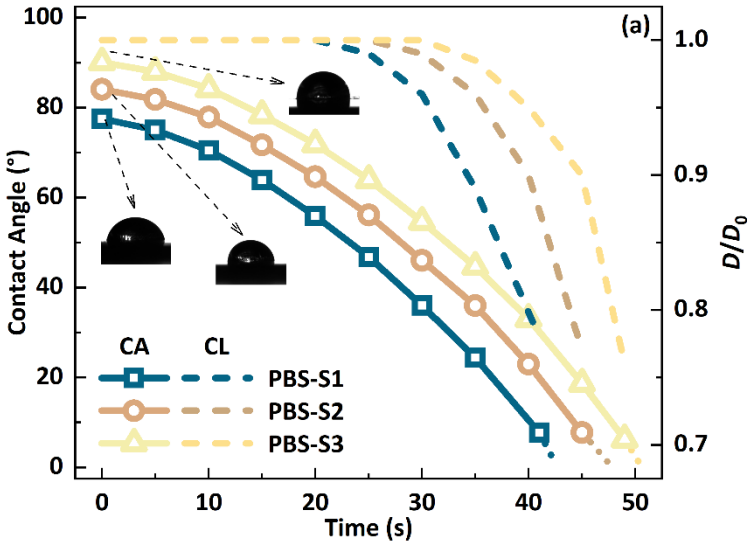
where M_0 and V_0 are the initial mass and volume of the droplet, respectively. T_{total} is the total evaporation time, and ρ_0 is the DI water density at 60℃.

3.3 Results and discussion

3.3.1 Effect of surface biomimetic pillar arrangement on droplet wetting properties

For biomimetic surfaces, the wettability has always been of excellent research significance. Therefore, this chapter first studied the wettability of biomimetic surfaces under different roughness conditions. The changes in the contact angle (CA) and dimensionless contact line (CL) with time when the droplet volume is 0.25, 0.5, 0.75 and 1.0 μL, respectively, are shown in Fig. 3.3 (a-d). It is worth noting that the change of the dimensionless contact line is expressed as D/D_0, where D_0 is the contact diameter of the droplet in the initial equilibrium state and D is the contact diameter in the real-time state. First, as shown in Fig. 3.3 (a), when a 0.25 μL DI water droplet evaporates on the three kinds of biomimetic surfaces, the initial contact angle increases by about 15% as the roughness increases. At the same time, the contact line of the droplet also shows the same change trend. In the initial stage of droplet evaporation, the contact line is in a pinned state. As the evaporation process proceeds, approximately in the middle and later period of the overall evaporation process, the contact line of the droplet begins to move and shrink until the end of evaporation, with an overall shrinkage of about 20%-30%. It can also be seen from this that the evaporation mode of the droplet goes through a constant contact radius (CCR) mode in the first half where the contact radius remains unchanged while the contact angle continues to decrease, and a mixed evaporation mode in the second half where both the contact angle and the contact line decrease simultaneously. At the same time, as shown in Fig. 3.3, the change trends of the contact angle and contact line of the droplet remain roughly the same when the

droplet volume increases. As a biomimetic surface with overall hydrophilicity, when its surface roughness increases, regardless of the size of the droplet volume, it will increase its surface wettability. This phenomenon is consistent with the description of the Wenzel equation, as shown in Eq. (3.1). Besides, the biomimetic surface will also impact the change of the droplet evaporation mode. As the roughness decreases, the time point of evaporation mode changes from CCR to mixed will also be later due to the increase in roughness delaying the time point when the surface tension of the liquid-vapour interface reaches the depinning force of the contact line. At the same time, in the observation process of the droplet contact angle, in some cases, the contact line of the droplet is not a perfect circle, which may cause specific errors in the observation of the contact angle. Still, it does not affect the observation of the change trend. Therefore, this error is acceptable in the research of this thesis, and this is hereby stated.



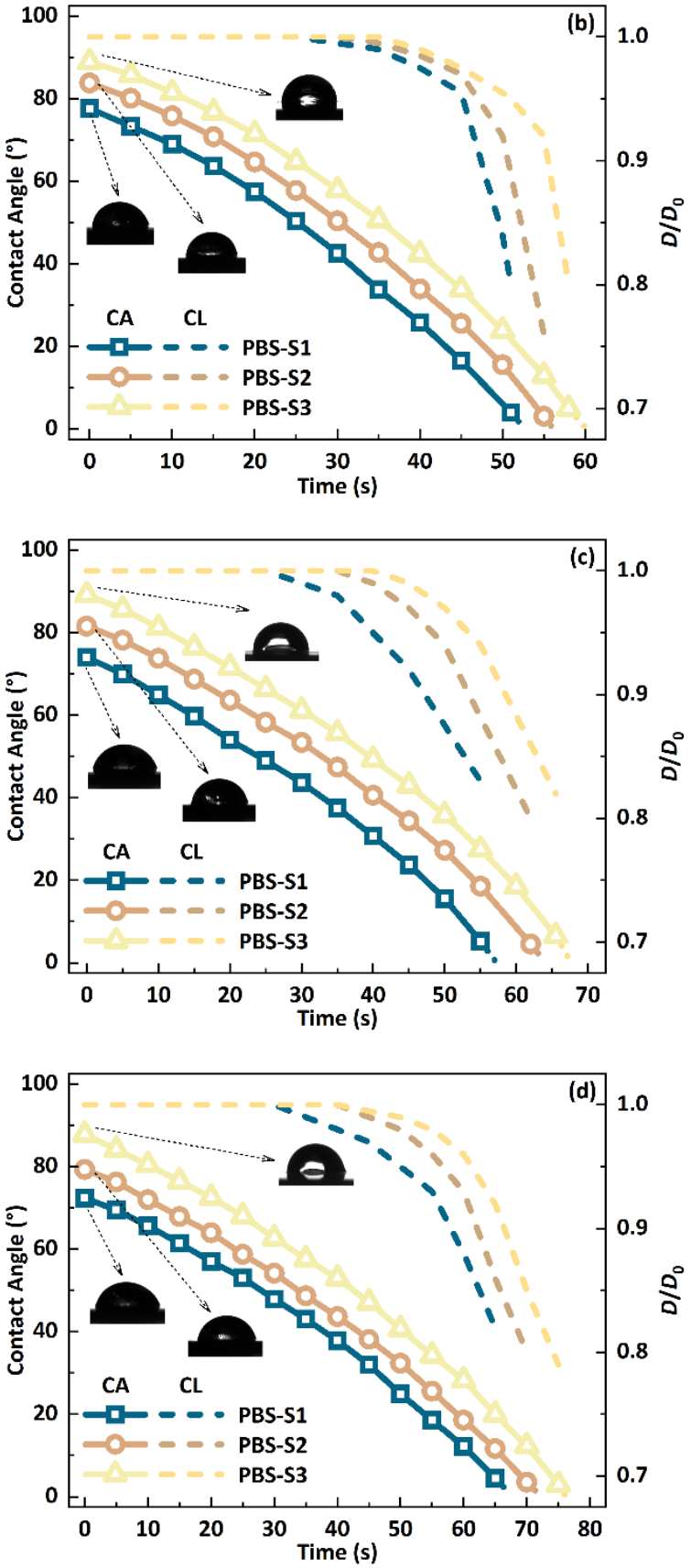
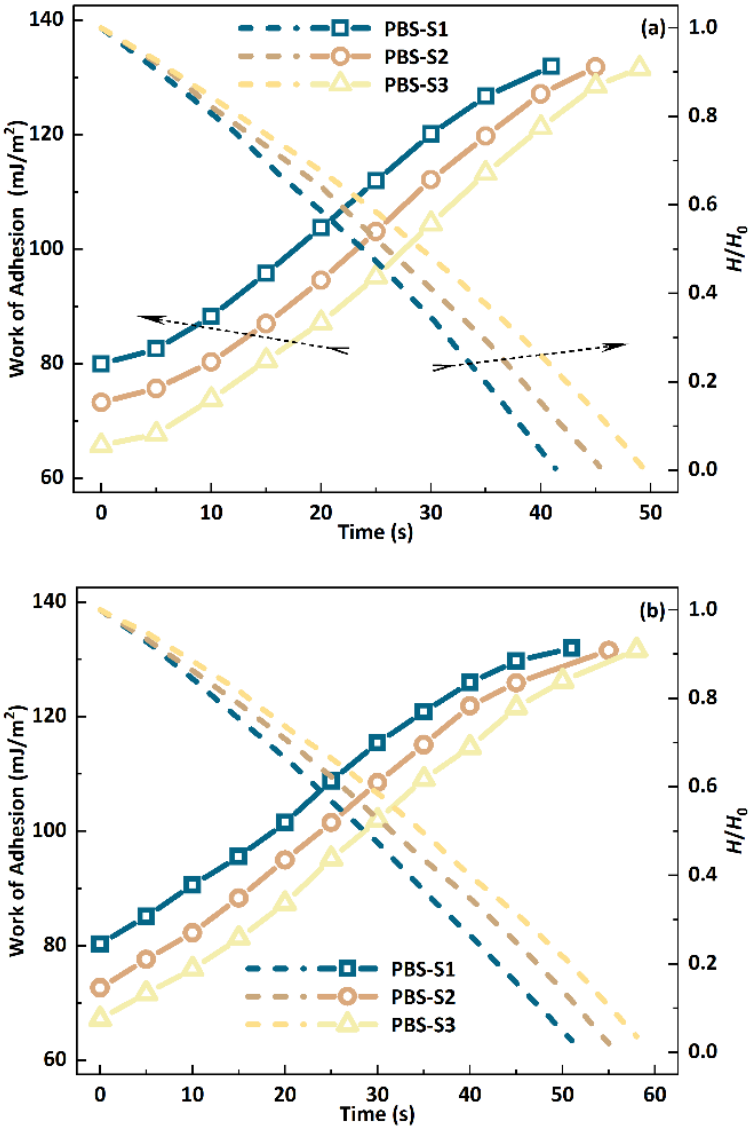


Fig. 3. 3 Changes of contact angle and dimensionless contact diameter of (a) 0.25 µL; (b) 0.5 µL; (c)

0.75 μL; (d) 1.0 μL DI water droplet on biomimetic surfaces over time.

At the same time, under different droplet volume conditions, the changes in the work of adhesion between the three biomimetic surfaces of PBS-S1, PBS-S2, and PBS-S3 and the DI water droplets are shown in Fig. 3.4 (a-d). It is worth mentioning that the work of adhesion, as an essential concept in interfacial physical chemistry, is of great significance in describing the characteristics of interfaces. Assuming that the surfaces of two immiscible objects are in contact with each other, the physical meaning of adhesion work is the work required to separate the two objects [224]. This chapter uses the simplified per unit area work of adhesion (W_{PSL}) for description, and the specific calculation principle is shown in Eq. (3.3-3.5). Taking 0.25 μL of DI water as an example, as shown in Fig. 3.4 (a), the work of adhesion between the droplet and the biomimetic surface decreases as the roughness declines, and the adhesion work of the liquid-solid interface decreases by about 17% when the surface changes from PBS-S1 to PBS-S3. At the same time, with the droplet volume increase from 0.25 μL to 1.0 μL, the changing trend of the work of adhesion remains consistent. That is, the influence of the change of the biomimetic surface roughness on the change of the adhesion work will not change with the change of the droplet volume. This is because the work of adhesion is one of the biomimetic surface properties, and the biomimetic surface microstructures play a dominant role in it by changing the wettability. Besides, the variation trend of the dimensionless height (H/H_0) of the droplet is also shown in Fig. 3.4 (a-d), where H_0 is the initial height of the droplet, and H is the real-time height of the droplet. As the surface roughness increases, the rate of change of the dimensionless droplet height also increases, and this trend is not affected by the droplet volume. This

can also be attributed to the increase in roughness, which enhances the mass transfer rate at the droplet liquid-vapour interface.



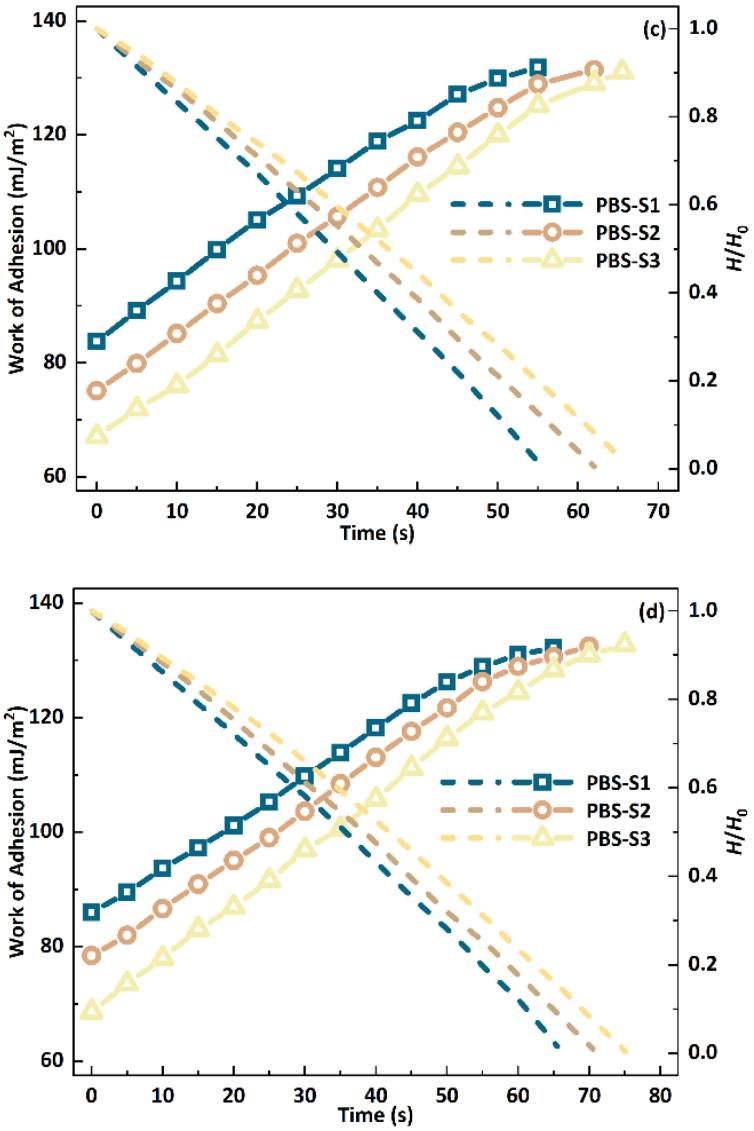
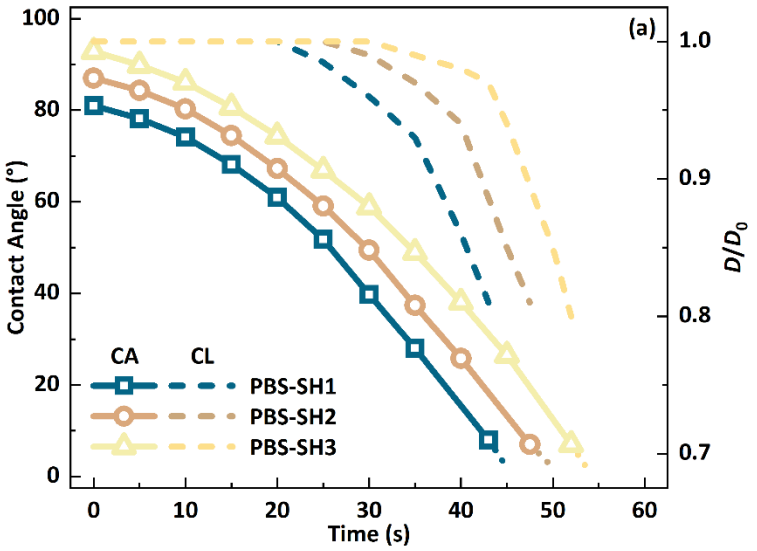


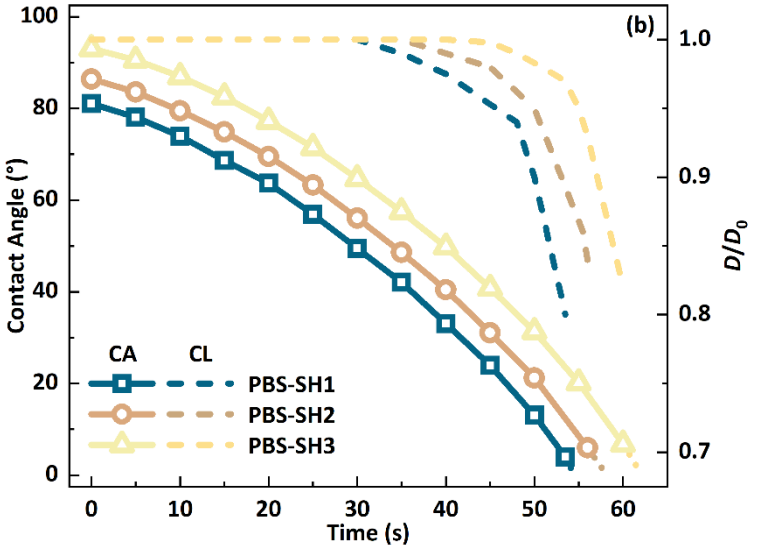
Fig. 3. 4 Variation of work of adhesion (WPLS) with (a) 0.25 μL; (b) 0.5 μL; (c) 0.75 μL; (d) 1.0 μL DI water droplets on different biomimetic surfaces over time.

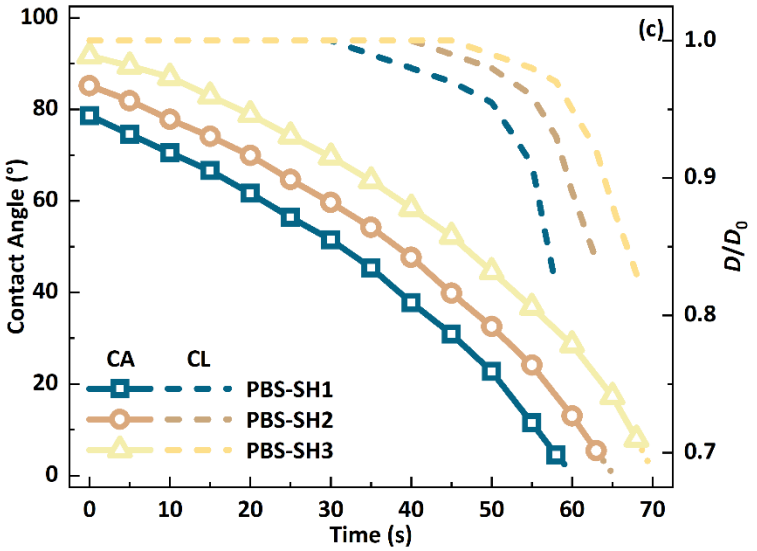
3.3.2 Effect of surface biomimetic pillar height on droplet wetting properties

In the above, we describe how to change the roughness of the biomimetic surface by changing the micro-pillar spacing and then explore its effect on wettability. In this section, based on the same spacing arrangement, the height of the micro-pillars is changed to study the effect of the change in their roughness on the wettability of the

biomimetic surface. After changing the height, the biomimetic surfaces are named PBS-SH1, PBS-SH2 and PBS-SH3, respectively. The wetting phenomenon and evaporation characteristics of the DI water droplets on these biomimetic surfaces are shown in Fig. 3.5 (a-d). As shown in Fig. 3.5 (a), when the volume of the droplet is 0.25 μL, as the surface roughness of the droplet increases, the contact angle declines by about 13%. The evaporation mode of the droplets still undergoes a transition from the CCR mode to the mixed mode. As the roughness decreases, the time node of the droplet evaporation mode transition is also delayed. At the same time, when the droplet volume increases to 0.5 μL, 0.75 μL, and 1.0 μL, it can be seen from Fig. 3.5 (b-d) that the change trends of the wetting characteristics on the biomimetic surface remain unchanged. And the evaporation process of the droplet also goes through the two modes of CCR and mixed. In summary, when the roughness of the biomimetic surface is controlled by changing the height of the micro-pillars, the evaporation process of the DI water droplets still follows the same change law described before. It can also be seen that the change in the height of the micro-pillars has no noticeable effect on the transformation of the evaporation mode. The change in surface roughness still has the dominant influence on the evaporation process of droplets.


(a)
Contact Angle (°)
D/D0
Time (s)
CA
CL
PBS-SH1
PBS-SH2
PBS-SH3


(b)
Contact Angle (°)
D/D0
Time (s)
CA
CL
PBS-SH1
PBS-SH2
PBS-SH3


(c)
Contact Angle (°)
D/D0
Time (s)
CA
CL
PBS-SH1
PBS-SH2
PBS-SH3

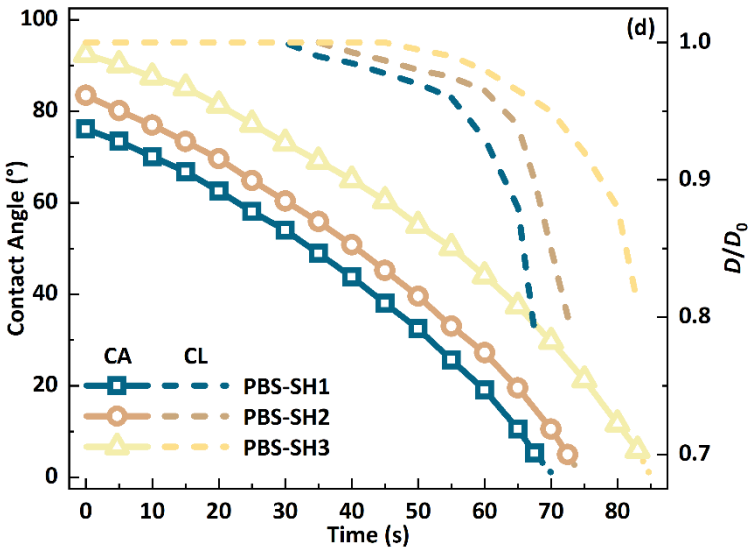
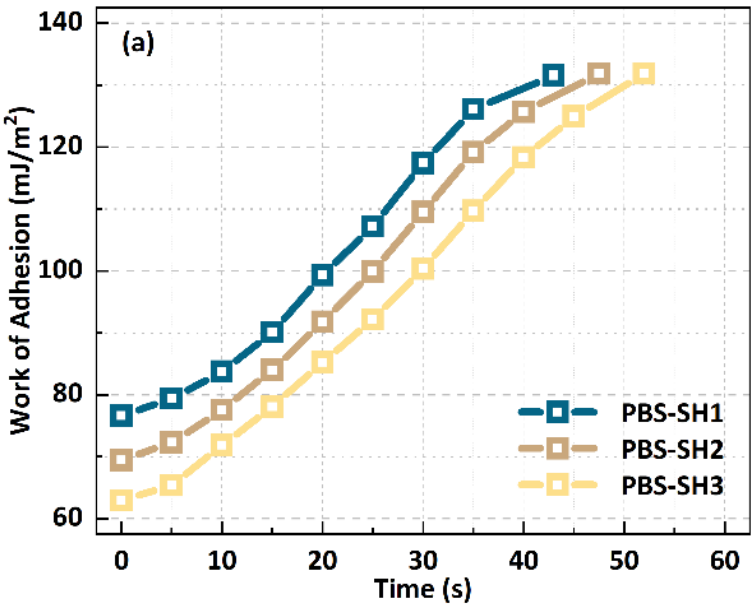
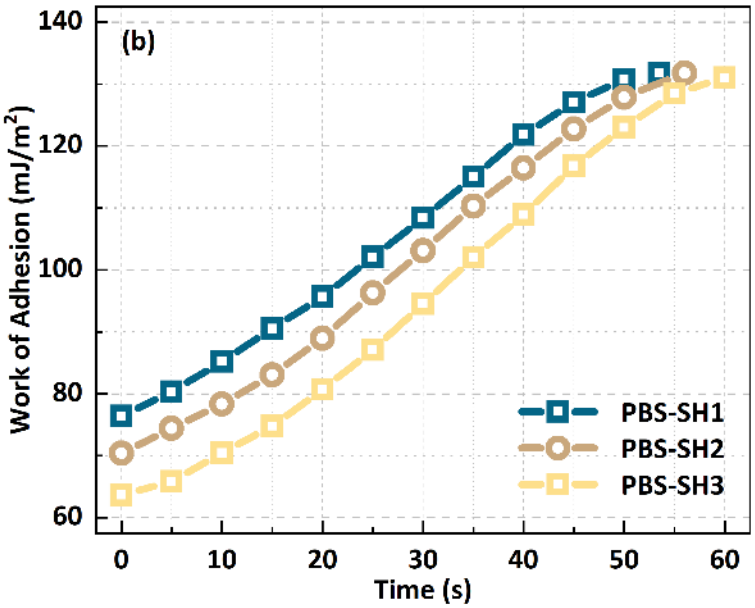


Fig. 3. 5 Changes of contact angle and dimensionless contact diameter of (a) 0.25 μL; (b) 0.5 μL; (c) 0.75 μL; (d) 1.0 μL DI water droplet on biomimetic surfaces over time.

At the same time, after the height of the micro-pillar structure on the biomimetic surface changes, the work of adhesion between the droplet and the biomimetic surface is shown in Fig. 3.6 (a-d). As shown in Fig. 3.6 (a), when a 0.25 μL DI water droplet was placed on the PBS-SH1 surface, its initial work of adhesion was about 76 mJ/m^2. In contrast, when the droplet was placed on the PBS-SH2 and PBS-SH3 surfaces, the work of adhesion decreased to about 69 and 62 mJ/m^2, respectively, also reduced by about 10% and 18%, respectively. This can be attributed to the fact that as the roughness of the biomimetic surface decreases, the wettability of the biomimetic surface also weakens, reducing the work of adhesion at the solid-liquid interface of the droplet. At the same time, as the droplet volume increases from 0.25 μL to 1.0 μL, as shown in Fig. 3.6 (b-d), on these three kinds of biomimetic surfaces, the work of adhesion between the droplet and the surface keeps following a trend of gradually increasing as the evaporation process proceeds. As the evaporation reaches the final phase, no matter on what kind of surface, the work of adhesion between the droplet of each volume and the

biomimetic surface will approach about 132 mJ/m^2, which is jointly determined by the biomimetic surface characteristics and the physical properties of DI water. The most significant difference is that the work of adhesion on the PBS-SH3 surface always reaches the constant value at the latest, which can be attributed to its surface having the worst hydrophilicity.





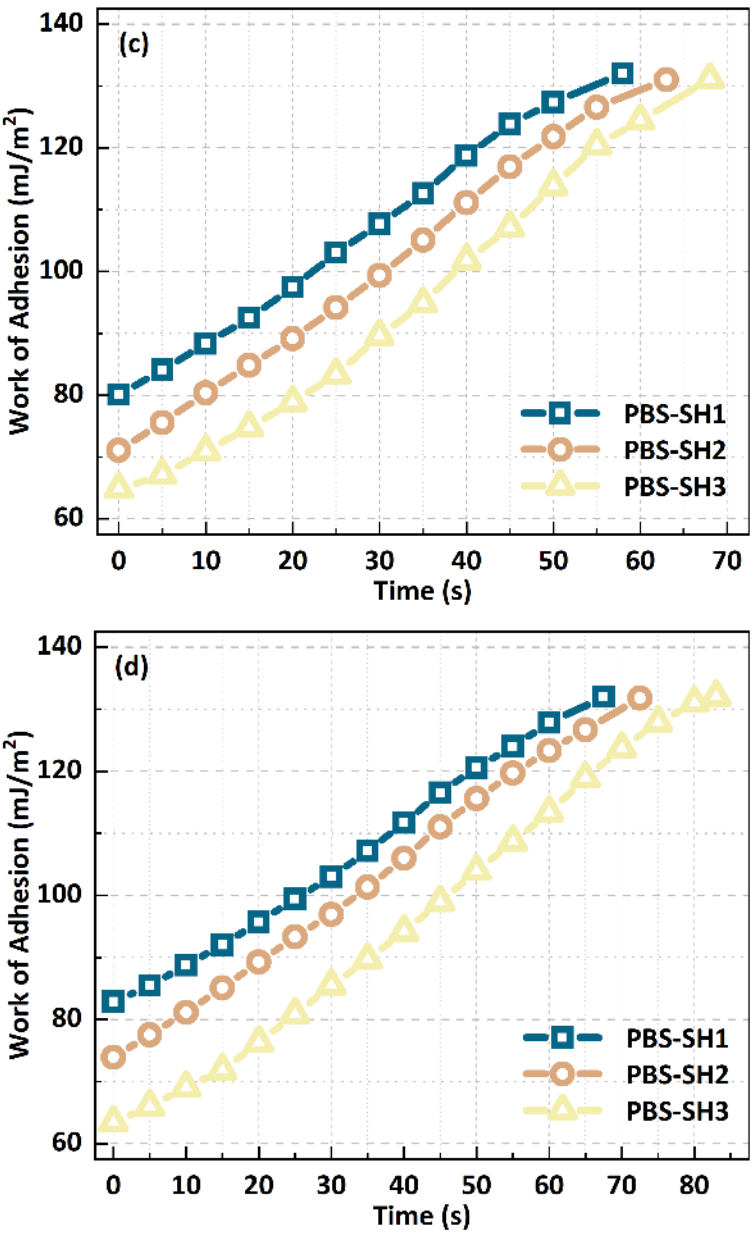


Fig. 3. 6 Variation of work of adhesion (WPLS) with (a) 0.25 μL; (b) 0.5 μL; (c) 0.75 μL; (d) 1.0 μL DI water droplets on different biomimetic surfaces over time.

In addition, to comprehensively compare the effects of biomimetic surfaces of various structures on the wetting characteristics of droplets with different volumes, the changes in the initial equilibrium angle of the droplet with surface parameters were sorted out, as shown in Fig. 3.7 (a). As seen in Fig. 3.7 (a), the initial equilibrium contact angle of the droplet is linearly related to the roughness of the biomimetic surface. That is, as the

surface roughness increases, the contact angle of the droplet declines. For example, when the droplet volume is 0.25 μL, as the roughness increases, the contact angle can decline from about 92° to about 77°, a reduction of about 17%. At the same time, it can also be seen from Fig. 3.7 (a) that when the volume of the droplet increases to 0.5 μL, 0.75 μL, and 1.0 μL, respectively, the maximum decrease in the initial equilibrium contact angle of the droplet can also reach 16%, 19%, and 22%, respectively. The reason for this phenomenon can be attributed to the different sizes and arrangements of the micro-pillar structures on the biomimetic surface, which will significantly change the overall surface roughness and then, based on the Wenzel state of the droplet, will have a crucial impact on the wettability of the biomimetic surface and the apparent contact angle of the droplet. At the same time, the droplet volume also has a minor effect on the initial equilibrium contact angle. For example, on the PBS-SH3 surface, the initial equilibrium contact angle does not change significantly when the droplet volume increases from 0.25 μL to 0.5 μL but decreases by about 5% when the volume increases to 1.0 μL. The reason for this phenomenon is the same as described before. It has nothing to do with the wettability of the biomimetic surface but mainly depends on the effect of gravity. Therefore, the larger the droplet volume, the more pronounced the gravity effect (overcoming the surface tension of the liquid-vapour interface), and the more significant the reduction in the contact angle. In addition, based on the series of biomimetic surfaces, the variation in the magnitude of the adhesion work of DI water droplets with different volumes is shown in Fig. 3.7 (b). Like the initial equilibrium contact angle, the initial adhesion work also shows an apparent linear relationship with the roughness of the biomimetic surface. The more significant the surface roughness, the greater the work of adhesion, and the maximum increase is approximately 23%.

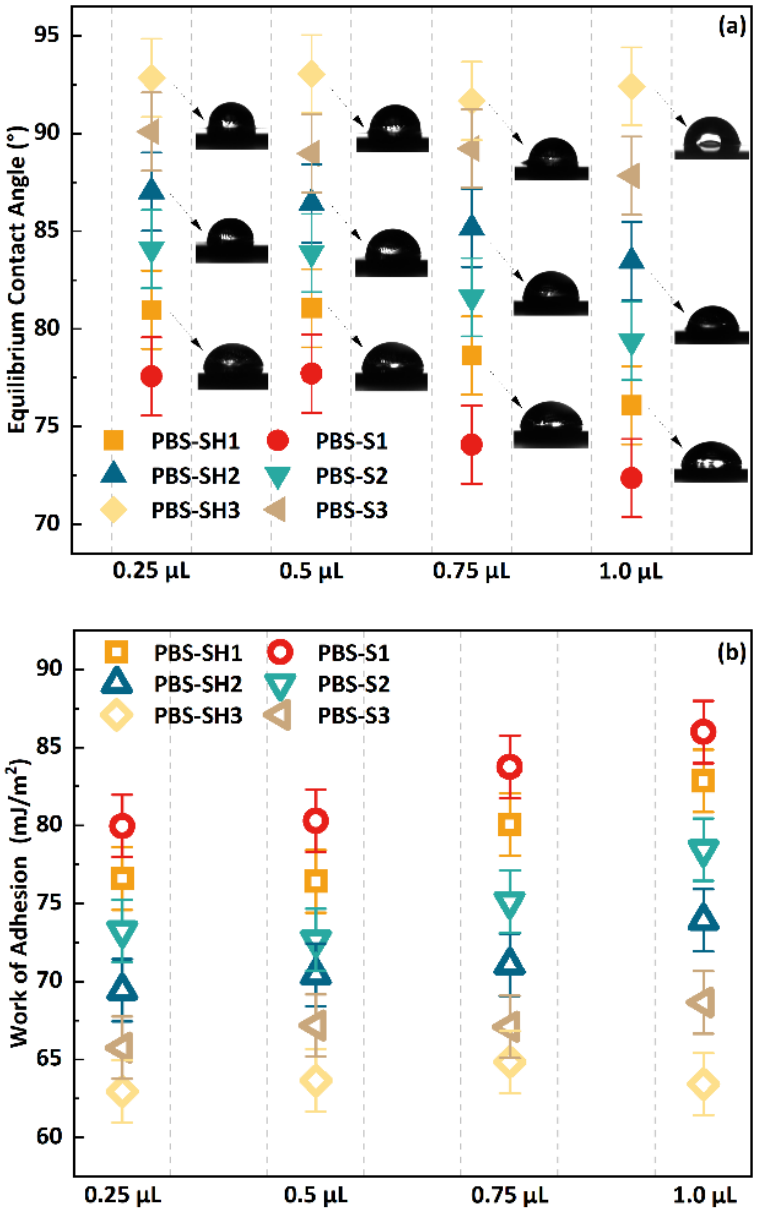


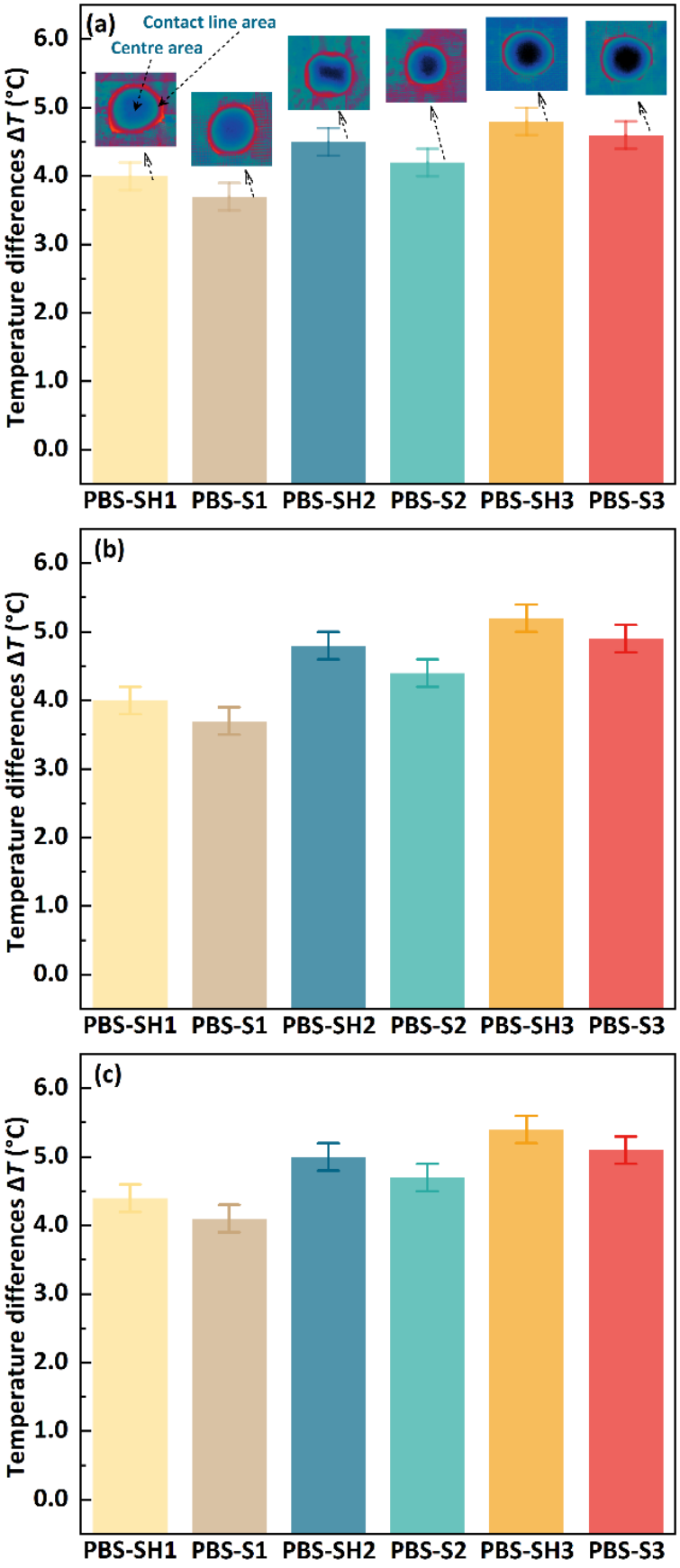
Fig. 3. 7 (a) Changes in the initial equilibrium contact angles of droplets of different volumes on biomimetic surfaces with roughness degrees; (b) the work of adhesion corresponding to different initial equilibrium contact angles.

3.3.3 Effect of surface roughness on droplet heat and mass transfer process

The previous mainly introduced the effects of biomimetic surfaces with a series of microstructures on the wetting characteristics of DI water droplets. In addition to the

wetting state of the liquid-solid interface, different biomimetic surfaces will also significantly impact the heat and mass transfer process at the liquid-vapour interface of the droplets, which will be discussed in this section. Firstly, the temperature difference ΔT between the droplet centre and the contact line areas is defined. It can be used to describe the strength of the evaporative cooling effect, which is usually caused by evaporation from the interface [97]. At the same time, Fig. 3.8 (a-d) shows that ΔT will also change under different biomimetic surfaces. As the surface roughness increases, the ΔT of the droplet will decrease significantly. For example, when a 0.25 μL DI water droplet evaporates on the biomimetic surface, as shown in Fig. 8 (a). When the droplet is placed on the PBS-SH3 surface, ΔT is about 4.8 °C. In contrast, when the droplet is placed on the PBS-S3 and PBS-SH1 surface, ΔT is about 4.6 °C and 4 °C, which decreases by about 4% and 17%, respectively. This phenomenon can be attributed to the fact that when the roughness of the biomimetic surface increases, the surface wettability is enhanced. The contact angle of the droplet is reduced, which enhances the heat transfer process inside the droplet and improves the temperature uniformity of the liquid-vapour interface while also inhibiting the evaporative cooling effect of the liquid-vapour interface. At the same time, at the initial equilibrium moment of the droplet, the infrared thermal images of a 0.25 μL droplet on different biomimetic surfaces are shown in the inset of Fig. 3.8 (a). The liquid-vapour interface of the droplet has a pronounced evaporative cooling effect at the initial moment and produces an apparent temperature gradient distribution. Afterwards, as shown in Fig. 3.8 (b-d), when the droplet volume increases from 0.25 μL to 1.0 μL, the ΔT change trend of the liquid-vapour interface remains unchanged. It maintains a linear relationship with the roughness degree. Under various droplet volume conditions, the ΔT difference

between the PBS-S1 and PBS-SH3 surfaces can vary by 34%.



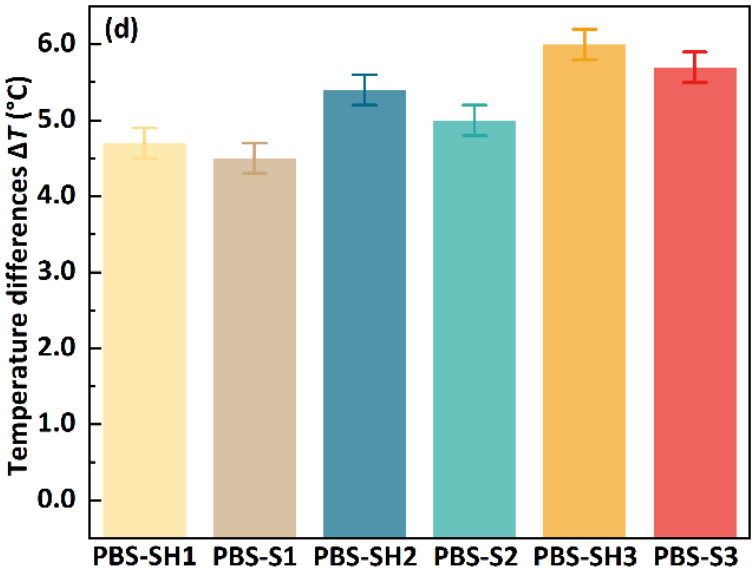


Fig. 3. 8 The temperature difference between the central and contact line region of (a) 0.25 μL; (b) 0.5 μL; (c) 0.75 μL; (d) 1.0 μL droplet on different biomimetic surfaces.

Meanwhile, the temperature distribution of the droplet liquid-vapour interface changes with time is shown in Fig. 3.9, where t_{total} refers to the total evaporation time of droplet. Fig. 3.9 (a) and (b) show the evaporation process of a 0.5 μL DI water droplet on the PBS-SH3 and PBS-S3 surfaces, respectively. As the evaporation process proceeds, the temperature distribution at the droplet liquid-vapour interface tends to be uniform. This can be attributed to the dual effects of enhanced thermal conductivity inside the droplet and weakened evaporative cooling effect on the interface. It can also be seen that at the same time point, the temperature distribution inhomogeneity at the droplet liquid-vapour interface on the PBS-SH3 surface is more evident in the early stage. In contrast, the difference in temperature distribution between the two surfaces is not significant in the later stage.

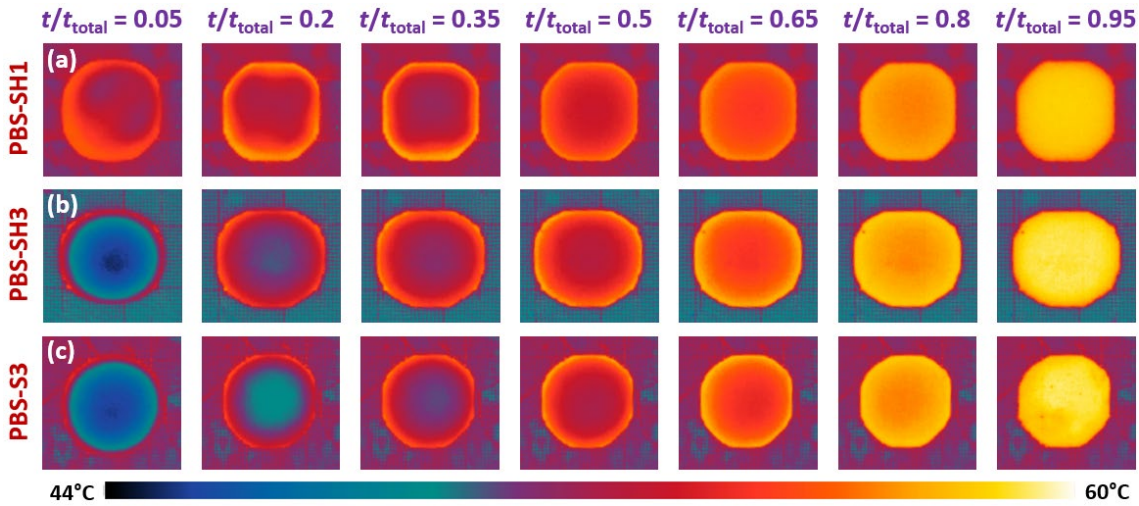
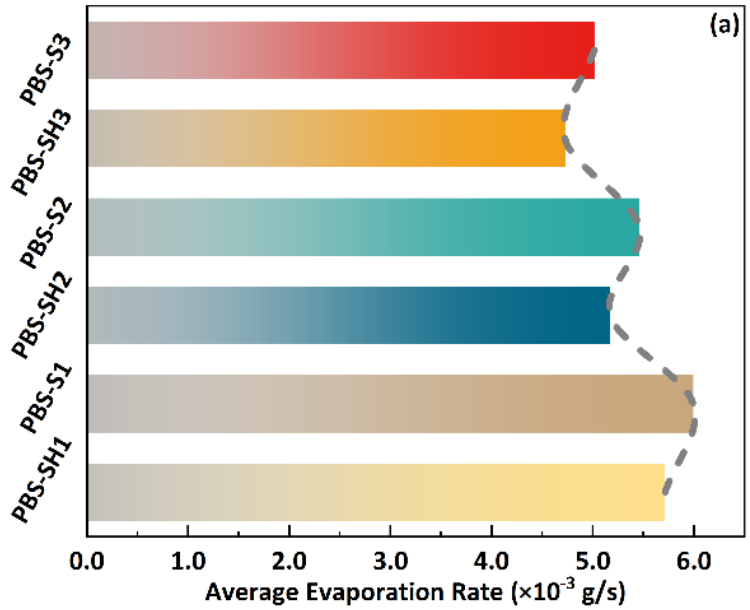
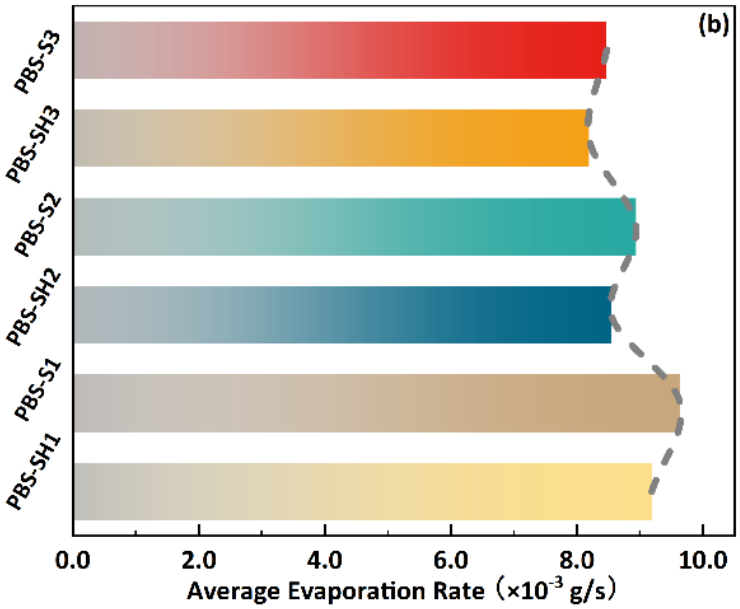


Fig. 3. 9 Evolution of the temperature distribution at the liquid-vapour interface of a 0.5 μL droplet on the (a) PBS-SH1, (b) PBS-SH3, and (c) PBS-S3 surfaces.

In addition, different biomimetic surfaces will also affect the mass transfer process, which will significantly impact the evaporation rate of droplets. As shown in Fig. 3.10 (a-d), the average evaporation rate of the droplet during the entire evaporation process is aggregated, which is defined as Eq. (3.6-3.7), showing the effect of different biomimetic surfaces on the evaporation rate. It can be seen from Fig. 3.10 (a) that as the biomimetic surface roughness increases, the sessile droplet average evaporation rate also rises. For example, when the droplet is converted from the PBS-SH3 surface to the PBS-S1 surface, the average evaporation rate increases from 4.73×10^{-3} g/s to 6.0×10^{-3} g/s, improving about 27%. Meanwhile, when the droplet volume increases from 0.25 μL to 1.0 μL, the average evaporation rate of the droplet on different biomimetic surfaces is shown in Fig. 3.10 (b–d). At the same time, when the droplet volume increases from 0.25 μL to 1.0 μL, the average evaporation rate of the droplet on different biomimetic surfaces is shown in Fig. 3.10 (b-d). The change in the droplet volume does not affect the trend of the average evaporation rate. When the droplet volume is 0.5 μL,

0.75 μL and 1.0 μL, the maximum increase in the average evaporation rate is 17%, 28% and 17%, respectively.





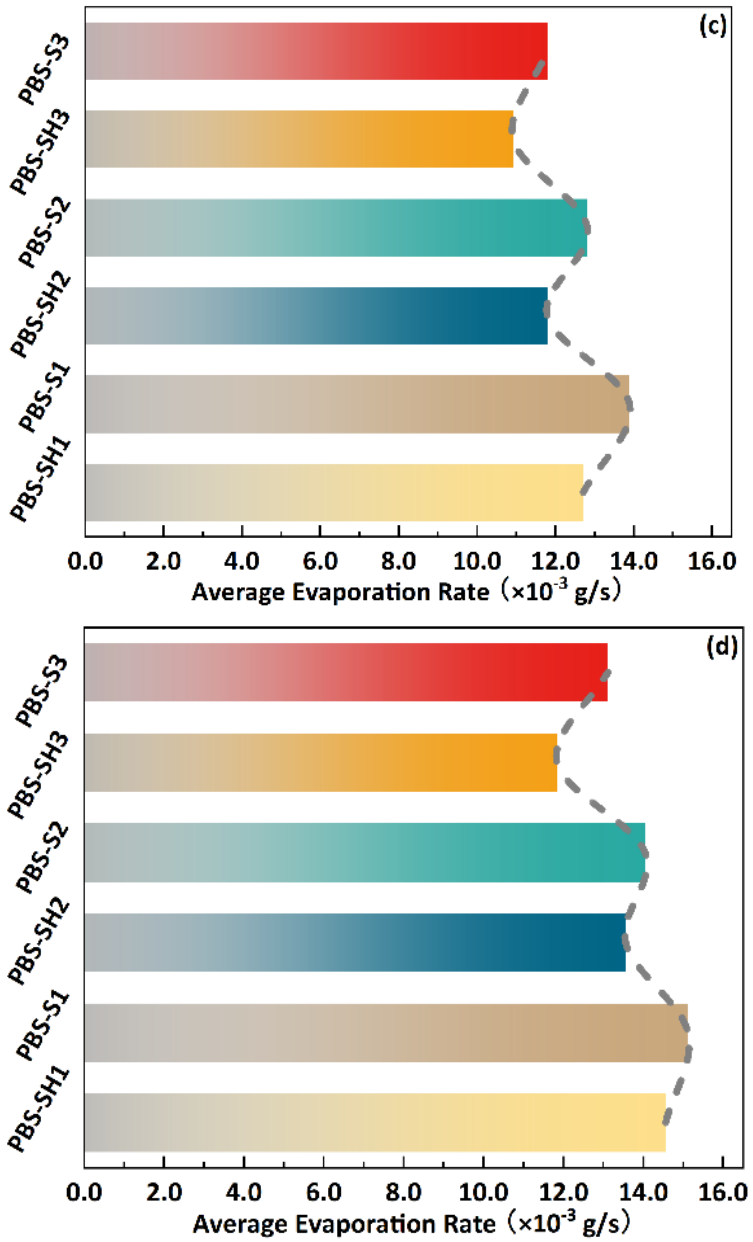


Fig. 3. 10 Average evaporation rate of (a) 0.25 μL; (b) 0.5 μL; (c) 0.75 μL; (d) 1.0 μL droplet located on different biomimetic surfaces.

3.4 Chapter summary

In this study, the bioinspired micro-pillar structures were fabricated on a silicon wafer based on a photoresist material SU-8, and the biomimetic surface roughness was precisely controlled by quantitatively controlling the size and arrangement of the micro-

pillars. First, this study set three different micropillar spacings: 15 μm, 20 μm, and 40 μm. The results show that the surface roughness gradually decreases as the spacing increases, weakening the biomimetic surface wettability. The biomimetic surface will also cause the evaporation mode of DI water droplets to change from CCR mode to mixed mode. At the same time, the changing trend of the work of adhesion between the biomimetic surfaces with different microstructures and the droplets is also different. The smaller the roughness, the lower the adhesion work for droplets of the same volume. After that, at the corresponding spacing, this study also adjusted the micro-pillar average height from 50 μm to 40 μm and 25 μm. In addition, after adjusting the height of the micro-pillars, the surface roughness changes, affecting the biomimetic surface wettability. Considering the combined effects of the micro-pillar spacing and height, the results show that as the surface roughness increases, the wettability of the photoresist biomimetic surface gradually increases. The contact angle can be reduced by up to about 22%, enhancing the adhesion work between the droplet and the biomimetic surface by up to 23%. There is an apparent linear relationship between them, which can all be controlled based on the design of the microstructures. Similarly, the microstructure of the biomimetic surface will also affect the droplet heat and mass transfer process. During the evaporation process, apparent evaporative cooling will occur at the liquid-vapour interface of the droplets, and this phenomenon will become more evident as the roughness increases. The temperature difference between different surfaces can be increased by up to 34% on average. At the same time, this phenomenon will also inhibit the overall average evaporation rate by up to 28%. This study demonstrates the feasibility of preparing hydrophilic biomimetic surfaces based on the photoresist. At the same time, by regulating the parameters of the surface microstructure,

the wettability of the biomimetic surface can be precisely controlled, thereby affecting the interfacial heat and mass transfer process. This study is expected to help expand the application of biomimetic surfaces in manufacturing electronic devices.

Chapter 4. Effect of the photoresist microstructure configuration on droplet evaporation dynamics

As the cornerstone of the electronic manufacturing field, the photolithography process determines the performance of advanced electronic equipment and products mentioned above [225, 226]. Therefore, applying photolithography technology to prepare functional surfaces is significant to the design of electronic equipment. In this chapter, based on photolithography technology, SU-8 photoresist was still used as raw material to prepare biomimetic surfaces with microstructures in various arrangements, and the micro-pillar structure will have cylindrical and square structures. The study in this chapter aims to guide the optimal design of biomimetic surfaces prepared based on photoresist.

4.1 Chapter introduction

The functional biomimetic surfaces can give the surface the required unique functions by simulating the various microstructures, physics, chemistry, and other characteristics of the surface or skin of plants and animals, which have broad application prospects [227, 228]. Especially with the development of the electronics industry, applying photolithography technology to prepare biomimetic surfaces is significant to the bionic design of electronic equipment. Regarding the preparation of biomimetic functional surfaces, whether using photolithography or other means, the design of biomimetic surface microstructures is always crucial, and an essential part of this is the choice of micro- and nanostructure configuration [229, 230]. Still, most of the research is based on achieving the super-hydrophobic properties of the biomimetic surface [231], and research based on conventional hydrophilic biomimetic surfaces or transformation of

surface wettability is still relatively rare. Besides, in the preparation process of biomimetic functional surfaces, in addition to the design as mentioned above of the surface configuration, choosing the material used to fabricate the microstructure also has a crucial influence on the overall performance of the biomimetic surface [232, 233]. However, research on biomimetic functional surfaces directly based on photoresist materials is still rare, and the influence of photoresist material characteristics on the wetting properties of biomimetic surface microstructures remains to be studied. Therefore, in this chapter, the SU-8 photoresist is still used to prepare biomimetic functional surfaces with various microstructures on silicon substrates based on bio-inspiration. The work in this chapter explores the influence of biomimetic surface microstructure design on wettability and the effective properties of biomimetic microstructures in photoresists.

4.2 Material and experimental setup

The bionic functional surface in this study is designed based on the concept of bionics, which was proposed in 1958, and the term “Biomimetics” evolved in 1991 [234]. As shown in Fig. 4.1 (a), plant surfaces and animal skin in nature will have some unique characteristics, and then, based on observing the microstructure of their surfaces, bionic microstructures can be designed. Among a series of bionic microstructures, etching the micro-pillar on the surface is one of the most widely used design strategies [235, 236]. Based on this, as shown in Fig. 4.1 (b), this study also used SU-8 as raw material to prepare micro-pillar structures on the silicon wafer to realise the preparation of biomimetic functional surfaces. The morphology of the prepared biomimetic functional

surface is shown in Fig. 4.1 (c). Some physical properties of the photoresist SU-8 2000 series are shown in Table 1.

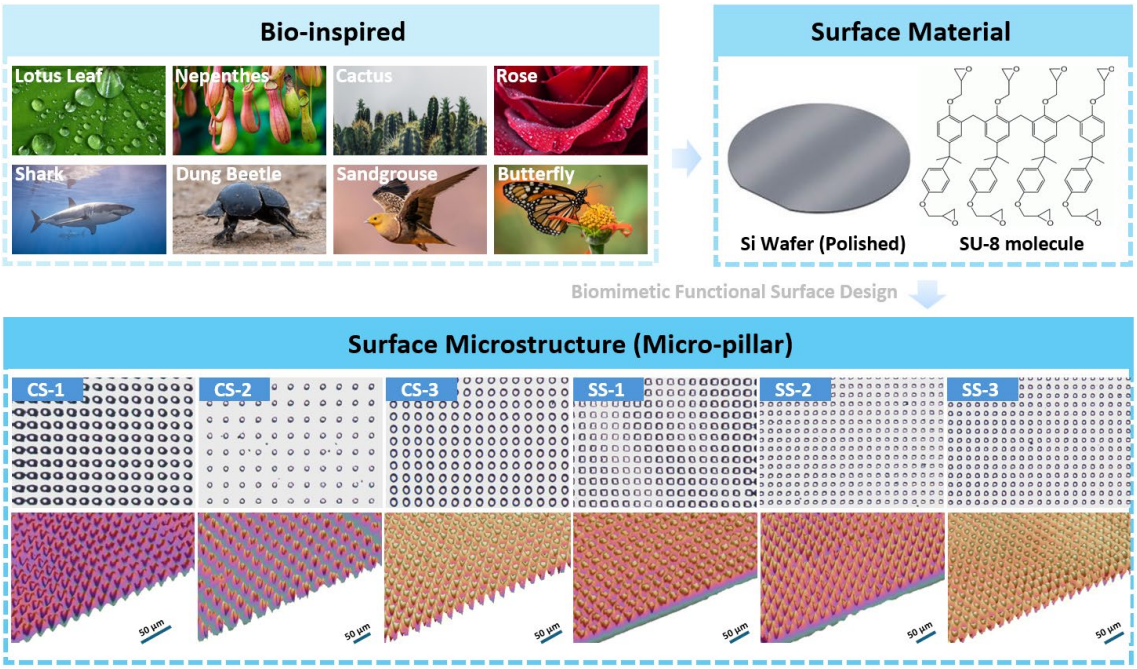


Fig. 4. 1 Bio-inspired preparation process of biomimetic functional surfaces.

Table 4. 1 Basic physical properties of photoresist SU-8 2010

Physical Properties	Approximate Values
Glass Transition Temperature (°C)	210
Thermal Stability (°C @ 5% wt. loss)	315
Thermal Conductivity (W/mK)	0.3
Coeff. of Thermal Expansion (ppm)	52
Adhesion Strength (mPa)	38

The specific process of preparing the micro-pillar structure on the silicon wafer surface is shown in Fig. 4.2. As shown in the figure, the substrate is first cleaned with acetone solvent, and after cleaning, it is baked at 200°C for 30 minutes to remove surface water

molecules. After that, the SU-8 photoresist is dispersed and spin-coated onto the substrate surface using a spinner. The photoresist is then soft-baked and then slowly cooled. After that, the photoresist is exposed to ultraviolet light through a mask reticle to prepare the desired pattern and a solvent is used to remove the unexposed areas. Then, the final stage is to hard bake the photoresist at 150-200°C to permanently solidify it, ultimately obtaining the microstructure required for the design. Meanwhile, it also can be seen in Fig. 4.2 that the parameters that determine the configuration and arrangement of the prepared micro-pillars are mainly the pillar spacing S, the pillar height H, and the pillar diameter (cylindrical pillar)/side length (square pillar) D. The configuration parameters of each surface are shown in Table 4.2. At the same time, based on various configuration parameters, the roughness factor on the surface can also be calculated based on Eq. (4.1) and (4.2), and the result is also listed in Table 4.2.

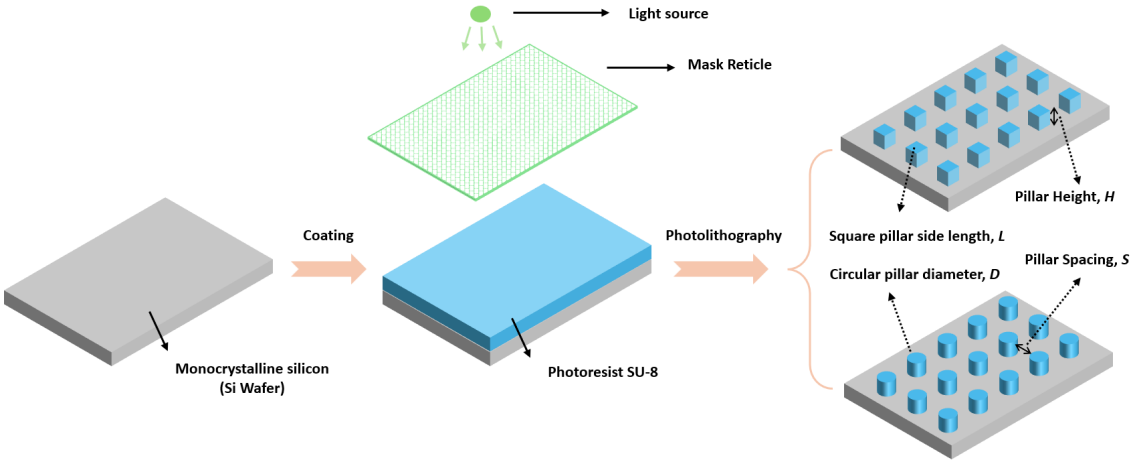


Fig. 4. 2 Photoresist biomimetic surface production process.

Table 4. 2 Biomimetic surface microstructural parameters.

	CS-1	CS-2	CS-3	SS-1	SS-2	SS-3
Average height H (μm)	15	50	30	30	30	40

Diameter/Side Length D (μm)	20	20	30	30	20	20
Spacing S (μm)	15	40	20	20	20	20
Roughness factor (f)	1.769	1.873	2.131	2.44	2.50	3.0

In addition, the experimental equipment and process used to study the evaporation of sessile droplets are the same as those shown in Fig. 3.2. The heating device at the bottom controls the bottom surface temperature between 50 and 80°C. During the evaporation process of the droplet, the droplet profile, such as the change in its contact angle and height, is measured in real time. At the same time, during the evaporation process, the temperature distribution at the droplet liquid-vapour interface is also recorded by the IR Camera (FLIR LLC, USA). At the same time, as the bottom temperature changes, the temperature of the droplet will also change, and its thermophysical properties will also change. The changes in the thermophysical parameters of deionised (DI) water under different temperature conditions are shown in Table 4.3. In addition, there are different calculation methods for the roughness factor for square and cylindrical pillars. When the surface microstructure is a square pillar, the roughness factor can be calculated by Eq. (1):

$$f = \frac{(S + L)^2 + 4 \cdot L \cdot H}{(S + L)^2} \tag{4.1}$$

Besides, when the surface microstructure is a cylindrical pillar, the roughness factor can be calculated by Eq. (2):

$$f = \frac{(S + D)^2 + \pi \cdot D \cdot H}{(S + D)^2} \tag{4.2}$$

At the same time, the Wenzel model could be expressed as:

$$\cos\theta^* = r \cdot \cos\theta \quad (4.3)$$

where θ* is the measured contact angle, θ is the contact angle with a smooth surface, and r is the surface roughness,

Besides, the Cassie–Baxter equation could be expressed as:

$$\cos\theta^* = r \cdot f_{SL} \cdot \cos\theta + f_{SL} - 1 \quad (4.4)$$

where the f_{SL} is the proportion of the actual wetted surface.

Table 4. 3 Physical properties of deionized water at different temperatures

	50°C	**60°C**	**70°C**	**80°C**
Density (g/cm^3)	0.98804	0.98321	0.97778	0.97180
Viscosity (mPa·s)	0.5494	0.4688	0.4061	0.3635
Surface Tension (dyn/cm)	67.91	66.18	64.42	62.61
Thermal Conductivity **(**mW/m·K**)**	640.60	650.91	659.69	667.02

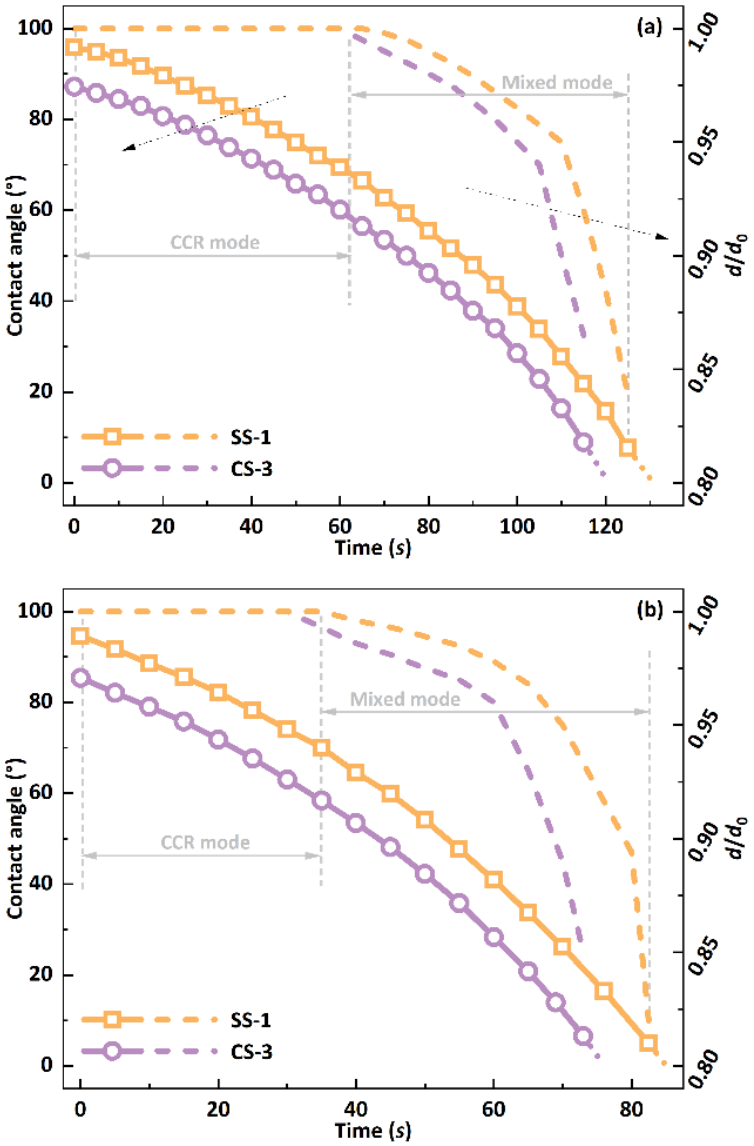
4.3 Results and discussion

4.3.1 Effect of microstructure configuration on droplet wetting performance

This study first investigated the effect of micro-pillar shape on the performance of biomimetic functional surfaces. First, two surfaces, SS-1 and CS-3, were selected, whose surface microstructures have similar dimensions (pillar height: 25 μm; pillar spacing: 20 μm; pillar side length/diameter: 30 μm). During the evaporation of a 1.0 μL DI water droplet on the surface, the changes in the contact angle and dimensionless contact diameter of the droplet are shown in Fig. 4.3, where d_0 is the initial contact

diameter, and d is the real-time contact diameter during the evaporation process. It is worth noting that in actual experiments, the size of the contact angle is not constant and has a dynamic fluctuation range during repeated experiments. The size of the contact angle in this study is the average size after multiple tests. At the same time, since the droplet contact line cannot always remain in a perfect circle during the droplet's evaporation process, the measured contact line length also fluctuates. Still, in this study, it is uniformly considered to be of constant shape to simplify the calculation. When the substrate temperature is 50 °C, the evaporation process of the droplet is shown in Fig. 4.3 (a). The contact angle of the droplet on the SS-1 surface is more significant than that of the droplet on the CS-3 surface, with a difference of about 10%. It is also worth noting that the contact angle on the SS-1 surface is greater than 90°, which is hydrophobic, while the contact angle on the CS-3 surface is less than 90°, which is hydrophilic. As evaporation proceeds, the contact angle gradually decreases. At the end of evaporation, since the measurement of the contact angle of the droplet becomes difficult, the change in the contact angle of the droplet is represented by a dotted line. Therefore, in this chapter, since the last stage of evaporation occupies a very short period of the entire process and has a minimal impact on the overall process, it is ignored to simplify the calculation and analysis. At the same time, the contact line remains fixed on the SS-1 or CS-3 surface in the early stage of droplet evaporation. Still, as the evaporation proceeds, the contact line of the droplet begins to shrink, and the contact diameter decreases by about 15%. Therefore, the droplet experiences two evaporation modes on the biomimetic surface: constant contact radius (CCR) mode and Mixed mode. The CCR mode refers to the contact radius remaining unchanged. In contrast, the contact angle decreases during evaporation, while the Mixed mode refers

to the contact radius and contact angle decreasing simultaneously. In addition, when the substrate temperature increases from 50°C to 60°C, 70°C, and 80°C, the change process of the droplet is shown in Fig. 4.3 (b), (c), and (d), respectively. The total evaporation life of the droplets decreases with the increase in temperature, and the evaporation mode of the droplets still maintains the two modes of CCR and Mixed.



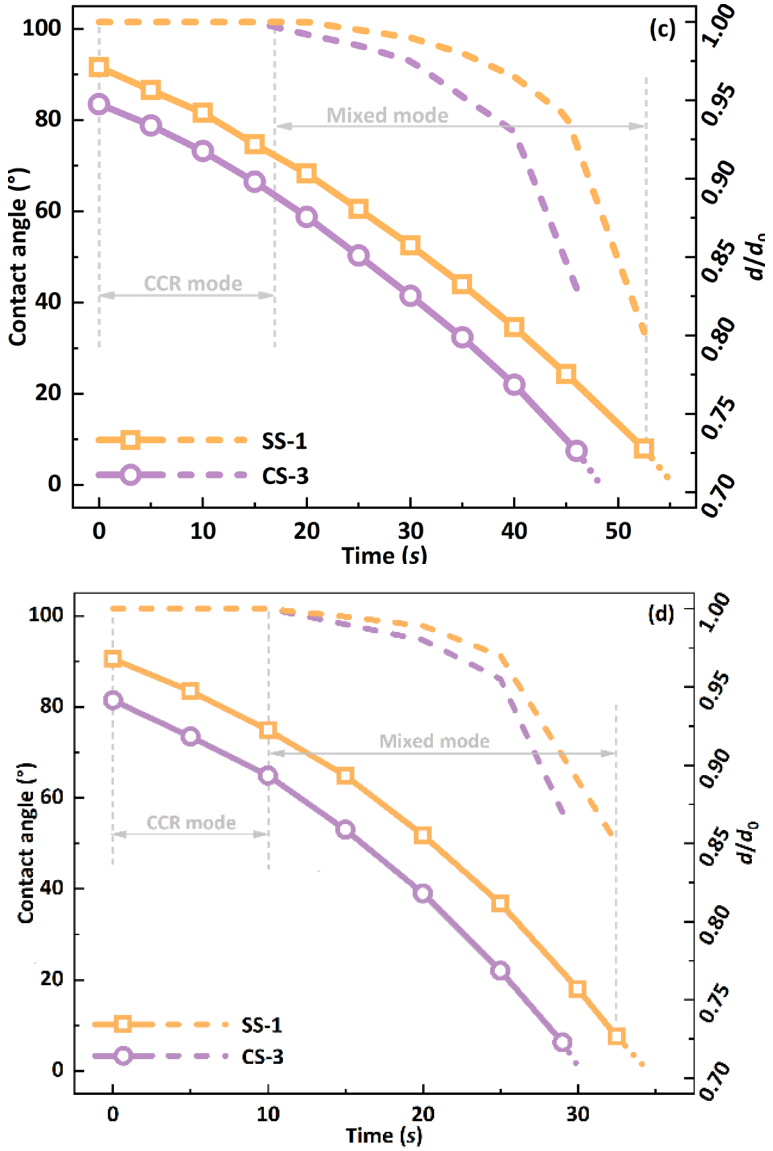
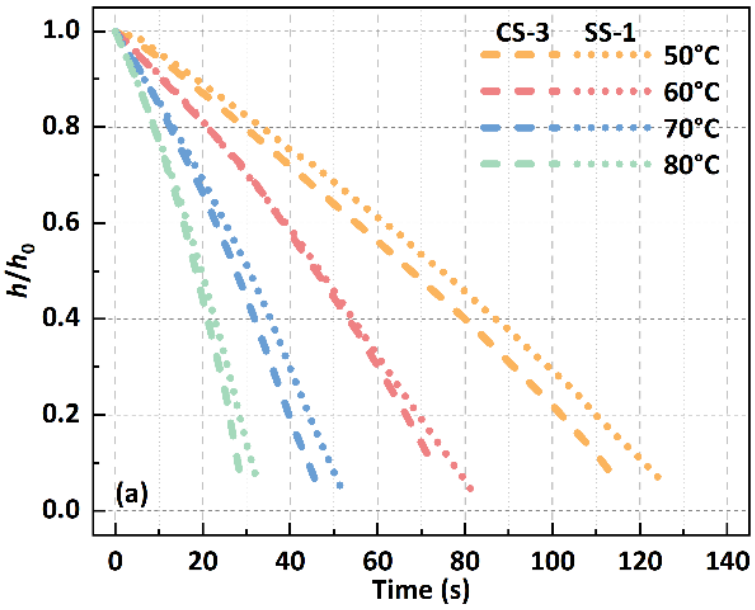


Fig. 4. 3 Changes of contact angle and contact line of a 1.0 μL droplet on SS-1 and CS-3 surfaces at a substrate temperature of (a) 50°C; (b) 60°C; (c) 70°C; (d) 80°C.

At the same time, the changes in the dimensionless height of the droplet on CS-3 and SS-1 under different substrate temperature conditions are shown in Fig. 4.4 (a), where h_0 is the initial height of the droplet and h is the real-time height of the droplet during the evaporation process. With the increase in temperature, the rate of change of droplet height gradually increases, increasing by about four times from 50°C to 80°C, which is caused by the significant acceleration of the evaporation rate. At the same time, the

height reduction rate of the droplet on the CS-3 surface is always slightly higher than that on the SS-1 surface, which is due to the stronger wettability of the CS-3 surface. In addition, the changes in the droplet's initial equilibrium contact angle (ECA) under different surface and substrate temperatures are shown in Fig. 4.4 (b). Both on the CS-3 and SS-1 surfaces, the contact angle of the DI water droplet decreases with the increase of the substrate temperature, and the average decrease rate is -0.19°/℃ and -0.18°/℃, respectively. In addition, the droplets on the CS-3 surface are always in a hydrophilic state (ECA < 90°), while the droplets on the SS-1 surface are basically in a hydrophobic state (ECA > 90°). This phenomenon can be attributed to the fact that the droplets on the CS-3 surface are in the Wenzel state, while the droplets on the SS-1 surface are in the Cassie-Baxter state.



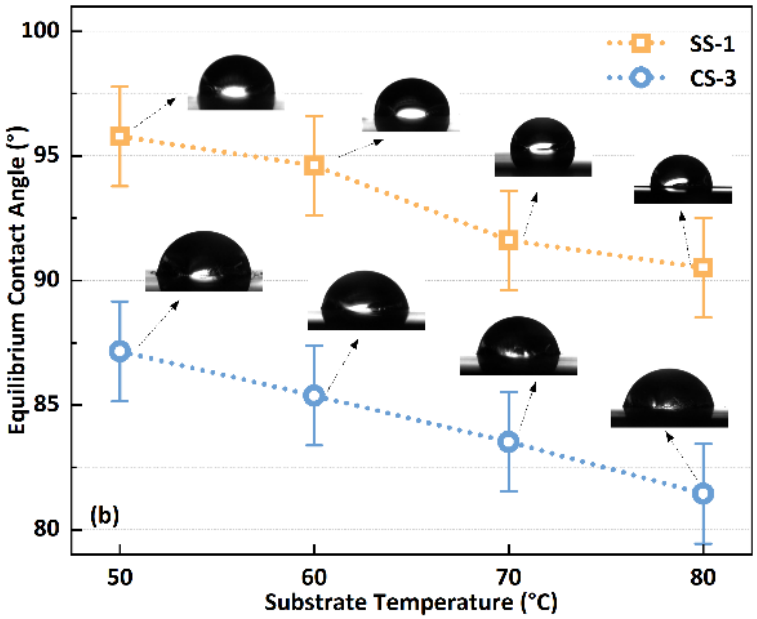
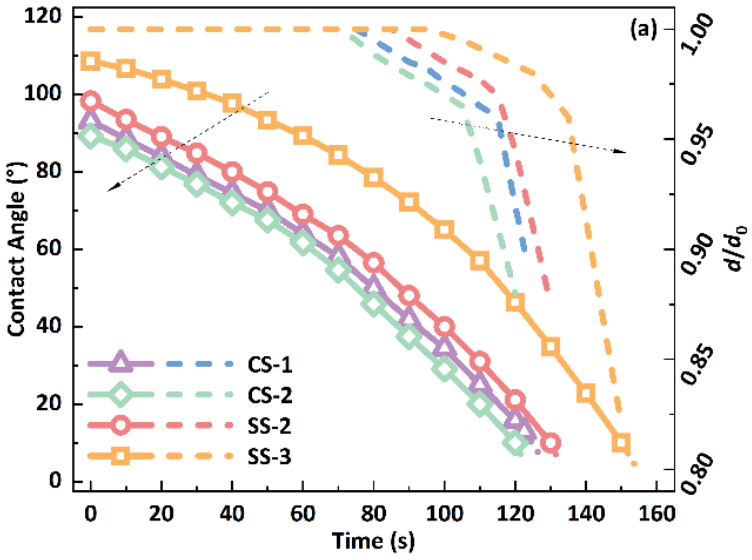


Fig. 4. 4 (a) Dimensionless height of a 1.0 μL droplet over time for different surfaces and substrate temperatures; (b) Initial equilibrium contact angle of a 1.0 μL droplet on different surfaces and substrate temperatures.

4.3.2 Effect of microstructure arrangement on biomimetic surface wettability

The previous chapter studied the influence of the shape of the micropillar structure on the wettability of biomimetic surfaces. The previous section studied the effect of the shape of micro-pillar structures on the wettability of biomimetic surfaces. In this section, we will comprehensively explore the effects of the configuration and arrangement of micro-structures on the wettability of biomimetic surfaces. When the substrate temperature is 50°C, 60°C, 70°C, and 80°C, the evaporation process of the droplet on the different surfaces is shown in Fig. 4.5 (a), (b), (c), and (d), respectively. Furthermore, the contact angle of the droplet on the SS surface is always greater than that on the CS series surface, which indicates that the wettability of the CS series surface is always more substantial than that of the SS series surface. In addition, as the evaporation proceeds, the contact angle of the droplet continuously decreases, while the contact line

is in a pinned state in the first half and then shrinks as the evaporation proceeds. Therefore, no matter what surface, the droplet evaporation process will transition from CCR to Mixed mode. In addition, it can be seen from Fig. 4.5 (b-d) that when the substrate temperature increases, its evaporation process does not change significantly except that the lifetime is significantly reduced. The evaporation mode of the droplet still undergoes a transition from CCR to Mixed mode. The wettability of the CS series surface is always more substantial than that of the SS series surface. Besides, it can also be found that the SS series surfaces maintain the droplet pinning state for a longer time, contributing to its ability to produce a hydrophobic state.



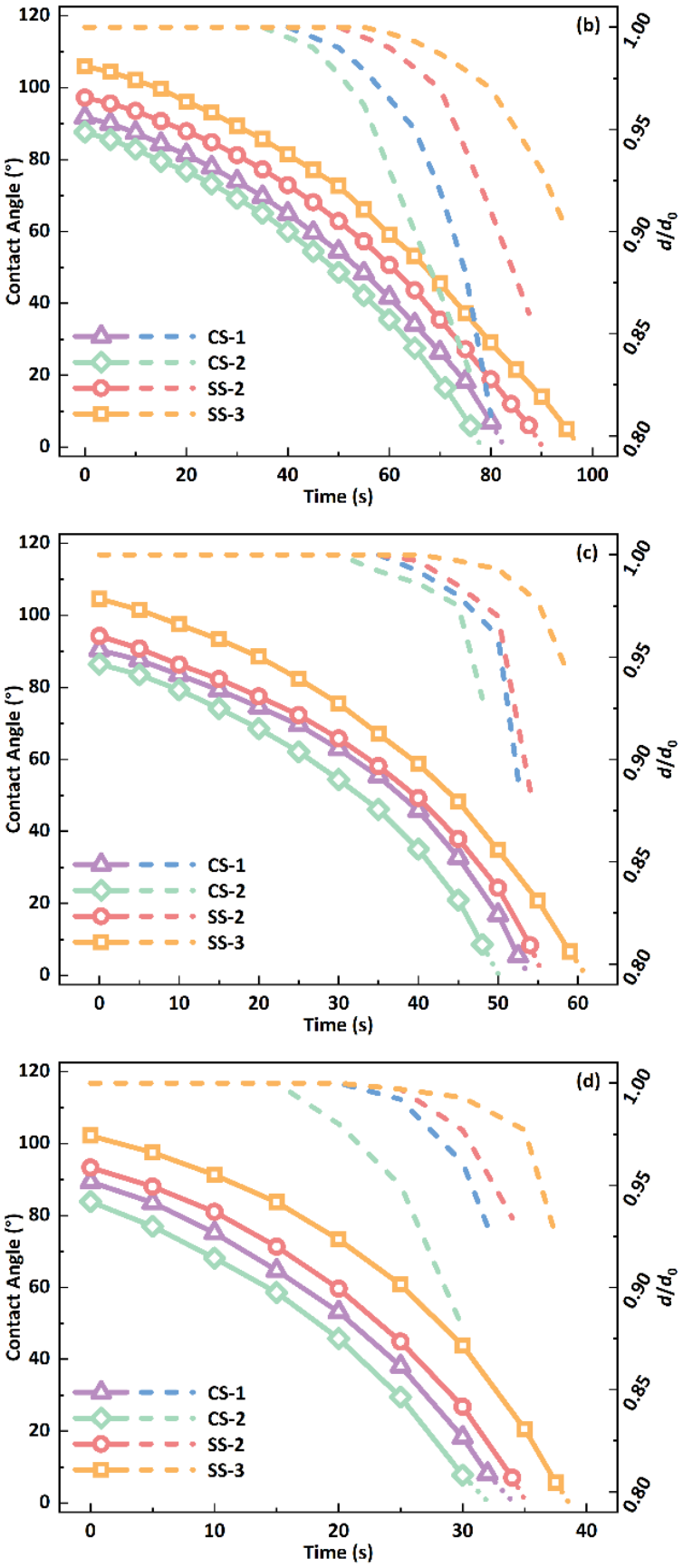


Fig. 4. 5 Changes of contact angle and contact line of a 1.0 μL droplet on different surfaces at a

substrate temperature of (a) 50°C; (b) 60°C; (c) 70°C; (d) 80°C.

In summary, the size and arrangement of biomimetic surface microstructures significantly impact wettability. For the overall comparative study, the magnitudes of the initial equilibrium contact angles of the droplets on the CS and SS series surfaces are shown in Fig. 4.6 (a). The ECA of the droplets on the SS series surface is greater than 90°, and they are all hydrophobic. However, the ECA of the droplets on the CS-1 surface is greater than 90° at low temperatures (T_{sub}<70°C), and the ECA gradually decreases and is less than 90° as the temperature rises to 80°C. This phenomenon can be attributed to the change of the droplet contact angle from the Cassie–Baxter state to the Wenzel state. Besides, on the CS-2 and CS-3 surfaces, the ECA of the droplets was consistently below 90°, indicating their hydrophilicity. Moreover, SS series surfaces can increase the contact angle by about 12% on average compared with CS series surfaces. This could be attributed to the square pillar microstructure having denser gaps, making it easier for droplets to be in the Cassie–Baxter wetting state. At the same time, on any surface, the ECA of DI water droplets decreases with increasing temperature, and the average decrease rate is about 0.17°/°C. At the same time, under different substrate temperatures and surfaces, the changes in the work of adhesion (WoA) between the solid-liquid interface at the initial equilibrium state of the droplet are shown in Fig. 4.6 (b). The work of adhesion on the CS series surface is always greater than that on the SS surface, with the maximum difference reaching up to 36%. This means that more work is required to separate the droplet on the CS series surface or that more energy is released during the wetting process of the droplet on the CS series surface.

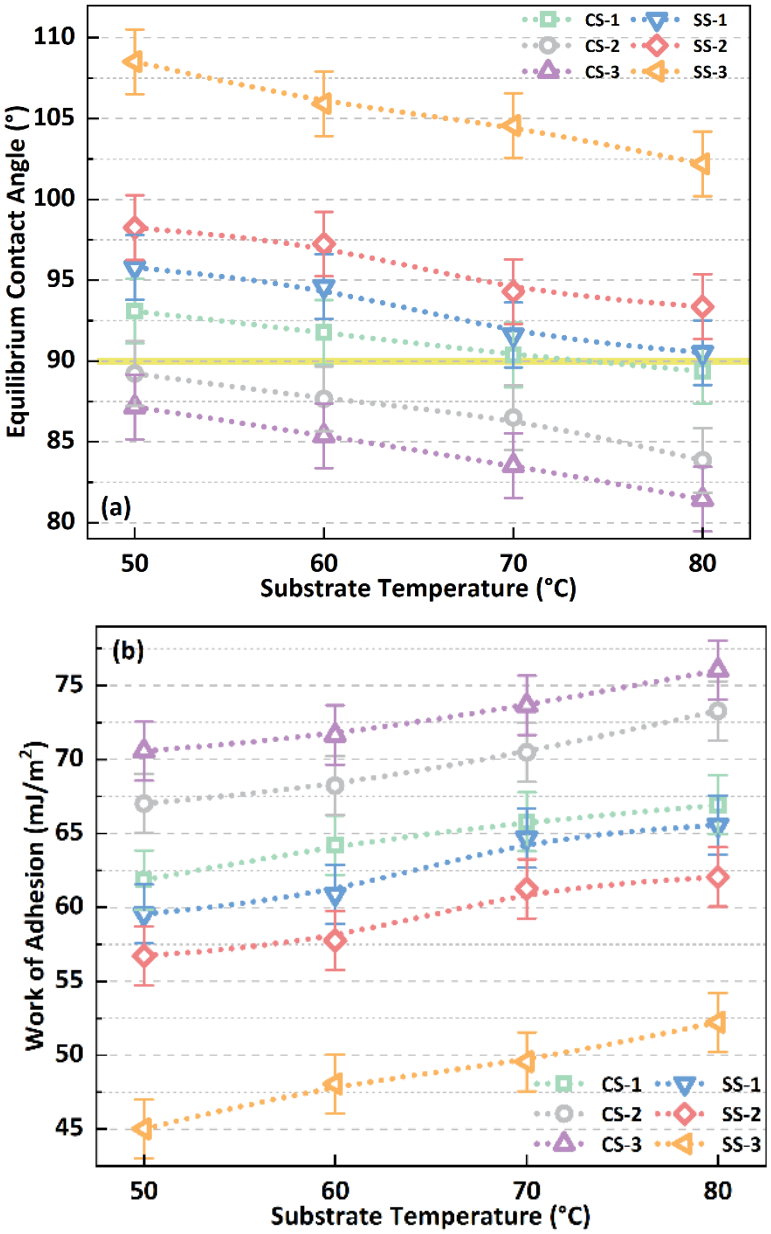


Fig. 4. 6 (a) The initial equilibrium contact angle of the droplet changes under different surface and substrate temperature conditions; (b) The initial adhesion work of the droplet changes under different surface and substrate temperature conditions.

4.3.3 Effect of microstructure arrangement on interfacial heat transfer

In addition to the wetting characteristics, the research will continue exploring the influence of biomimetic functional surface microstructure on the sessile droplet

interfacial heat transfer characteristics. Taking the CS-3 and SS-3 surfaces as examples, when the substrate temperature is 50 °C and 80 °C, the temperature distribution changes at the droplet liquid-vapour interface are shown in Fig. 4.7 (a) and (b), respectively. It can be seen intuitively that no matter the substrate temperature increases from 50 °C to 80 °C, the temperature distribution of the liquid-vapour interface of the droplet on the CS-3 surface will be more uniform in each period. Besides, as the evaporation process proceeds, the temperature of the droplet liquid-vapour interface gradually increases. These phenomena can be mainly attributed to the fact that as evaporation proceeds, the height of the droplets gradually decreases, which enhances the heat transfer inside the droplets and thus gradually increases the temperature of the liquid-vapour interface.

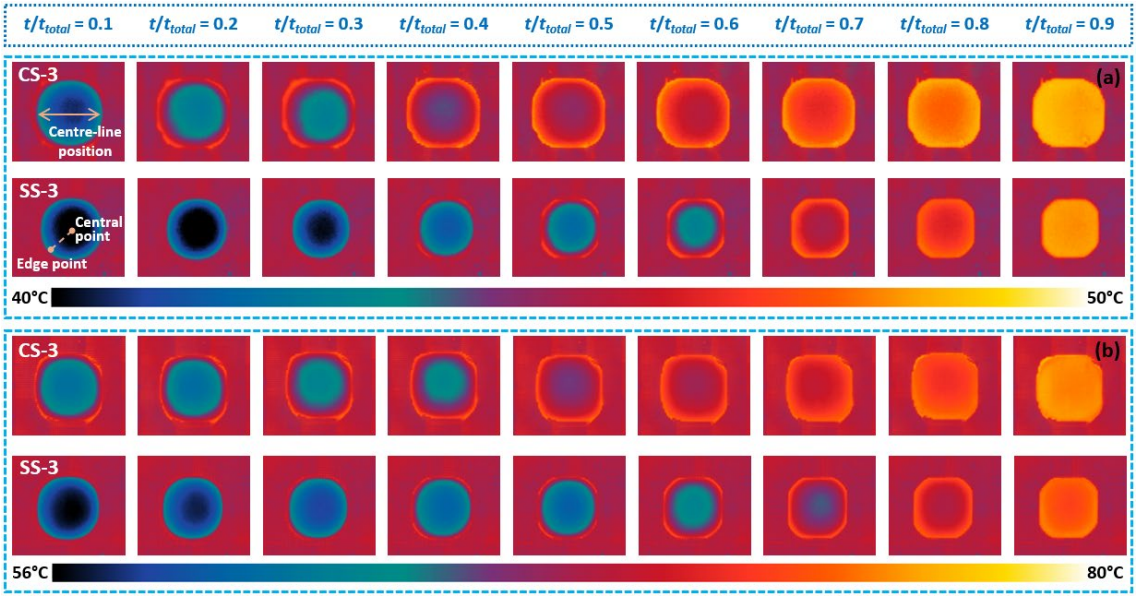
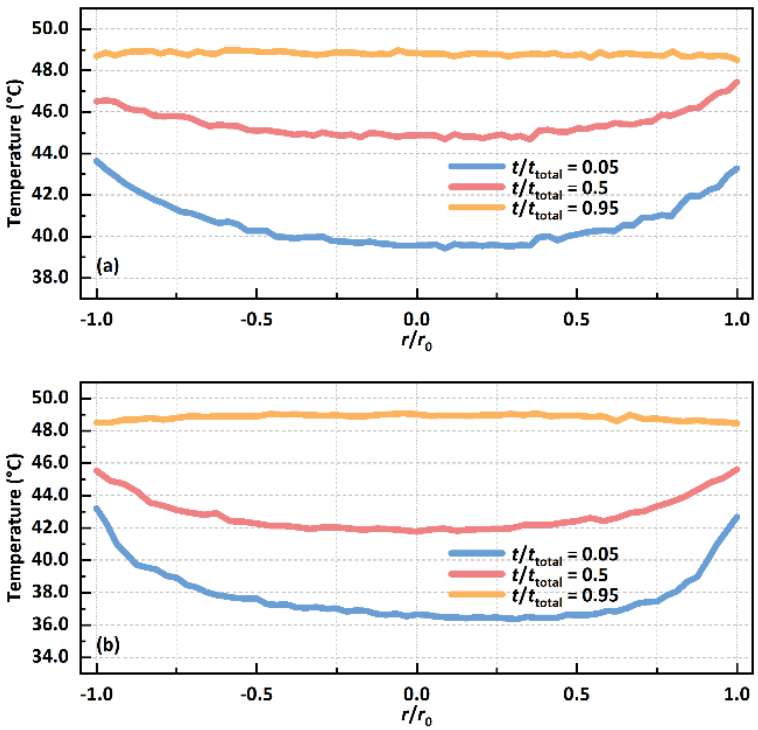
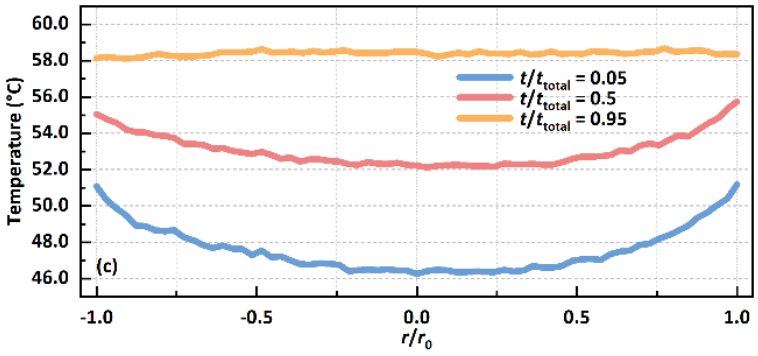


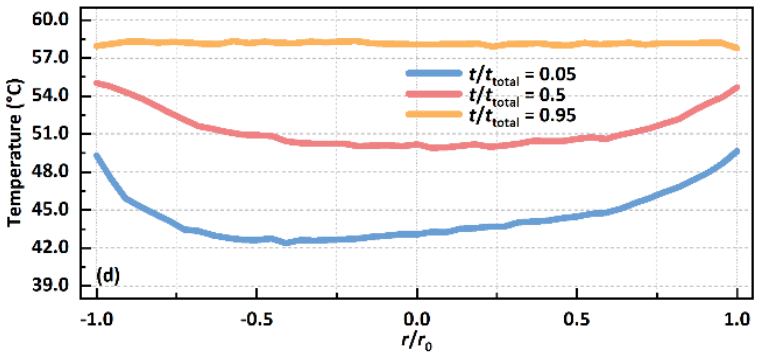
Fig. 4. 7 Temperature distribution of the droplet liquid-vapour interface on the CS-3 and SS-3 surfaces at different periods when the substrate temperature is (a) 50 °C and (b) 80 °C.

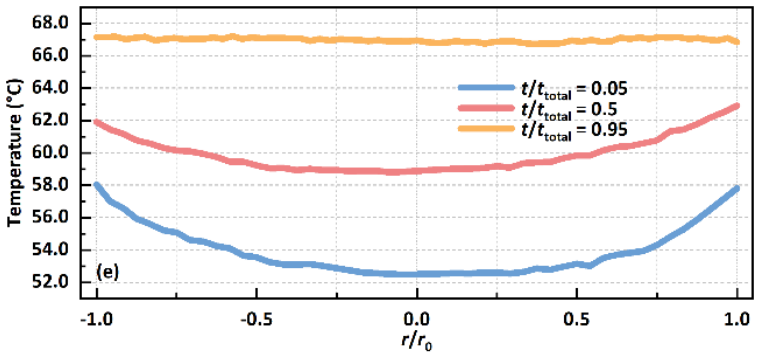
In addition, it can be seen from Fig. 4.7 that the temperature distribution of the liquid-vapour interface of the droplets on the SS-3 surface is more uneven at almost every stage of droplet evaporation. At the same time, the temperature distribution at the

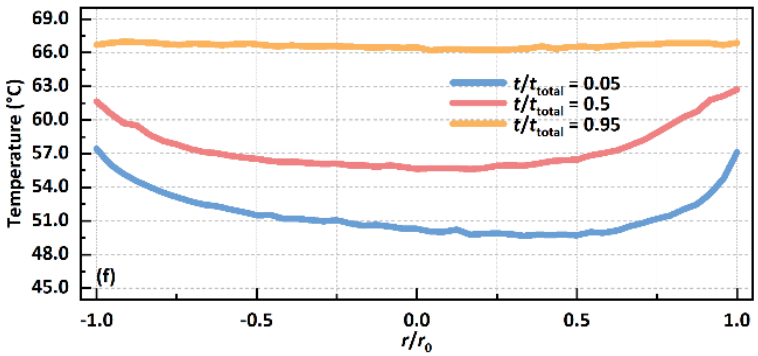
central line position of the droplet at the beginning, middle, and end of evaporation under the substrate temperature range from 50 to 80 °C is shown in Fig. 4.8. Among them, when the droplet is located on the CS-3 surface when the substrate temperature increases from 50°C to 80°C, the temperature distribution is shown in Fig. 4.8 (a), (c), (e), and (g), respectively. As the temperature increases, the temperature non-uniformity of the droplets in the initial stage also increases, up to 37%, and tends to be uniform in the final stage. This phenomenon also occurs on the SS-3 surface, as shown in Fig. 4.8 (b), (d), (f), and (h). In addition, by comparison, it can be found that under the same substrate temperature conditions, the temperature distribution of the droplet liquid-vapour interface on the SS-3 surface is more uneven, which could be attributed to the hydrophobicity of the SS series surface.




Temperature (°C)
60.0
58.0
56.0
54.0
52.0
50.0
48.0
46.0
(c)
-1.0
-0.5
0.0
0.5
1.0
r/r0
t/ttotal = 0.05
t/ttotal = 0.5
t/ttotal = 0.95


Temperature (°C)
60.0
57.0
54.0
51.0
48.0
45.0
42.0
39.0
(d)
-1.0
-0.5
0.0
0.5
1.0
r/r0
t/ttotal = 0.05
t/ttotal = 0.5
t/ttotal = 0.95


Temperature (°C)
68.0
66.0
64.0
62.0
60.0
58.0
56.0
54.0
52.0
(e)
-1.0
-0.5
0.0
0.5
1.0
r/r0
t/ttotal = 0.05
t/ttotal = 0.5
t/ttotal = 0.95


Temperature (°C)
69.0
66.0
63.0
60.0
57.0
54.0
51.0
48.0
45.0
(f)
-1.0
-0.5
0.0
0.5
1.0
r/r0
t/ttotal = 0.05
t/ttotal = 0.5
t/ttotal = 0.95

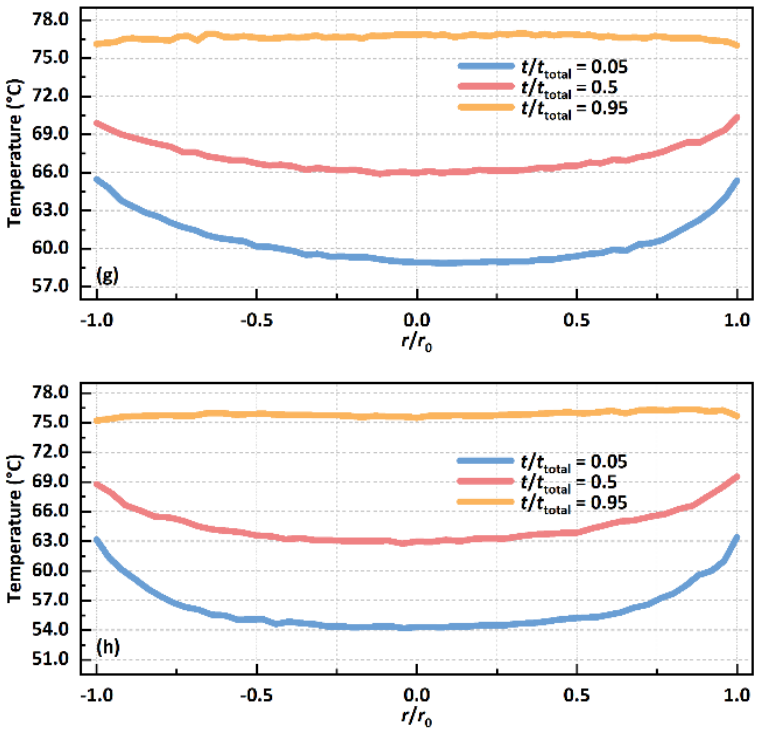
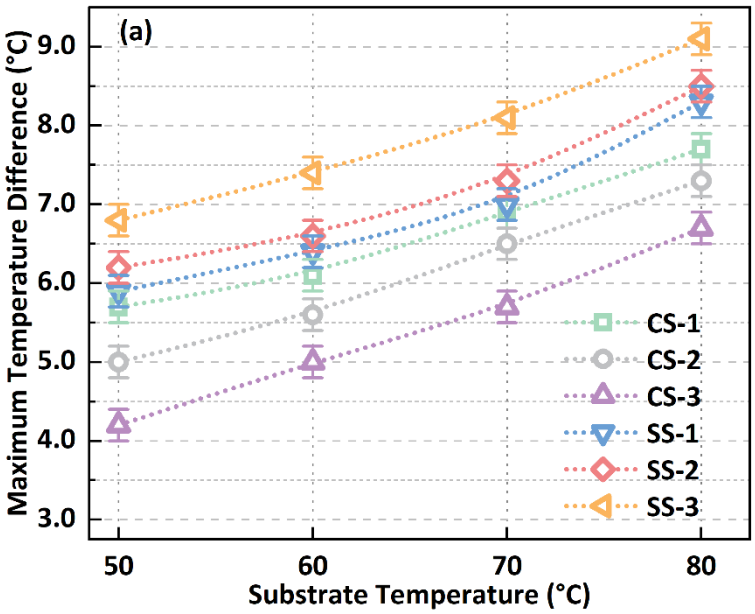


Fig. 4. 8 When the substrate temperature of the CS-3 surface is (a) 50°C, (c) 60°C, (e) 70°C, (g) 80°C, the temperature distribution at the centre-line of the droplet liquid-vapour interface at different periods; when the substrate temperature of the SS-3 surface

In addition, the droplet liquid-vapour interface maximum temperature difference ($T_{diff, max}$) under various surface and substrate temperature conditions is shown in Fig. 4.9 (a). The maximum temperature difference refers to the temperature difference between the centre of the droplet liquid-vapour interface and the contact line, such as the mark in Fig. 4.7. On any surface, the maximum temperature difference of the droplets always increases with increasing substrate temperature, up to a difference of 37%. At the same time, when the substrate temperature increases, the gap of the maximum temperature difference between different surfaces remains unchanged basically, such as the maximum temperature difference between the SS-3 and CS-3 surfaces kept at 2.5°C when the substrate temperature rises from 50°C to 80°C. At the same time, when the substrate temperature is 50°C -80°C, the CS surface can reduce the maximum

temperature difference by about 18% compared with the SS surface. These phenomena indicate that as the substrate temperature or hydrophobicity increases, the evaporative cooling effect at the droplet liquid-vapour interface will be enhanced. Besides, the changing trends of the average evaporation rate of droplets on various surfaces under different substrate temperature conditions are also shown in Fig. 4.9 (b). As the temperature increases, the evaporation rate of the droplets increases significantly, increasing by about 4 times on average from 50°C to 80°C. Besides, the evaporation rate of the droplets on the SS series surface is always lower than that on the CS series surface, with an average decrease of about 13%, which can be attributed to the dual effects of decreased internal heat transfer of the droplets and enhanced interfacial evaporative cooling effect.



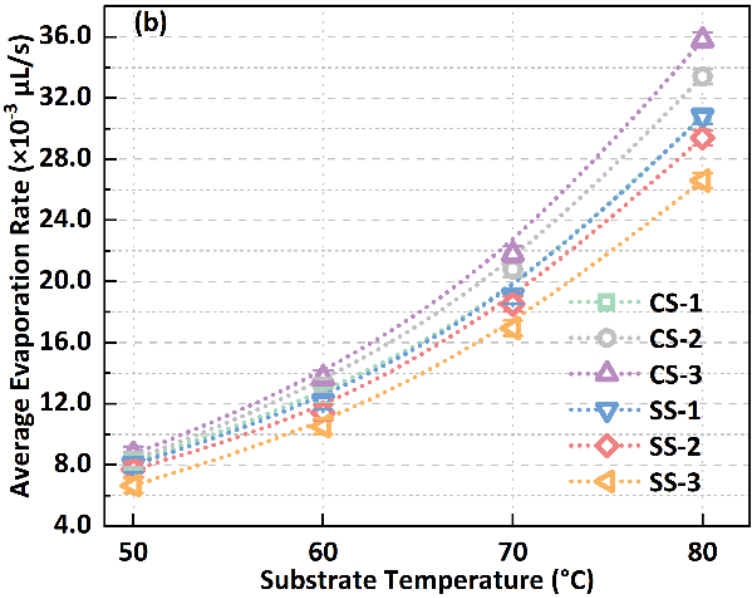


Fig. 4. 9 (a) Temperature difference at the droplet liquid-vapour interface in the initial state under different surface and substrate temperature conditions; (b) Variation of the overall average evaporation rate of the droplet with the surface and substrate temp

4.4 Chapter summary

Inspired by natural bionics, this study designed the bionic functional surface with the micro-pillar structure through photolithography technology. Based on this, the effects of the microstructure structural parameters and arrangement on the biomimetic surface wettability and the heat and mass transfer process at the liquid-vapour interface of the sessile droplets were further studied. The research results show that square micropillars have denser voids under the same or similar size and arrangement conditions, achieving a more significant roughness factor, which may help achieve the hydrophobic state. In addition, the substrate temperature will also affect the wettability. As the temperature increases, the contact angle of the droplets on any surface will decrease, enhancing the biomimetic surface wettability. In addition, the microstructure of the biomimetic

surface also significantly impacts the heat and mass transfer process at the liquid-vapour interface of the sessile droplets. Studies have shown that compared with the CS series surfaces, the liquid-vapour interface of the droplets on the SS series surfaces has a more uneven temperature distribution, with an average difference of up to 18%. This can be attributed to the fact that the SS series surface not only increases the thermal resistance inside the droplet but also causes a more obvious evaporative cooling effect at the liquid-vapour interface. Naturally, under the combined effect of these factors, the evaporation rate of droplets on the SS series surface is suppressed, and the reduction can reach 13% compared with the CS series surface. This study hopes to contribute to applying and researching biomimetic functional surfaces, especially those prepared based on photoresist lithography technology.

Chapter 5. Effect of surface roughness on silica nanoparticle-laden droplet evaporation dynamics

This chapter focuses on the influence of copper surface roughness on the evaporation dynamics and deposition mode of fixed silica nanofluid droplets. Copper is selected as the droplet-bearing surface in this section because of its wide application in thermal management and even industrial manufacturing. This experimental study reveals the critical influence of the roughness of copper, a widely used heat dissipation material, on the heat and mass transfer process and sedimentary pattern of silica nanofluid droplet evaporation.

5.1 Chapter introduction

As mentioned above, droplet evaporation is one of nature's most common physical processes. Among them, due to nanofluid efficient energy transport characteristics, the evaporation of nanofluid droplets has received widespread attention and has been widely used in various fields [177, 237-239]. Therefore, it is natural to associate that in addition to nanofluidic properties, the characteristics of the surfaces contacted by the droplets will strongly influence their evaporation and deposition processes. Hence, as one of the primary surface properties, surface roughness has been widely considered in engineering and scientific research [240], and surface roughness will significantly impact the heat dissipation effect of thermal management methods based on droplet evaporation, such as spray cooling. Therefore, it is crucial to reveal the impact of surface roughness on the nanofluid droplet evaporation dynamics and sedimentary pattern. However, studies about the influence of surface roughness on the sessile

nanofluid droplet evaporation process are not much, and the mechanism of the effect of surface roughness on the evaporation heat transfer of nanofluid droplets still needs more research. Not many reports have clarified the relationship between the surface roughness and the nanofluid droplet sedimentary pattern until now. Therefore, the study in this chapter helps reveal the interaction mechanism between surface roughness, nanofluid droplet evaporation dynamics, and sedimentary process, which is expected to guide related industrial applications and scientific analysis.

5.2 Experimental setups and methodology

Before the experiment, the environmental conditions of the closed laboratory were measured. The relative humidity in the laboratory was about 50 ± 5%, which was detected automatically; the ambient temperature and air pressure were 293 ± 2 K and 0.1 MPa, respectively. Under these well-controlled conditions, the experimental measurements are highly reproducible. The experimental processes are shown in Fig. 3.2. The characterisation of the surface roughness of the S1 to S4 surfaces is shown in Fig. 5.1.

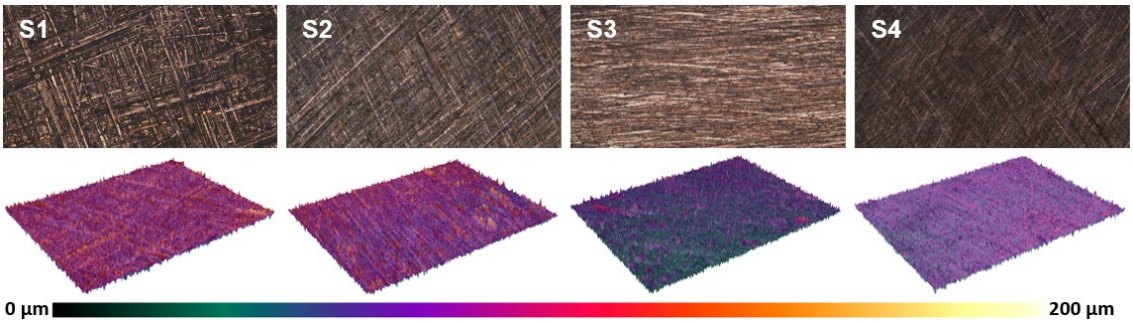


Fig. 5. 1 The optical profiling of the sample surface.

The fluids used in the experiments are deionised (DI) water and silica nanofluid, in

which silica nanoparticles (SNP) were dispersed in DI water (RS PRO, UK) and followed by ultrasonication for two hours based on the two-step method. The silica nanoparticles (Sigma-Aldrich, USA) with a diameter of 0.007 μm were used in this study and were prepared at a fixed particle concentration of 0.5% volume fraction, respectively. A pipette (Eppendorf Corporate, Germany) generates the nanofluid droplet, ensuring a constant volume by smoothly pushing the working fluid out. Meanwhile, 2, 4, 6, and 8 μL are the droplet volumes used during the experiment.

5.2.1 Substrate surface preparation

As shown in Fig. 5.1, the copper discs were polished with emery paper (3M Science, USA) through a lapping machine. The grid size of the emery papers is P120, P240, P400, and P1200, respectively. The optical microscope (OPTIKA Microscopes, Italy) with cold LED light observed the surface image and the deposition appearance. Besides, in this study, the surface roughness parameters of the substrate listed in Table 5.1 and the 3D colour view images shown in Fig. 5.1 were measured by the 3D optical profilometer (KLA Corporation, USA). The surfaces S1 to S4 are fabricated by P120, P240, P400, and P1200 emery paper through a grinding machine. The surface roughness parameters include S_a which means the roughness average, S_q means the root mean square roughness, S_p means the highest peak height, S_v means the absolute value of maximum pit height, and S_{sk} means the surface skewness. The calculation formula is shown in Eq. (5.1-5.5). The copper discs are fixed on the water bath heater with silicone grease (RS PRO, UK), and the surface temperature is controlled at about 40 ± 2 ℃.

Table 5. 1 Surface roughness measurement data of copper disc samples

Samples No.	S_a (μm)	S_q (μm)	S_p (μm)	S_v (μm)	S_{sk} (μm)
S1	15.86	20.64	96.19	84.25	-0.0343
S2	14.88	19.78	90.73	112.32	-0.6768
S3	13.97	18.83	99.02	110.05	-0.6919
S4	9.389	12.05	80.97	51.61	0.2265

$$S_a = \frac{1}{A}\iint_A |z(x,y)|\,dx\,dy \tag{5.1}$$

$$S_q = \sqrt{\frac{1}{A}\iint_A \big(z(x,y)\big)^2\,dx\,dy} \tag{5.2}$$

$$S_p = \max_A z(x,y) \tag{5.3}$$

$$S_v = \left|\min_A z(x,y)\right| \tag{5.4}$$

$$S_{sk} = \frac{1}{{S_q}^3}\left[\frac{1}{A}\iint_A z^3(x,y)\,dx\,dy\right] \tag{5.5}$$

It is essential to determine if the sessile droplet on the rough copper surfaces is a spherical cap to analyse the subsequent changes in the droplet shape. The effect of gravity on the droplet could be confirmed by the Bond number (Bo), a dimensionless number defined as the ratio of gravitational force to surface tension force. And usually, when the Bo is less than 1.0, the effect of the influence of gravity can be ignored, and surface tension dominates. The maximum value of the Bo number in this study is about 0.85, so all experimental groups can be regarded as meeting the requirements. The Bo can be calculated by using Eq. (5.6),

$$Bo = \frac{\Delta\rho r^2 g}{\sigma_{lg}} \quad (5.6)$$

where $\Delta\rho$ is the density difference between the liquid and air, r is the radius of the contact line, g is the gravitational acceleration, and σ_{lg} is the surface tension of the liquid.

5.2.2 Silica nanofluid preparation

In this experimental study, the one-step method was used to prepare nanofluids, a standard method for preparing nanofluids [241-243]. The one-step method usually has the advantages of good dispersion and high suspension stability. In this thesis, the silica nanoparticles were directly dispersed into the base liquid deionized water, and then an ultrasonic generator was used for ultrasonic vibration and stirring for 2 hours. In this experiment, the mass percentage concentration of silica nanofluid was 0.5 wt%. Besides, it needs to be mentioned that based on previous studies on the surface tension of silica nanofluids [244, 245], the surface tension of 0.5 wt% nanofluid at 40°C was estimated to be 63 mN/m.

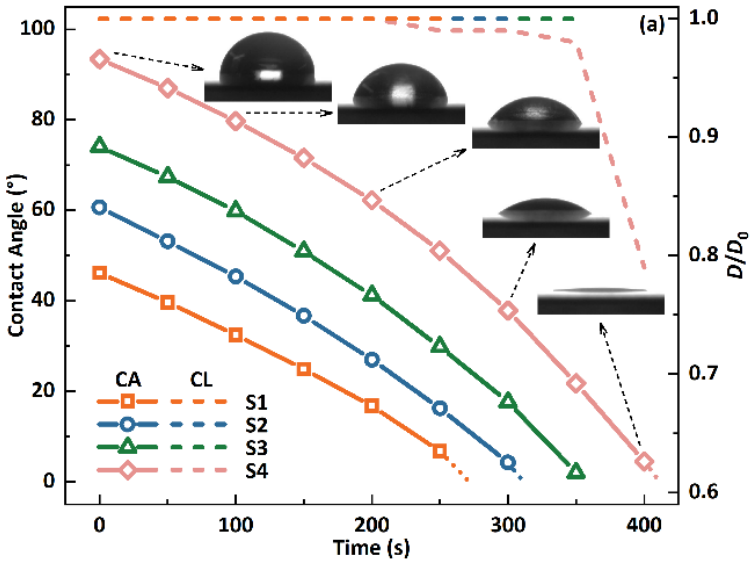
5.3 Results and Discussion

5.3.1 The effect of surface roughness on the droplet wettability

The surface wettability could be influenced significantly by the surface roughness. As seen in Fig. 5.2 (a-d), the surface wettability also improved with the increase of the surface roughness degree. As shown in Fig. 5.2 (a), for the 2 μL silica nanofluid droplet, when it is located on the S1 surface, the contact angle (CA) appears as 43°

approximately. When the surface changes to the S2, S3, and S4, the apparent contact angle also increases to about 60°, 77°, and 92°, respectively. This is attributed to the inverse relationship between contact angle and roughness under hydrophilic surfaces. It also could be described as $\cos\theta^* = r \cdot \cos\theta$, which is also known as the Wenzel equation [64], where θ* is the apparent contact angle, θ refers to Young's contact angle, r refers to surface roughness degree. As shown in Fig. 5.2 (b-d), this phenomenon still occurs when the volume of silica nanofluid droplets increases. Although the initial apparent contact angle changes somewhat with the volume change, the overall difference is insignificant. It can be concluded that the impact of droplet volume on wettability is very limited. In addition, it is worth mentioning that on surfaces with different roughness, the difference in the contact angle hysteresis of the droplet is not apparent, which shows that the surfaces are generally hydrophilic. Then, as shown in Fig. 5.2 (a-d), the surface roughness degree also significantly affects the silica nanofluid droplet evaporation lifetime. It is worth noting that the contact angle is too small in the final evaporation stage, making it difficult to measure directly. Therefore, for the convenience of analysis, the endpoint of the evaporation time of the curve in Fig. 5.2 is taken as an integer multiple of 50s, and the final stage of evaporation is described by a dotted line fitting. As shown in Fig. 5.2 (a), as the substrate surface changes from S1 to S4, the evaporation lifetime extends from about 250 s to 400 s, increasing by about 60%. As shown in Fig. 5.2 (b-d), as the surface roughness degree decreases, the evaporation lifetime of the sessile droplet also maximum prolongs about 66.7%, 71.4%, and 75%, respectively. It can be concluded that on a hydrophilic surface, the increase in roughness will reduce the life of the silica nanofluid droplet, which may owe to the increase in roughness increases the contact area of the solid-liquid interface, enhances the heat

transfer process, and promotes evaporation. Besides, the wettability can significantly affect the evaporation mode of droplets [246]. Similarly, in this study, the surface roughness could also significantly affect the silica nanofluid evaporation mode. As shown in the dotted line in Fig. 5.2 (a-d), regardless of the droplet volume, the evaporation mode of the droplets on the S1, S2, and S3 surfaces always remains in the constant contact radius (CCR) mode [247], which means that the droplet contact line (CL) is pinned. The contact angle continues to decrease during the evaporation process. However, on the S4 surface, during the last 10%-20% stage of evaporation of the droplet, the evaporation mode of the droplet will change from CCR to mixed mode [63], which refers to the process that the contact line and contact angle of the droplet move simultaneously. It may be because smoother surfaces have more minor energy barriers, lowering the energy and tension requirements needed to move the droplet contact line. Thus, as evaporation proceeds, the surface tension at the liquid-vapour interface drives the contraction of the contact line, which in turn gives rise to the slip phenomenon.



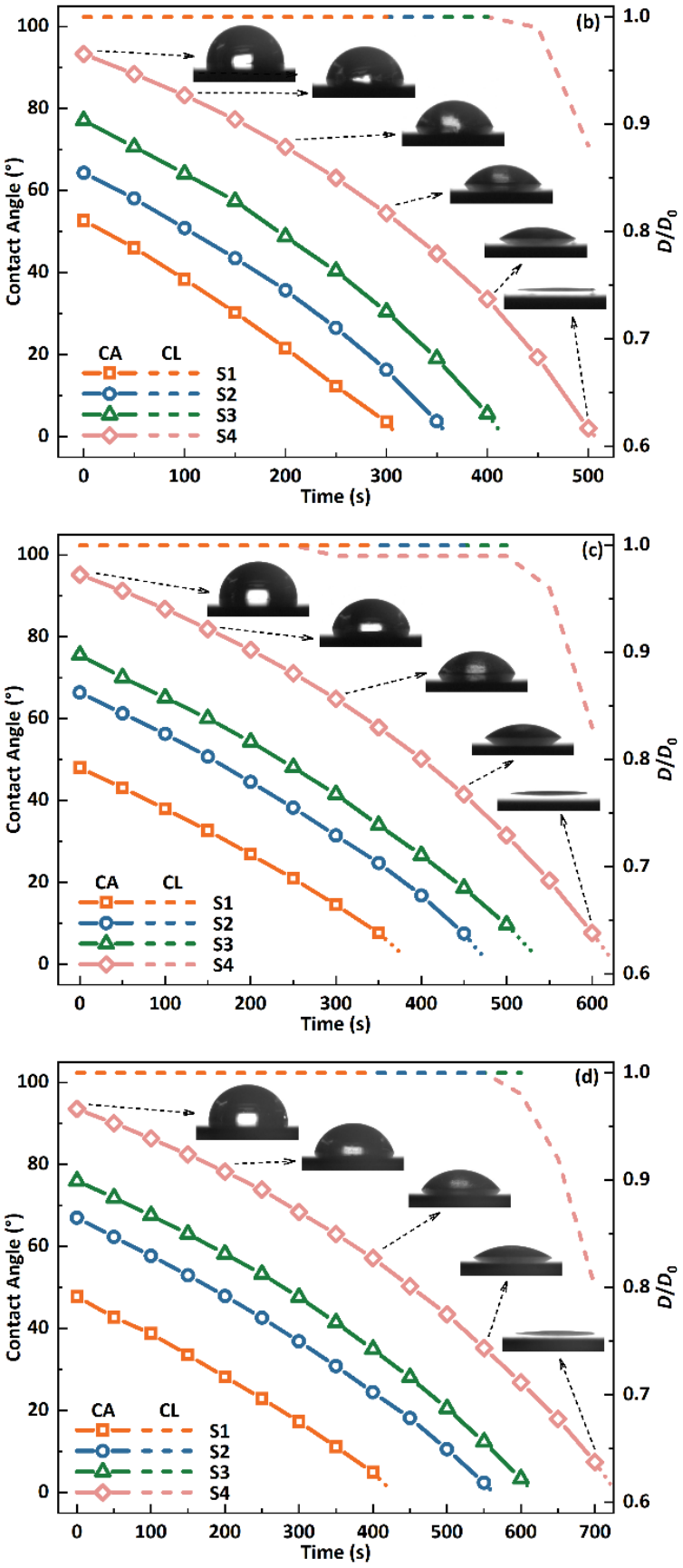
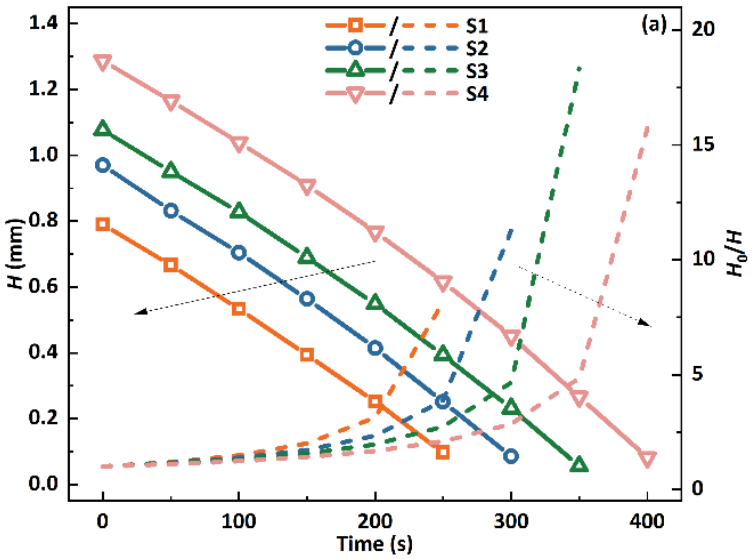


Fig. 5. 2 Evolution of the contact angle of a sessile droplet with a volume of (a) 2, (b) 4, (c) 6, (d) 8 µL

when located on substrates with different roughness.

At the same time, the quantitative trend of droplet height H changes is shown in Fig. 5.3 (a-d). The degree of surface roughness has a significant effect on profile-changing trends. As shown in Fig. 5.3 (a), with the increase of the surface roughness degree, the height of the silica nanofluid also keeps decreasing. Then, the inverse ratio of dimensionless height change with time is also shown in Fig. 5.3 (a). Regardless of the surface roughness, the rate of change of the reciprocal of the dimensionless height of the droplet (H_0/H) increases significantly as the evaporation process proceeds, and they all rise sharply about fifty seconds before the evaporation process ends. As shown in Fig. 5.3 (b-d), this trend also has the same appearance at the droplet volume of 4-8 μL. This may be because, during the evaporation process, the height of the droplets decreases. In the final evaporation stage, the evaporative cooling effect is weakened. This makes the relative evaporation rate of the droplets more significant, which in turn accelerates the droplet height shrinking velocity.



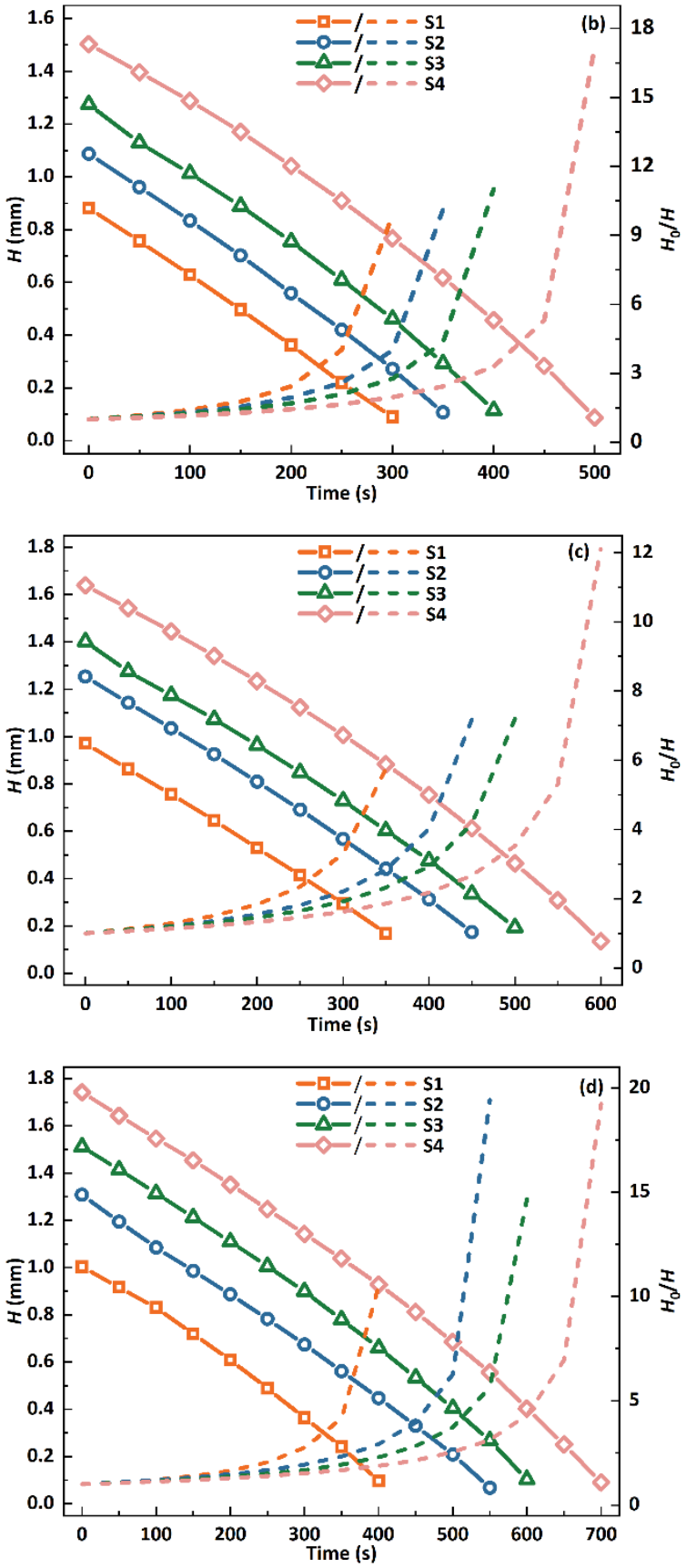
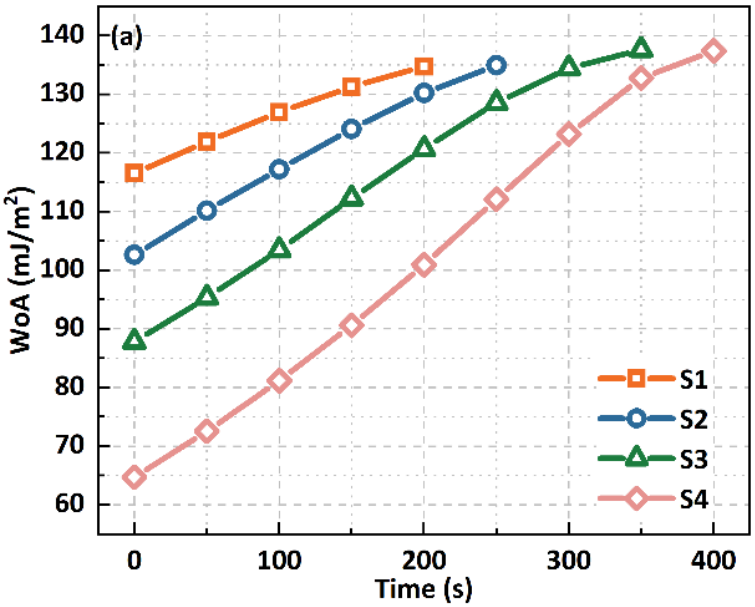
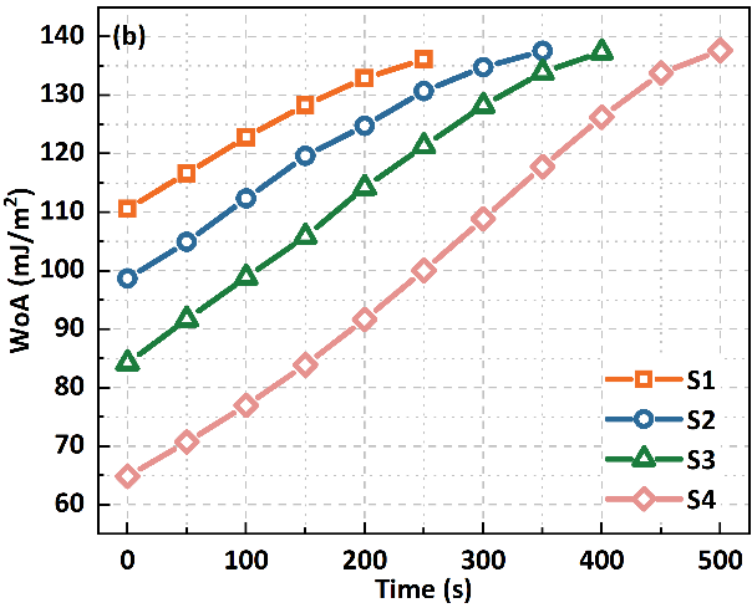
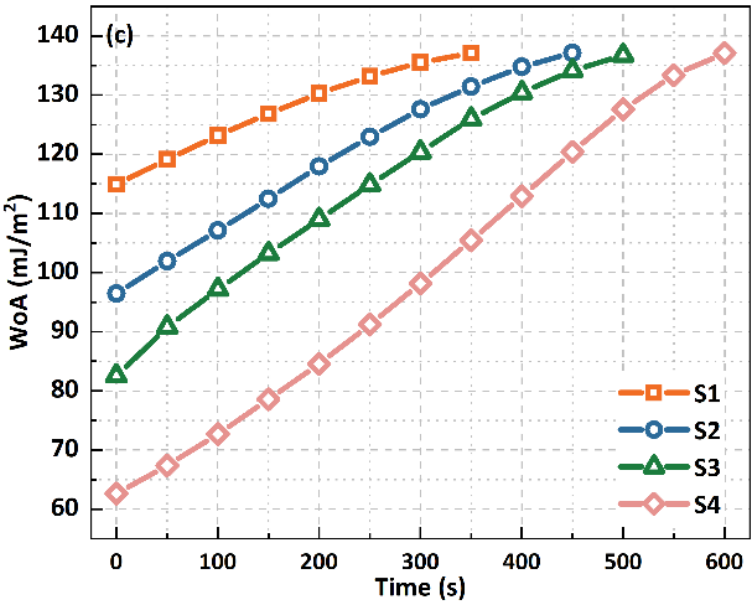


Fig. 5. 3 The height shrinkage process of the (a) 2 μL, (b) 4 μL, (c) 6 μL, and (d) 8 μL droplets.

To further study the effect of copper surfaces with different roughness on the wettability of silica nanofluid droplets, based on the experimental results, the change of the work of adhesion (WoA) at the liquid-solid interface of the droplet during the evaporation process was calculated according to Eq. (5.7-5.9), as shown in Fig. 5.4 (a-d). As the surface roughness decreases, the work of adhesion between the droplet solid-liquid interface also decreases. Based on the individual volumes, the initial work of adhesion of the silica nanofluid droplet decreases by an average of about 45% when the surface goes from S1 to S4. During the evaporation of the droplet, the magnitude of the adsorption work at the liquid-solid interface of the droplet on the surface with minor roughness is always lower. As time goes by, the work of adhesion of the liquid-solid interface gradually increases and eventually reaches a maximum value of about 137 mJ/m^2. These calculations show that the greater the roughness, the more work is required to separate the droplet from the surface and the stronger the wetting ability.




(b)
WoA (mJ/m²)
Time (s)
S1
S2
S3
S4


(c)
WoA (mJ/m²)
Time (s)
S1
S2
S3
S4

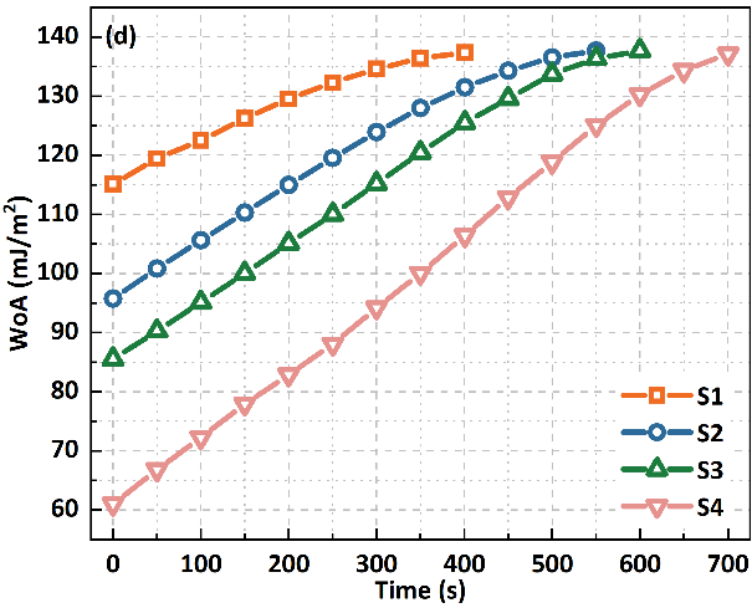
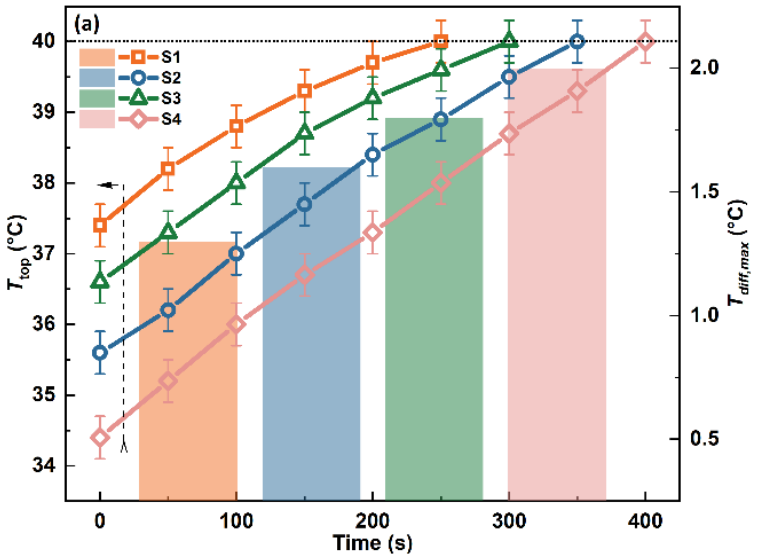


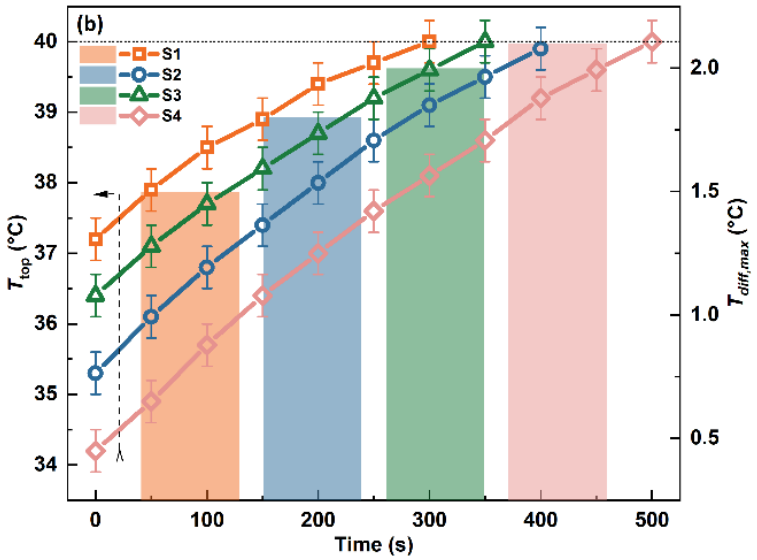
Fig. 5. 4 Variation of adhesion work at the liquid-solid interface of a (a) 2 μL; (a) 4 μL; (a) 6 μL; (a) 8 μL droplet during evaporation.

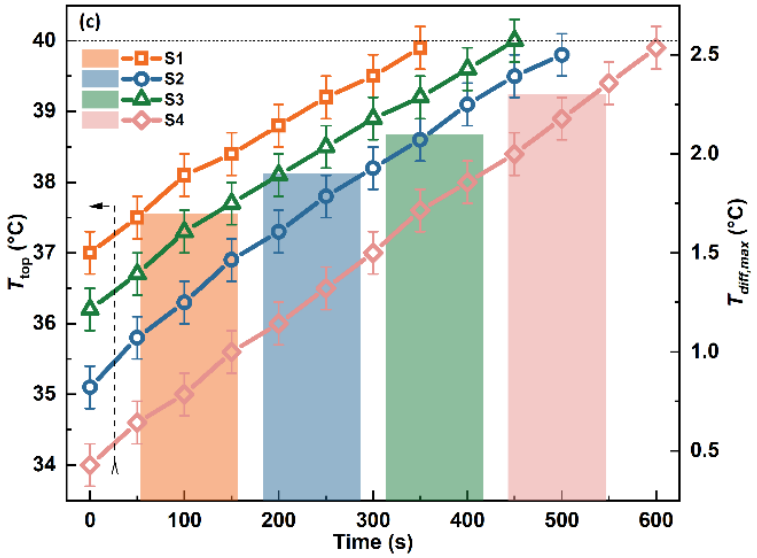
5.3.2 The effect of surface roughness on the droplet interfacial heat transfer

The effect of surface roughness on wettability was introduced in the previous section. This section will also introduce the influence of the surface roughness on the silica nanofluid droplet heat and mass transfer. Under different surface roughness, the temperature change trend at the top of the 2 μL silica nanofluid droplet with time is shown in the line chart in Fig. 5.5 (a). It can be seen from Fig. 5.5 (a) that with the increase of the surface roughness degree, the temperature at the top of the droplet (T_{top}) keeps increasing. The T_{top} increased from about 34.4℃ to 37.4 ℃, improving 8.7%, when the substrate surface changed from S4 to S1. This may be because as the surface roughness degree increases, the droplet height becomes lower, which enhances the heat conduction process inside the droplet, thereby increasing the temperature of the liquid-vapour interface. Under other droplet volume conditions, the maximum increase in T_{top}

is also around 8.7%, meaning that volume changes have little impact. On the other hand, it can also be seen from the bar chart in Fig. 5.5 (a) that as the roughness decreases, the maximum difference between the temperature at the top of the droplet and the temperature in the contact line area ($T_{diff,max}$) also becomes more significant. The $T_{diff,max}$ of the silica nanofluid droplet increased from about 1.3℃ on the surface S1 to about 2℃ on the surface S4, which is an increase of approximately 54%. As the roughness increases, the evaporative cooling effect of the liquid-vapour interface is also enhanced, which may be due to the reduced surface wettability, inhibiting the heat transfer process inside the droplet, thus promoting the evaporative cooling effect. The $T_{diff,max}$ difference on the surface of S1 and S4 also change to 40%, 35%, and 32% as the volume increases to 4 μL, 6 μL, and 8 μL, respectively. Then, these kinds of trends also remain unchanged, with the droplet volume gradually increasing to 4 μL, 6 μL, and 8 μL. As shown in Fig. 5.5 (b-d), the temperature at the droplet's top gradually increases and stabilizes at about 40℃. With the silica droplet volume increase, the T_{top} also decreases in the initial stage, like the S1 surface decline of about 2%. It may be due to the droplet height increasing with droplet volume, suppressing droplets inside heat transfer and further enhancing the evaporative cooling effect, making the temperature of the liquid-vapour interface decline. At the same time, with the increase of silica nanofluid droplet volume, $T_{diff,max}$ also increases significantly, such as increasing by 25% on the S4 surface from 2 μL to 8 μL, which could be attributed to the enhanced evaporative cooling effect.


(a)
S1
S2
S3
S4
T_{top} (°C)
$T_{diff,max}$ (°C)
Time (s)


(b)
S1
S2
S3
S4
T_{top} (°C)
$T_{diff,max}$ (°C)
Time (s)


(c)
S1
S2
S3
S4
T_{top} (°C)
$T_{diff,max}$ (°C)
Time (s)

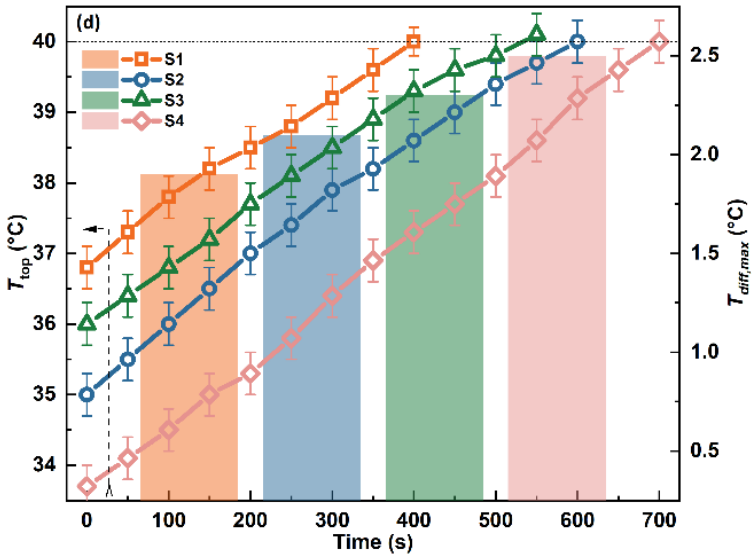


Fig. 5. 5 The temperature change of the droplet top region T_{top} with time and the maximum temperature difference in liquid-vapour interface $T_{diff,max}$ when the droplet volume is (a) 2 μL; (b) 4 μL; (c) 6 μL; (d) 8 μL.

Then, as shown in Fig. 5.6, the temperature distribution of the liquid-vapour interface of the silica nanofluid droplets of different volumes on the S4 surface. It can be seen from Fig. 5.6 (a-d) that on the S4 surface, droplets with various volumes have a relatively pronounced evaporative cooling effect in the initial stage. At the liquid-vapour interface, the temperature in the top centre region is significantly lower than in the contact line region. As the evaporation proceeds, the temperature distribution at the liquid-vapour interface gradually becomes uniform, stabilising at about 40 ℃ in the final evaporation stage.

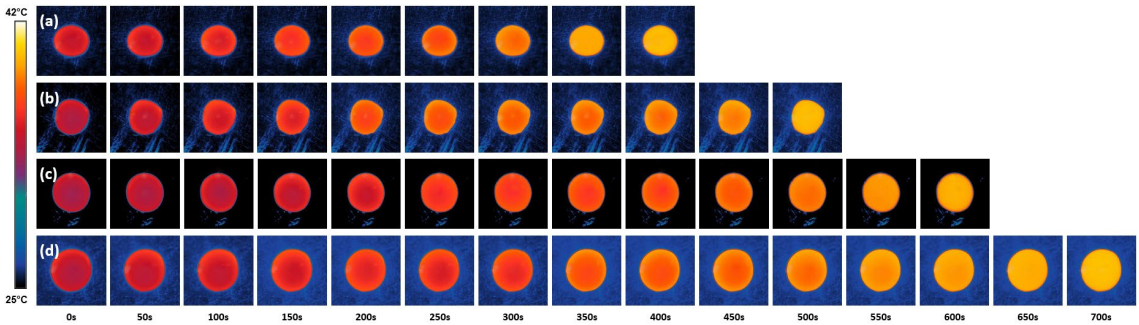


Fig. 5. 6 The evolution of interface temperature distribution of (a) 2 μL; (b) 4 μL; (c) 6 μL; (d) 8 μL

droplet on the S4 surface with time.

5.3.3 The effect of surface roughness on the nanofluid droplet sedimentary pattern

The previous sections analysed the effects of roughness on the surface wettability and silica nanofluid droplet interfacial heat and mass transfer processes during the evaporation process. In this section, we will discuss the sedimentary pattern of silica nanofluid droplets after the evaporation process and analyse its relationship with surface roughness. In this experimental study, nanofluid droplets produced a coffee-ring effect after evaporating on surfaces with different degrees of copper roughness. The sedimentary pattern of 2 μL silica nanofluid droplets on the surfaces S1 to S4 is shown in Fig. 5.7 (a-d). As the surface roughness decreases, the sedimentary pattern becomes more precise and complete. It may be owed that as the surface roughness decreases, the substrate surface wettability decreases, and the evaporative cooling effect of the droplets is also enhanced. In this way, the temperature difference between the top and edge regions of the sessile droplet becomes more significant, which enhances the Marangoni effect inside the silica nanofluid droplet, which in turn leads to a faster and more massive aggregation of silica nanoparticles inside the droplet to the contact line region via Marangoni flow. It can be concluded that increasing the roughness of the copper surface can inhibit the coffee-ring effect to a certain extent. At the same time, it can also be seen from Fig. 5.7 (a-d) that as the roughness increases, the coffee-ring sedimentary pattern becomes unclear, and its shape also becomes more irregular. This is because during the wetting process, after the droplet adheres to the surface, the contact line is restricted by the large grooves on the rough surface and cannot move

evenly around but is hindered, limiting the contact line's roundness and further affecting the sedimentary pattern.

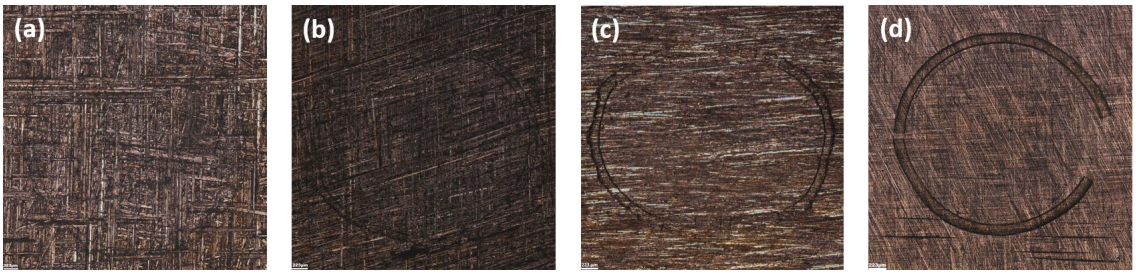
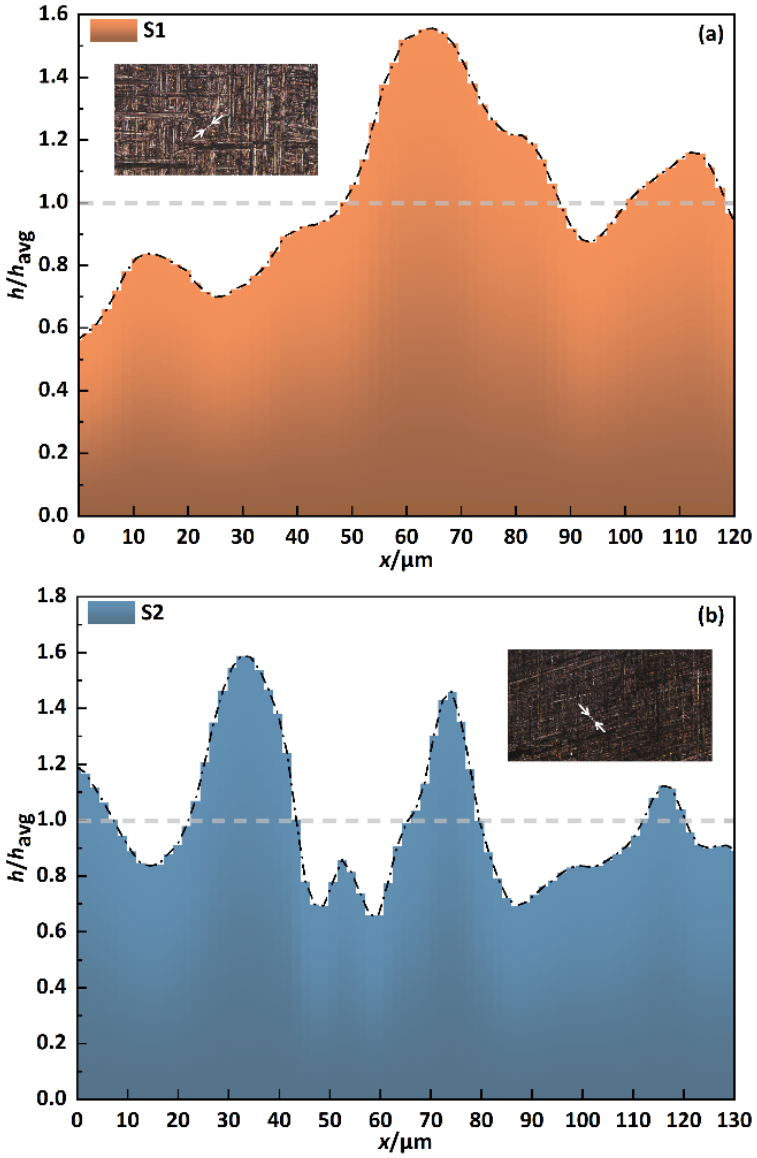


Fig. 5. 7 The sedimentary pattern after the evaporation of 2 μL silica nanofluid droplet on the (a) S1, (b) S2, (c)S3, and (d)S4 surfaces, respectively.

At the same time, the relative height distribution statistics of the coffee-ring sedimentary pattern of silica nanofluid droplets under different roughness surfaces are shown in Fig. 5.8 (a-d). As shown in Fig. 5.8 (a), the range of horizontal coordinates represents the width of the sedimentary coffee-ring pattern marked by the white line in the illustration within Fig. 5.8 (a). h/h_{avg} represents the dimensionless height of the sedimentary coffee-ring pattern, which means the ratio of the height of each location to the overall average height. In the dimensionless height distribution of the coffee ring formed on the surface of S1, the maximum value differs from the minimum value by a factor of about 2.6. Meanwhile, as shown in Fig. 5.8 (b-d), the difference between the maximum and minimum values of the dimensionless heights of the silica nanofluid droplets increased to about 2.7, 5.9, and 8.5 times when the droplets were located on the S2, S3, and S4 surfaces, respectively. This phenomenon is due to several reasons. Firstly, as the surface roughness degree increases, the coffee-ring phenomenon of the silica nanofluid droplet is suppressed. This makes the coffee-ring sedimentary pattern relatively insignificant, leading to a flatter distribution of dimensionless heights. Second, as the roughness decreases, the copper substrate surface becomes smoother,

allowing the silica nanoparticles to be deposited chiefly on the surface rather than in the grooves, contributing to a more differentiated distribution of dimensionless heights.



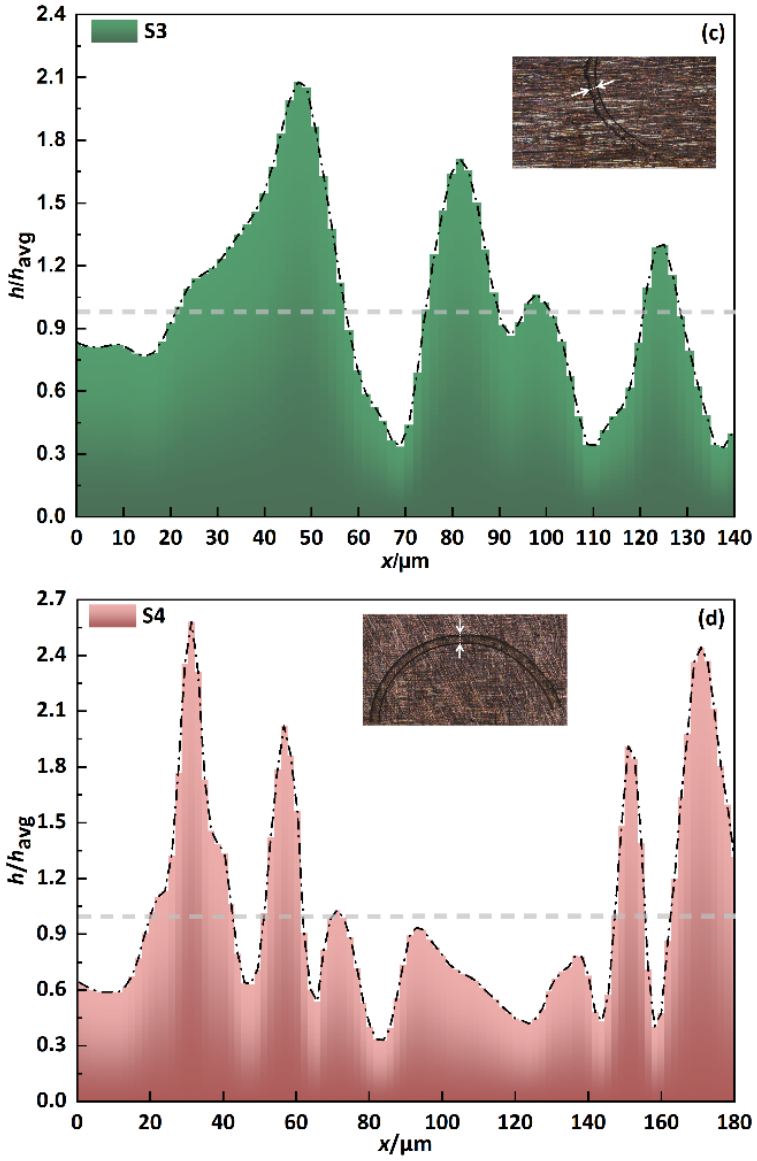


Fig. 5. 8 Dimensionless height of the cross-section of the sedimentary ring after evaporation of a 2 μL silica nanofluid droplet on the (a) S1, (b) S2, (c) S3, (d) S4 surface.

Also, the pattern of sedimentary coffee rings formed on the surface of the copper substrate after the evaporation of different volumes of silica nanofluid droplets is shown in Fig. 5.9, where only the roughest S1 surface and the smoothest S4 surface were selected for comparison to clarify the differences. As shown in Fig. 5.9 (a-c), the diameter of the sedimentary coffee-ring pattern increases as the droplet volume

improves. At the same time, the sedimentary coffee-ring patterns remain visible as the droplet volume increases, and all these have about 1-4 fractures. As shown in Fig. 5.9 (c), a localized 3D surface measurement of the fractures by optical profilometer shows that there are almost no residual silica nanoparticles left at the fracture regions, which indicates that the fractures appeared abruptly after the silica nanofluid droplet evaporation and the formation of the sedimentary coffee-ring patterns. Meanwhile, it can be seen in Fig. 5.9 (d-f) that the coffee-ring effect appears regardless of the increase in droplet volume. Still, the sedimentary coffee-ring pattern produced by the droplet's evaporation is not apparent, and the ring deposition pattern has many fractures (more than 10). Although the sedimentary coffee-ring patterns fractured on both surfaces, the causes differed. On the smooth surface (S4), the sedimentary coffee-ring pattern formed gradually and entirely during evaporation. In contrast, the fracture may be attributed to the bottom heating, which caused the sedimentary coffee-ring pattern to receive thermal stresses. Some localized thermal stresses were stronger than the inherent strength of the silica sedimentary ring itself, and thus, a sudden fracture occurred after the evaporation was completed. Meanwhile, on the rough surface (S1), the surface grooves were much more numerous than those on the smooth surface and had a greater depth, resulting in a poorer flatness. In this way, when the nanoparticles gather and deposit toward the contact line area during the evaporation process, the coffee-ring sedimentary pattern formed by them is subject to natural uneven stress distribution at the bottom, which makes many fractures generated, so it may not be possible to form a complete and continuous ring sedimentary pattern during the evaporation process.

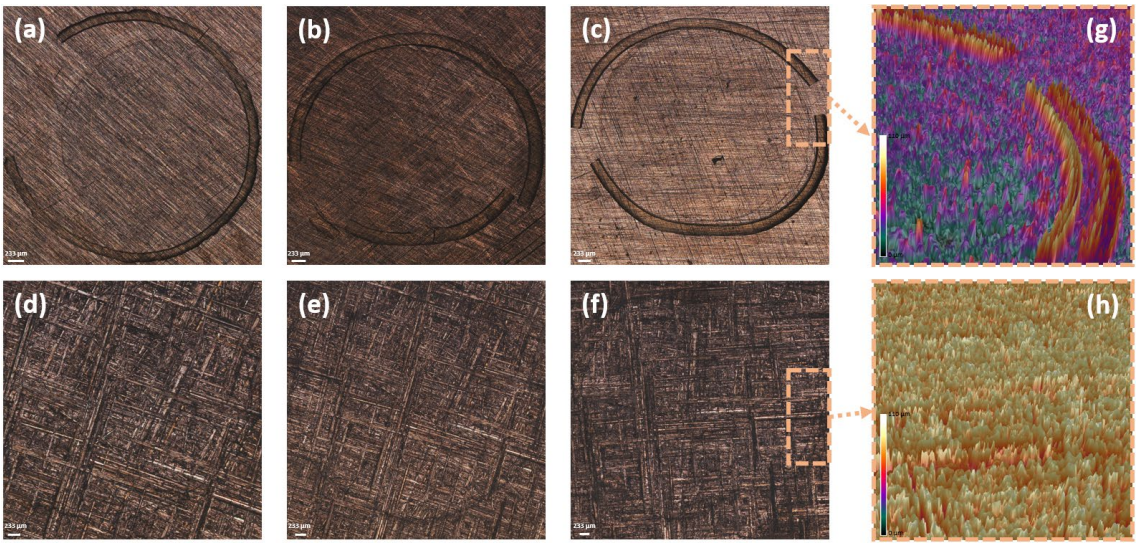


Fig. 5. 9 Microscope images of the sedimentary coffee-ring patterns of (a) 4; (b) 6; and (c) 8 μL silica nanofluid droplets placed on the S4 surface; Microscope images of the sedimentary coffee-ring patterns of (d) 4; (e) 6; and (f) 8 μL silica nanofluid droplets placed on the S1 surface; (g) and (h) is the optical profile of the selected area.

5.4 Chapter summary

In this chapter, the effect of copper surface roughness on the evaporation dynamics of the sessile silica nanofluids droplet is investigated experimentally. There are many studies on the evaporation phenomenon and deposition pattern of silica nanofluid droplets [248] [249, 250], including its deposition mechanism or the effect of surfactant addition. However, this chapter is unique in that it studies the effect of surface roughness on the coffee deposition cracks of silica nanofluid droplets. The results show that based on the hydrophilic copper surface, the surface wettability increases with increasing roughness, reducing the contact angle of the nanofluid droplets. Correspondingly, the height change of droplets is not significantly affected by roughness, and the change rate is slow in the early evaporation stage and increases sharply in the later stage. Meanwhile, the evaporation of nanofluid droplets on the S1,

S2, and S3 surfaces follows the CCR pattern regardless of the droplet volume. However, on the S4 surface, the evaporation is in the CCR mode in the beginning and middle stages but changes to the mixed mode in the last 10%-20% of the total process approximately. In addition to wettability, the experiment also observed the effect of roughness on the heat transfer process at the liquid-vapour interface of silica nanofluid droplets. As the surface roughness decreases, the adhesion work between the droplet and the solid-liquid interface also decreases. When the surface changes from S1 to S4, the initial adhesion work, on average, decreases by about 45%. At the same time, as the roughness decreases, the temperature at the apex of the liquid-vapour interface also decreases, and the temperature difference between the top liquid-vapour interface and contact line region also increases, up to about 2.5℃, indicating that increasing the surface roughness can suppress the evaporative cooling effect of the nanofluid droplet during evaporation. Similarly, substrate roughness also impacts the coffee-ring effect of silica nanofluid droplets. As the roughness increases, the coffee-ring sedimentary pattern of the nanofluid droplets becomes less pronounced due to the dual reasons of deep surface grooves for greater roughness and suppression of the Marangoni flow. Experimental results show that forming rounded droplet and coffee ring deposition patterns on rough surfaces is challenging but accessible on smooth surfaces. On the smoother surface, there are fewer fractures in the coffee-ring sedimentary pattern, and the relative height difference of the sedimentary pattern is more pronounced, with a maximum amplitude of up to 8.5 times. Besides, regardless of the change in droplet volume, the effect of surface roughness on the sedimentary pattern remains unchanged. In inkjet printing, paint coating, plant fertilization, and even medical testing, regulating the shape and cracks of the coffee ring deposition pattern will significantly affect its

effect. This study hopes to guide the research related to the effect of roughness on the evaporation of nanofluid droplets and its subsequent practical application.

Chapter 6. Effect of loaded carbon-based nanoparticles on the evaporation dynamics of sessile droplets

This chapter prepared the nanofluid droplets based on two common carbon-based nanomaterials, multi-walled carbon nanotubes (MWCNTs) and multi-layer graphene (MLG). The monocrystalline silicon wafer is used as the substrate, and the substrate temperature is controlled between 50 °C and 80 °C as the external factors. The effects of adding different carbon-based nanoparticles on droplet wettability, contact line movement, and heat and mass transfer processes at the liquid-vapour interface were explored under different heating conditions. At the same time, the experimental study would also focus on the effect of nanoparticle type on the sedimentary pattern.

6.1 Chapter introduction

Carbon-based materials mainly refer to materials with carbon as the main body, among which high-performance materials such as graphene and carbon nanotubes have been widely used in industrial production and scientific research [251, 252]. So far, although there have been many studies focused on carbon-based nanofluids, not many studies have been done on the evaporation of loaded droplets in multi-walled carbon nanotubes and multilayer graphene, which are typical and widely used carbon-based nanomaterials, and comparative studies on its evaporation dynamics on heated silicon wafers are even rarer, which also need to be explored further. Besides, in the process of evaporation of carbon-based nanofluid droplets, the sedimentary of nanoparticles is inevitably accompanied, and the sedimentary process would not only affect the enhanced heat transfer process of the cooling system but also should be considered in

the manufacture of electronic equipment [253, 254] and inkjet printing [255]. Therefore, exploring the evaporative and sedimentary processes of nanofluid droplets from different carbon-based materials and the influence of substrate temperature on them is significant. In this chapter, based on the multi-wall carbon nanotubes and multilayer graphene nanoparticles, the influence of substrate temperature on the evaporation dynamics and the sedimentary pattern of the nanoparticles-laden droplet was investigated experimentally, which is expected to guide the direct cooling or printing of electronic devices based on carbon-based nanofluids.

6.2 Experimental methods

6.2.1 Experimental setup

The experimental devices used in this study are also shown in Fig. 3.2. At the same time, a 1-inch diameter monocrystalline silicon wafer was selected as the substrate for placing the nanofluid droplets, and the surface of the silicon wafer was polished. The morphology parameters of the polished surface are shown in Table 6.1. Meanwhile, the monocrystalline silicon wafer is placed on a temperature-controlled heating panel. In this experiment, the substrate temperature is controlled between 50 - 80 °C. Before each experiment, each silicon wafer was cleaned by ultrasound in an isopropyl alcohol solution for at least 10 min and then dried using an air jet. And the droplets were extracted and placed using pipettes (Eppendorf Research plus, Germany) during the experiments. The ambient temperature of each test in the laboratory was controlled between 20 and 24 °C, and the relative humidity was controlled between 50% and 60%.

Table 6. 1 Silicon wafer polishing surface parameters

Surface parameters	Value
surface flatness (Total Indicator Reading, TIR)	TIR < 3 μm
Warp (Total Thickness Variation, TTV)	TTV < 10 μm
Wafer curvature (BOW)	BOW < 10 μm
Surface roughness	< 0.5 nm
Surface granularity	< 10 (for size > 0.3 μm)

6.2.2 Nanofluid preparation

This study uses multi-walled carbon nanotubes (MWCNTs) and multilayer graphene (MLG) nanoparticles as carbon material, and their physical properties are shown in Table 6.2. Both MWCNTs and MLG nanofluid were prepared using the two-step method [243], which can enhance the stability of nanofluids. In this experiment, the deionised water was selected as the base fluid. The nanoparticles were then dispersed into the base liquid, and the surfactant sodium dodecyl sulfate (SDS) was also added to the nanofluid, which purpose to make the MWCNTs and MLG nanoparticles uniformly and stably dispersed in the liquid so that the stability of the nanofluid was further enhanced. The nanoparticles are then mixed with the solvent using ultrasonic vibration and stirring for at least 30 minutes. In the finally prepared nanofluid, the mass concentration of MWCNTs and MLG was controlled at 0.5 wt%, and the mass concentration of the surfactant SDS was controlled at 1.0 wt%.

Table 6. 2 Basic physical parameters of nanoparticles

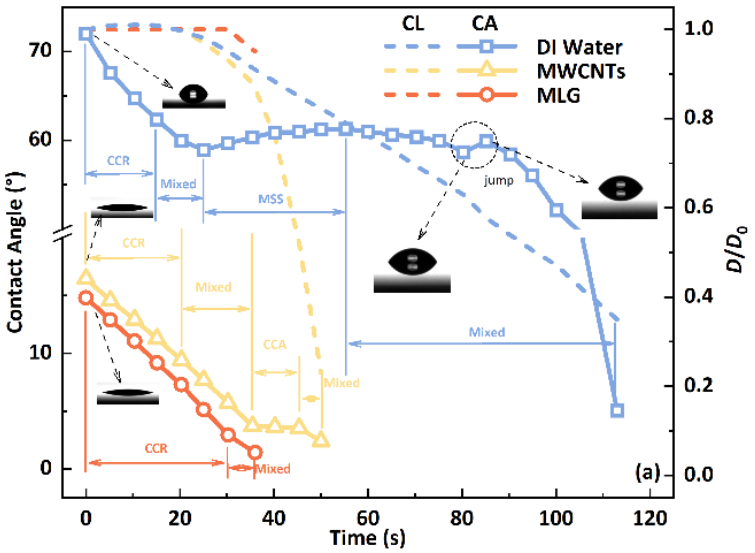
	MWCNTs	MLG
Diameter	Inner: 3-5; Outer: 8-15nm	7-10 μm
Length/Thickness	3-12 μm	< 100 nm (1-3 layers)
Carbon content	> 95 wt%	> 98 wt%
Density (g/cm^3)	0.15	0.08-0.13
Thermal conductivity (W/m·k)	2000-6000 [256]	2000-6000 [257]

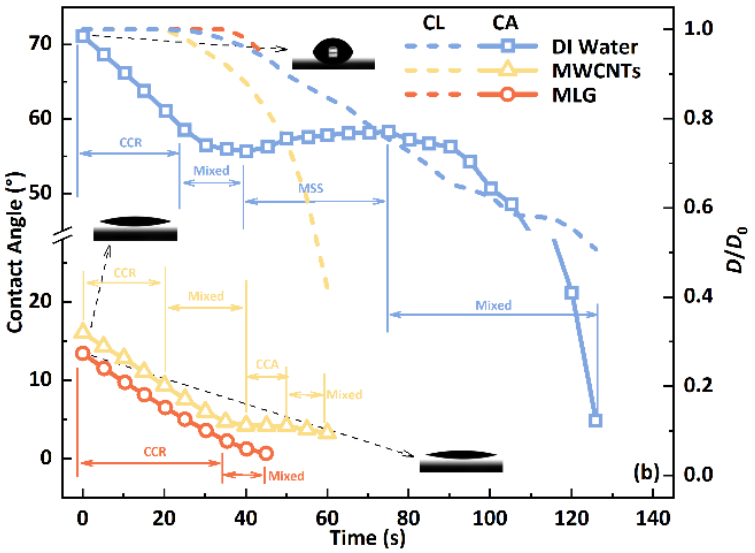
6.3 Results and discussion

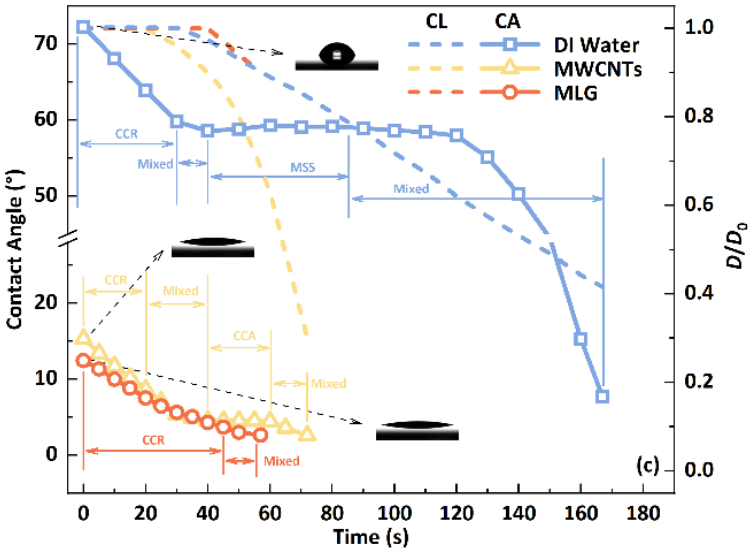
6.3.1 Effect of different carbon-based nanoparticles on the heat and mass transfer process

In this study, the effect of different additions of carbon-based nanoparticles on droplet wetting properties and evaporate modes compared to pure DI water was carried out, and the substrate heating temperature was controlled at 50 °C. As shown in Fig. 6.1 (a-d), compared with pure DI water, adding MWCNTs and MLG nanoparticles can significantly reduce the contact angle and evaporation time of droplets. From Fig. 6.1 (a) to Fig. 6.1 (c), when the droplet volume increases from 0.5 μL to 1.5 μL, the contact angle of the carbon-based nanofluid droplets is all around 15°, while the contact angles of the pure water droplets are all around 72°. At the same time, compared with pure water, adding MWCNTs and MLG nanoparticles can reduce the total evaporation time of droplets by an average of 55% and 66%, respectively. This should be due to the addition of carbon-based nanoparticles, which significantly increase the thermal conductivity of the droplets, thus enhancing the heat transfer and evaporation efficiency. At the same time, the addition of nanoparticles also considerably changes the

evaporation mode of droplets. As shown in Fig. 6.1 (a), when pure water droplets evaporate on the Si wafer, it is in the early stage's constant contact radius (CCR) mode. Then, the droplets change to the mixed evaporation mode in which the contact line (CL) and contact angle (CA) decrease simultaneously. As the evaporation proceeds further, the contact line of the droplets continues to decline, but the contact angle increases, which kind of state could be called mixed stick−slip (MSS) mode [258]. Afterwards, the evaporation mode returned to the mixed mode, and the contact angle jumping behaviour appeared in this process. At the same time, when a 0.5 μL MWCNTs nanofluid droplet evaporates on the Si wafer, the droplet is also in the CCR mode in the initial stage, then transitions to the mixed mode and CCA mode and ends in the mixed mode in the final stage of evaporation. Meanwhile, when 0.5 μL MLG nanofluid droplets evaporate on the Si wafer, the droplet evaporation remains in the CCR mode and changes to the mixed mode in the final stage. Also shown in Fig. 6.1 (b) and (c), when the droplet volume increases to 1.0 and 1.5 μL, the evaporation modes experienced by the three droplets remain unchanged. Among them, the CCR mode takes the longest time during the evaporation process of MLG nanofluid droplets, and it may be attributed to the addition of MLG nanoparticles and surfactant that reduces the surface tension, making it insufficient to drive the movement of the contact line. In addition, as shown in Fig. 6.1 (d), compared with MWCNTs, the addition of MLG can always lead to better wettability of droplets and higher evaporation efficiency, which can be mainly attributed to the enhancement of thermal conductivity and wettability.


CL
CA
DI Water
MWCNTs
MLG
Contact Angle (°)
D/D0
Time (s)
CCR
Mixed
MSS
jump
CCA
(a)


CL
CA
DI Water
MWCNTs
MLG
Contact Angle (°)
D/D0
Time (s)
CCR
Mixed
MSS
CCA
(b)


CL
CA
DI Water
MWCNTs
MLG
Contact Angle (°)
D/D0
Time (s)
CCR
Mixed
MSS
CCA
(c)

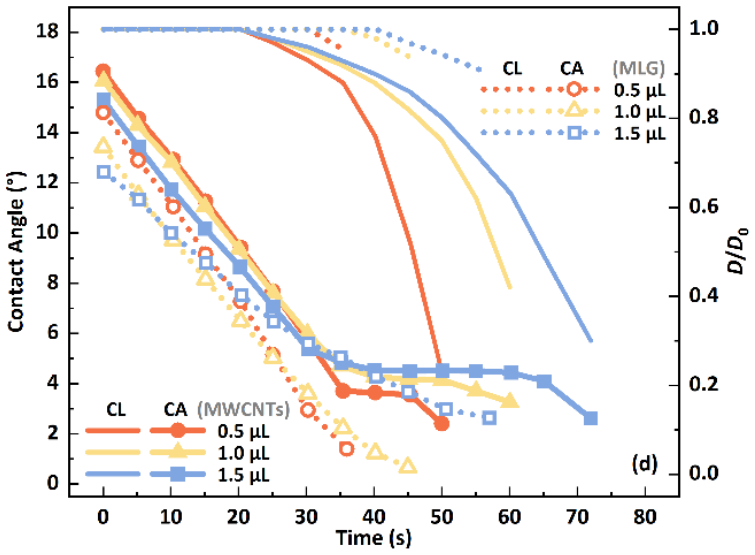
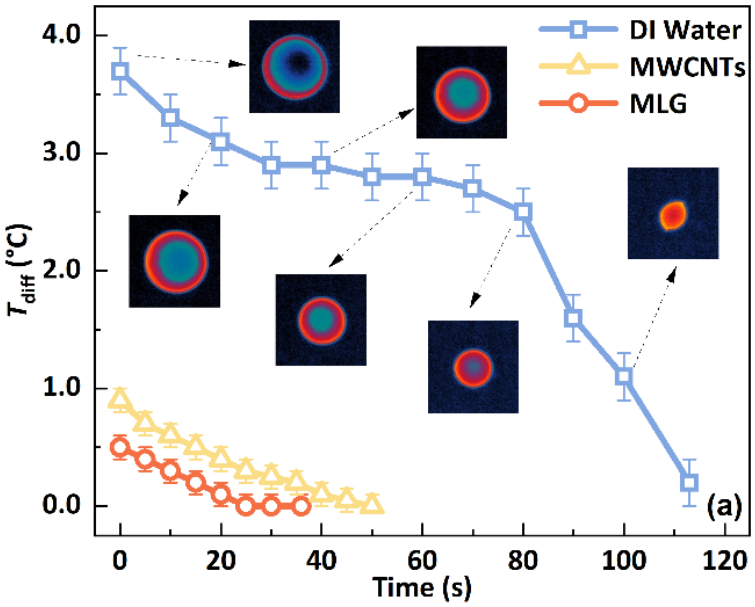
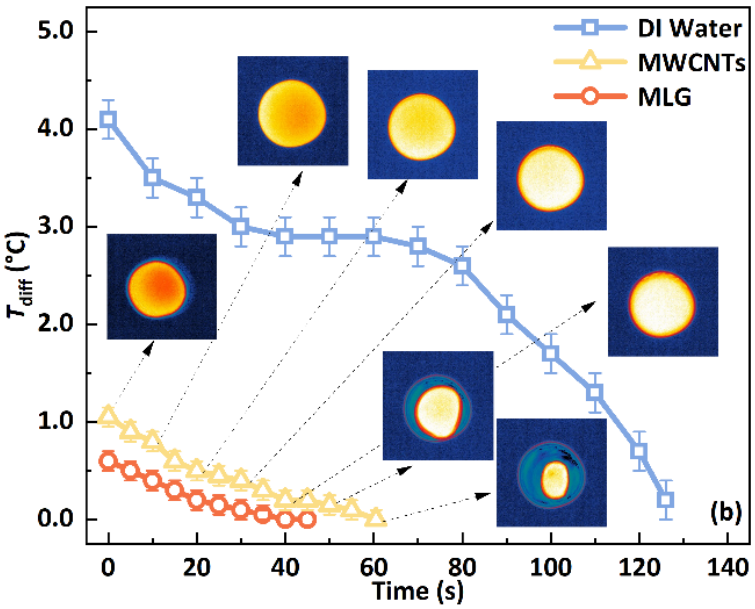


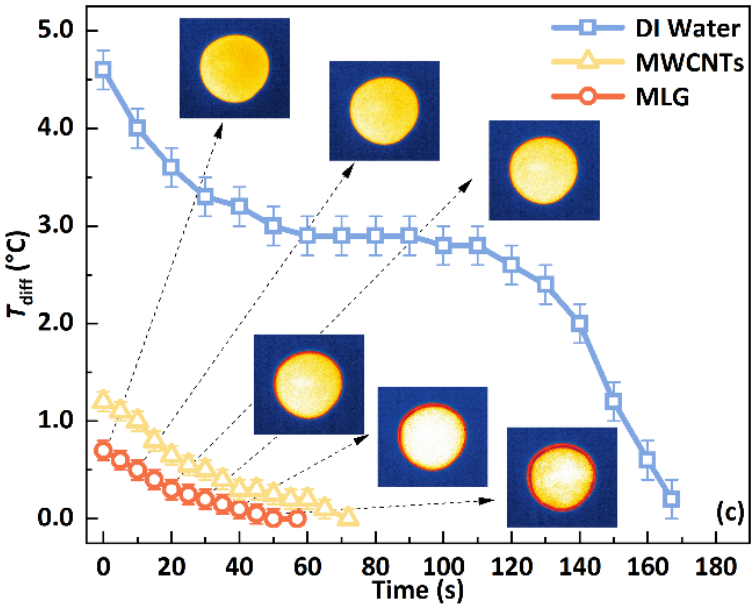
Fig. 6. 1 Changes in contact angle and contact line during evaporation for (a) 0.5 µL, (b) 1.0 µL, (c) 1.5 µL DI water, MWCNTs, and MLG nanofluid droplets and (d) the carbon-based nanoparticles comparison.

Subsequently, under the same external conditions, during the evaporation process of different types of droplets, the temperature difference between the top of the droplet and the contact line area (T_{diff}) changes with time, as shown in Fig. 6.2 (a-d). As shown in Fig. 6.2 (a), when the droplet volume is controlled to 0.5 µL, the T_{diff} of the DI water droplets is significantly higher than that of MWCNTs and MLG nanofluid droplets. For example, in the initial stage, the T_{diff} of DI water droplets is about 3.7 °C, while the T_{diff} of MWCNTs and MLG nanofluid droplets are about 0.9 and 0.5 °C, respectively. This may be attributed to the enhanced liquid thermal conductivity and wettability suppressing the evaporative cooling effect. At the same time, it is also evident from the illustration in Fig. 6.2 (a) that as the evaporation process proceeds, the temperature uniformity of the droplet liquid-vapour interface is improved, and the evaporative cooling effect is also suppressed. Similarly, when the droplet volume increases to 1.0 and 1.5 µL, the T_{diff} of the three kinds of droplet changes with time, as shown in Fig.

6.2 (b) and (c). As the droplet volume increases, the T_{diff} also increases at the initial moment, such as the T_{diff} of DI water droplet increased by 11% and 24% when the volume rises to 1.0 and 1.5 μL, respectively. In addition, the changes of T_{diff} with time for MWCNTs and MLG nanofluid droplets under different volume conditions are shown in Fig. 6.2 (d). Compared with MLG nanofluid, the T_{diff} of MWCNTs nanofluid droplets is always larger. For example, under the conditions of 0.5, 1.0, and 1.5 μL, the T_{diff} increases by 80%, 75%, and 71%, respectively. It may be owed that the addition of MLG nanoparticles makes the surface tension of the liquid more minor, and the droplet wettability is more muscular, which strengthens the thermal conductivity inside the droplet, thereby inhibiting the evaporative cooling effect.




DI Water
MWCNTs
MLG
T_{diff} (°C)
Time (s)
(b)


DI Water
MWCNTs
MLG
T_{diff} (°C)
Time (s)
(c)

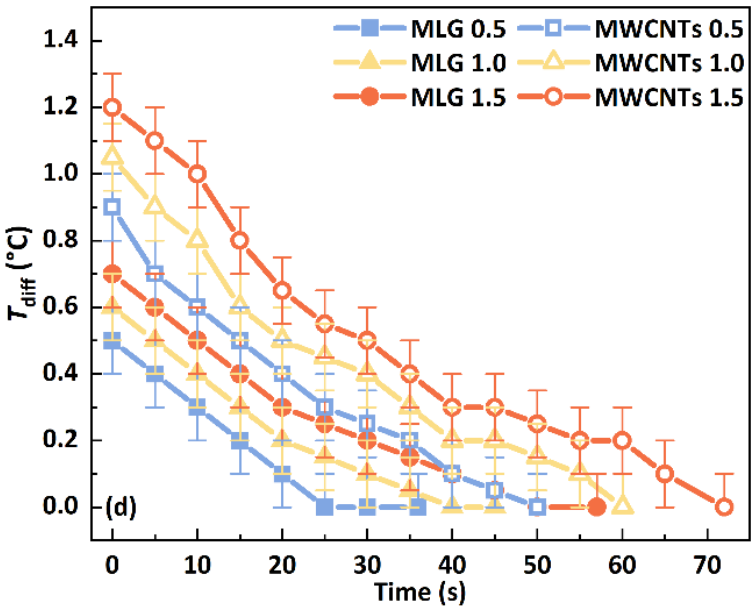
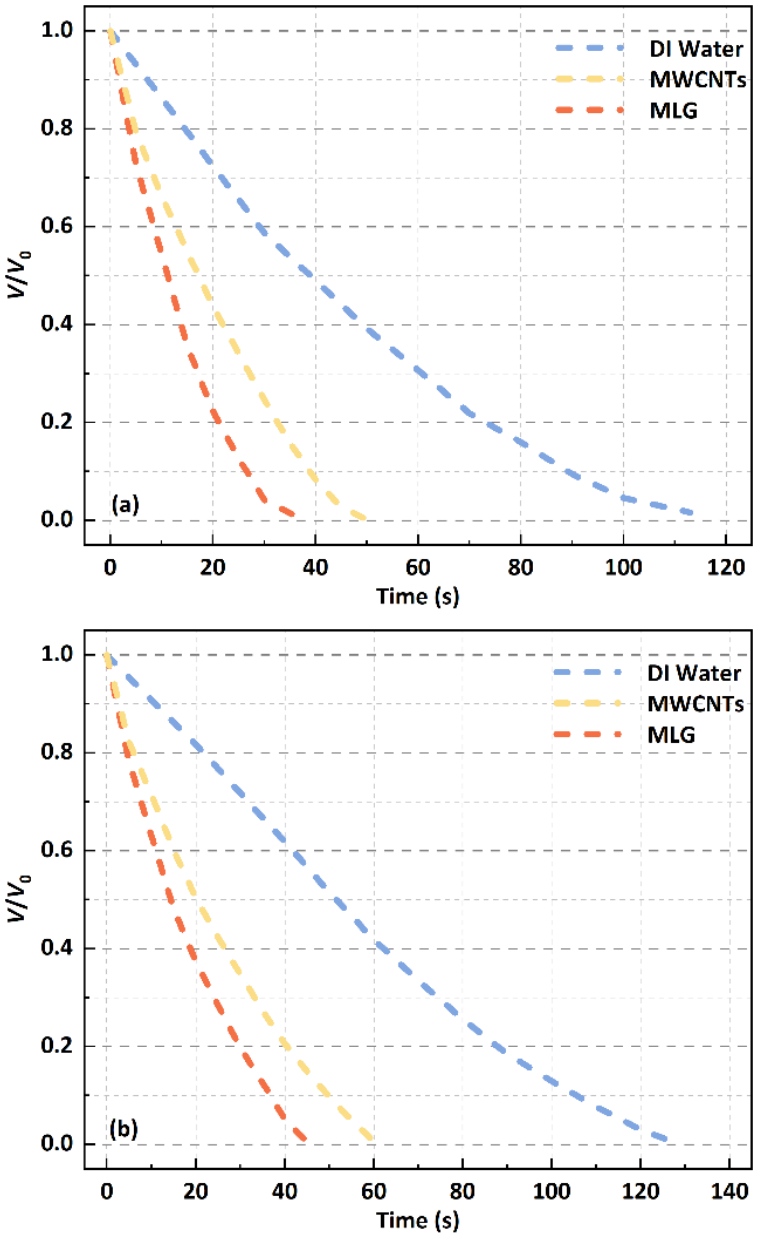


Fig. 6. 2 Temperature difference at the edge and top of liquid-vapour interface of (a) 0.5 µL, (b) 1.0 µL, (c) 1.5 µL DI water, MWCNTs, and MLG nanofluids with time.

At the same time, the dimensionless volumes (V/V_0) of different volumes change with time during the evaporation process, as shown in Fig. 6.3 (a-d). It can be seen from Fig. 6.3 (a) that when the droplet volume is 0.5 µL, the average evaporation rate of the carbon-based nanofluid droplets is greater. Compared with pure DI water, adding MWCNTs and MLG nanoparticles increases the average evaporation rate of the droplets by approximately 1.2 and 2.1 times, respectively. Similarly, as shown in Fig. 6.3 (b), when the droplet volume is 1.0 µL, adding MWCNTs and MLG nanoparticles increases the average evaporation rate of the droplets by approximately 1.2 and 1.9 times compared with pure DI water droplets. When the droplet volume increased to 1.5 µL, this value became 1.36 and 2 times. At the same time, the comparison of different carbon-based nanofluid droplet average evaporation rates at different volumes is shown in Fig. 6.3 (d). It can be seen from Fig. 6.3 (d) that the evaporation rate of the MLG nanofluid droplets is still faster than MWCNTs nanofluid droplets. At the same time,

with the increase of the droplet volume, the evaporation rate of the droplets loaded with carbon-based nanoparticles increases faster than that of the DI water droplets, which can be attributed to the fact that the evaporative cooling effect at the liquid-vapour interface is more obvious on the DI water droplets, thereby inhibiting evaporation more severely.



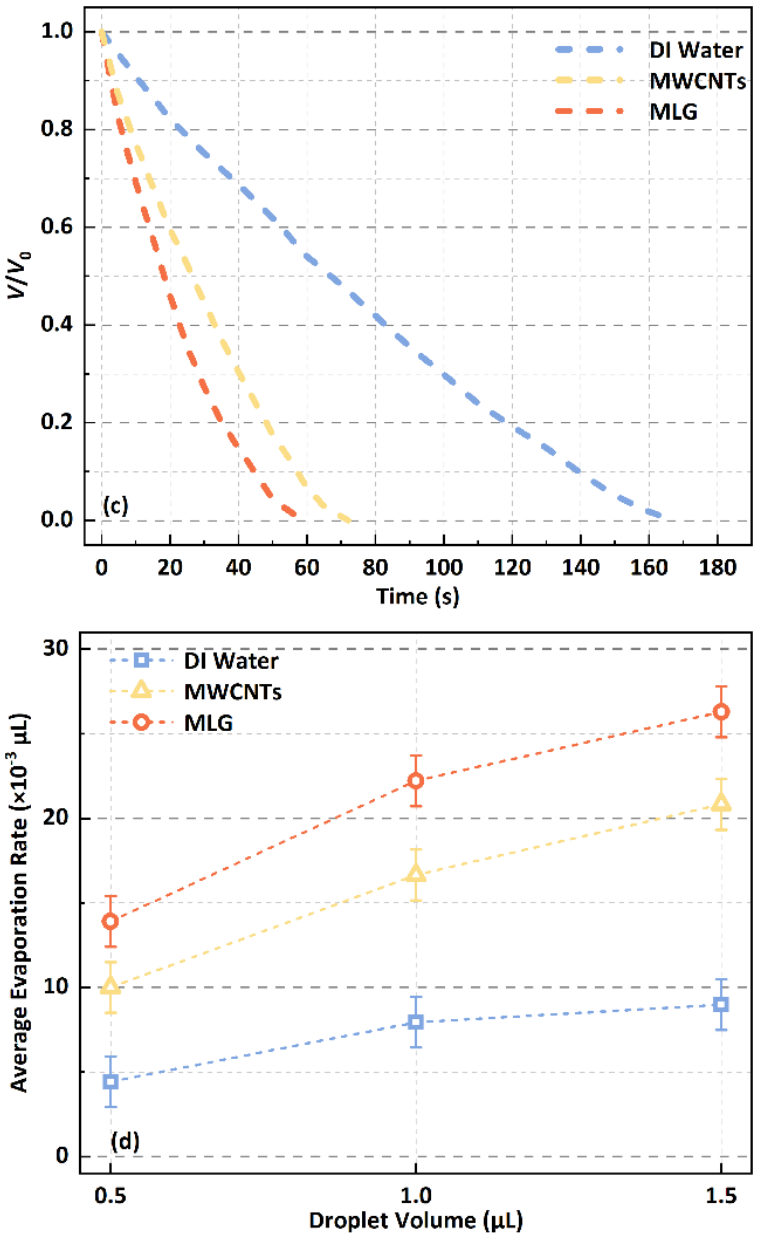


Fig. 6. 3 (a) 0.5 µL, (b) 1.0 µL, (c) 1.5 µL droplet dimensionless volume changes with time of DI water and carbon-based nanofluid, (d) the average evaporation rate of DI water and carbon-based nanofluid droplet with different volume.

6.3.2 Effect of substrate temperature on the droplet evaporation dynamics

After exploring the effects of different materials, this study is also conducted on the

effects of different substrate temperatures on the droplet evaporation process. As shown in Fig. 6.4, different droplets exhibit different evaporation processes at various temperatures. As the substrate temperature increases, the total evaporation time shortens significantly. The effect of substrate temperature on the evaporation of the DI water droplets is shown in Fig. 6.4 (a). When the temperature increases from 60 °C to 80 °C, the total evaporation time is shortened by approximately 63%. Under different substrate temperature conditions, the contact line will jump during the droplet evaporation. For example, when the substrate temperature is 60 °C, around the 58th second of the evaporation process of DI water droplets, the contact angle immediately increases from 21° to 52° after jumping, and the contact line is also instantly reduced by about 34%. At the same time, as shown in Fig. 6.4 (b), as the substrate temperature increases, the total evaporation time of the carbon-based nanofluid droplets also significantly decreases. When the substrate temperature increases from 60 to 80 °C, the total evaporation time of MWCNTs and MLG nanofluid droplets decreases by about 54%. Meanwhile, the initial contact angle also increases significantly with the increase in temperature. When the substrate temperature increases from 60 to 80 °C, the contact angles of MWCNTs and MLG nanofluid droplets increase by about 1.1 times and 0.9 times, respectively. As the temperature increases, the evaporation process of the MLG nanofluid droplets only experiences the CCR mode and the mixed mode. Still, the MWCNTs nanofluid droplet base has CCR, CCA, and mixed evaporation modes during the entire evaporation process.

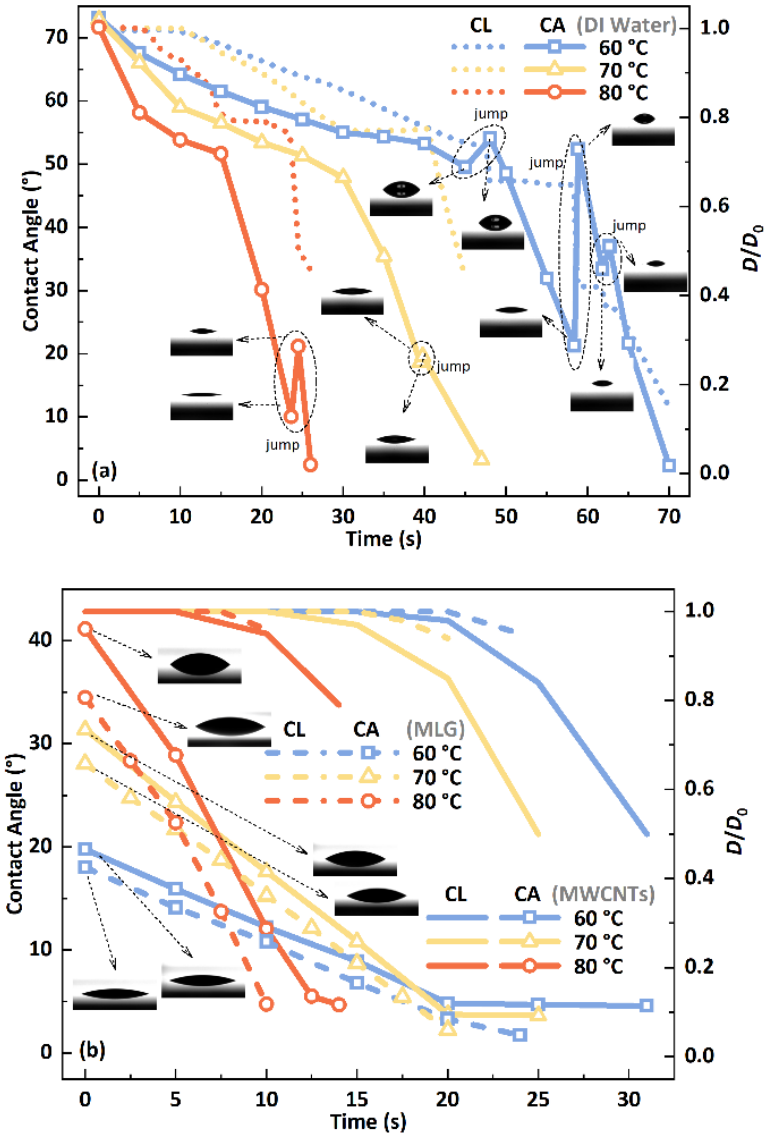


Fig. 6. 4 Changes in contact angle and contact line of 0.5 µL (a) DI water and (b) carbon-based nanoparticle-laden droplets during evaporation.

Under the same conditions, when the volume of the droplets increases to 1.0 µL, the evaporation process of DI water, MWCNTs, and MLG nanofluid droplets is shown in Fig. 6.5. With the volume increased to 1.0 µL, the DI water droplets still showed apparent jumping behaviour at the substrate temperature of 70 and 80 °C. At the same time, the entire evaporation process was relatively smooth at the substrate temperature of 60 °C. For 1.0 µL MWCNTs and MLG nanofluid droplets, the increase in substrate

temperature significantly shortened the total evaporation time. At various temperatures, the increase in droplet volume did not affect the evaporation modes of MWCNTs and MLG nanofluid droplets. Meanwhile, when the droplet volume increases to 1.5 µL, the droplet evaporation process changes with time, as shown in Fig. 6.6. As shown in Fig. 6.6 (a), the 1.5 µL DI water droplet contact line only jumped at 80°C. The droplet contact angle increased instantly from 30° to 56° at about 25th seconds. Likewise, as shown in Fig. 6.6 (b), the evaporation mode of MWCNTs and MLG nanofluid droplets also do not change with increasing droplet volume and are the same as those at 0.5 µL and 1.0 µL.

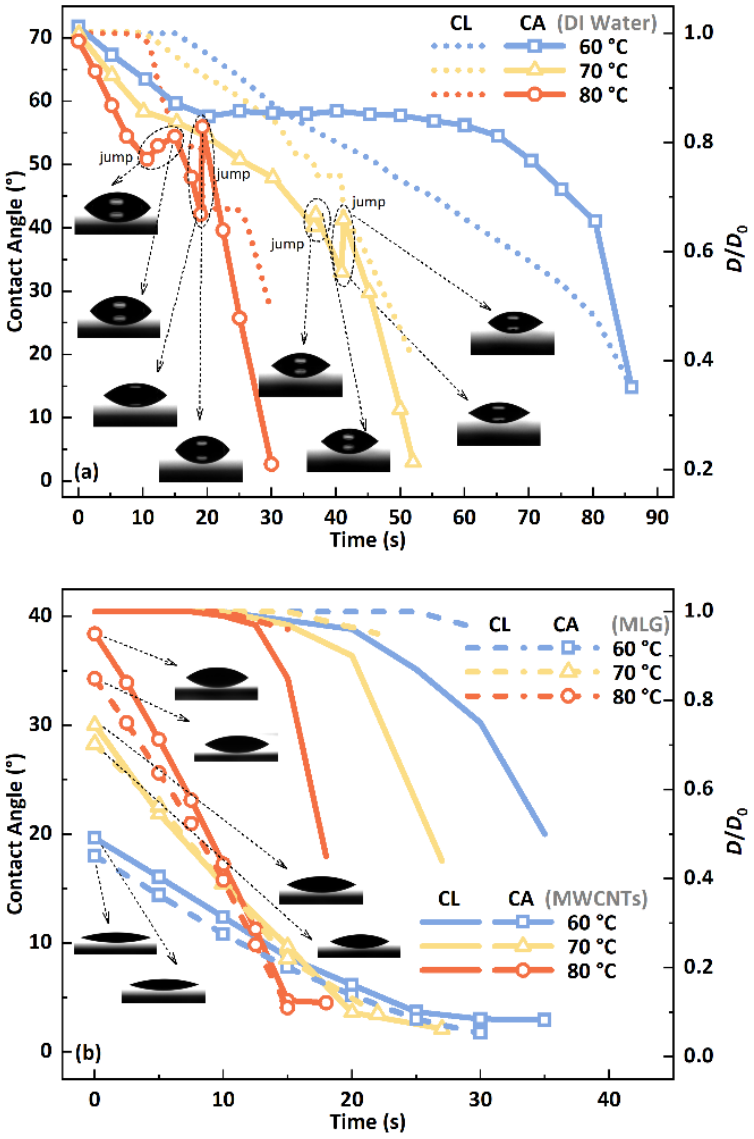


Fig. 6. 5 Changes in contact angle and contact line of 1.0 µL (a) DI water and (b) carbon-based nanoparticle-laden droplets during evaporation.

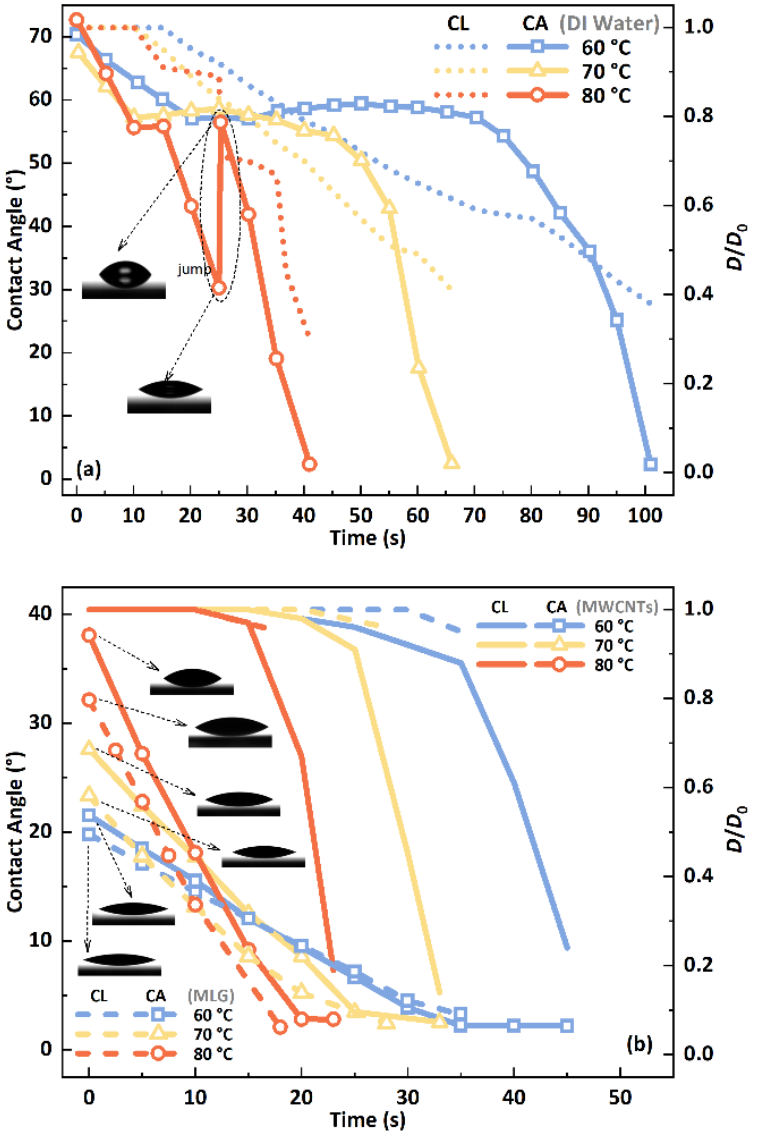
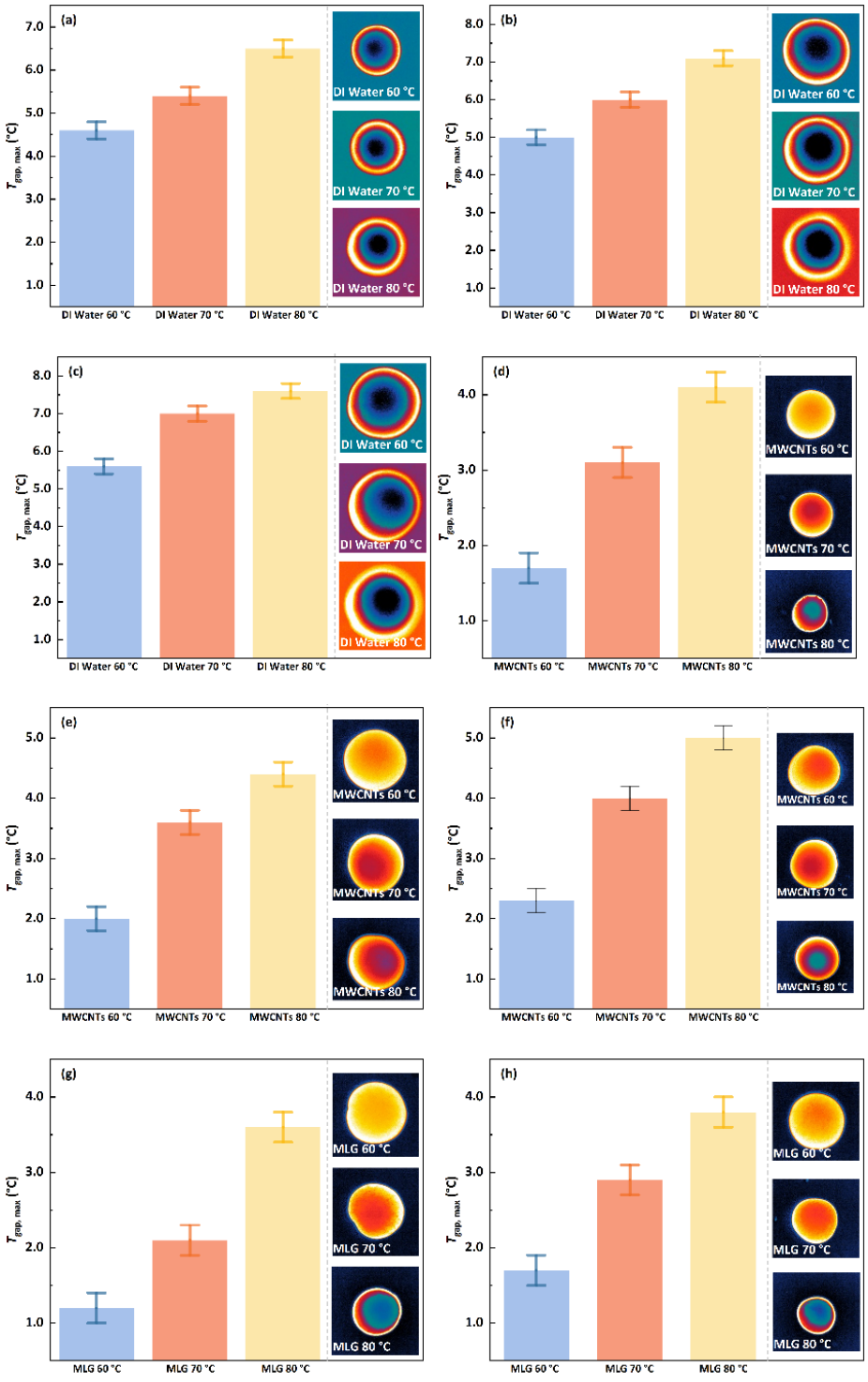


Fig. 6. 6 Changes in contact angle and contact line of 1.5 µL (a) DI water and (b) carbon-based nanoparticle-laden droplets during evaporation.

As the substrate heating temperature increases, as shown in Fig. 6.7 (a-i), the maximum value of the temperature difference ($T_{diff, max}$) at the top and edge of the droplet's liquid-

vapour interface also changes. The $T_{diff, max}$ of DI water droplets with different volumes would be changed with the substrate temperature, as shown in Fig. 6.7 (a-c). When the droplet volume increases from 0.5 μL to 1.5 μL, $T_{diff, max}$ will also rise as the substrate temperature increases. This may be due to the increased evaporation rate at the liquid-vapour interface. This causes the surface to absorb much heat, promoting the evaporation-cooling effect. In addition, as the droplet volume increases, the $T_{diff, max}$ will also increase. For example, when the substrate temperature is 80 °C, the $T_{diff, max}$ will increase by about 17% from 0.5 to 1.5 μL. This is because, with the increase in droplet volume, the distance between the liquid-vapour interface and the substrate also increases, inhibiting heat transfer and making a more significant temperature difference between the top and edge of the interface. Similarly, the changes in $T_{diff, max}$ of MWCNTs and MLG nanofluid droplets under different volumes and substrate temperatures are shown in Fig. 6.7 (d-f) and (g-i), respectively. It can be seen that the $T_{diff, max}$ of carbon-based nanofluid droplets, is still lower than that of DI water. For example, when the substrate temperature is 80 °C and volume is 0.5 μL, the $T_{diff, max}$ of MWCNTs, and MLG nanofluid droplet are 37% and 45% lower than DI water, respectively. This is due to the addition of carbon-based nanoparticles significantly enhancing the droplets' wettability and internal heat conduction, which can effectively suppress the evaporative cooling effect of the liquid-vapour interface and improve its temperature uniformity. Compared with DI water and MWCNTs nanoparticles, adding MLG nanoparticles could make $T_{diff, max}$ with a max reduction of up to 3.7 °C and 1.0 °C, respectively. It means that the addition of MLG nanoparticles will make the effect of inhibiting evaporative cooling more apparent, which can be attributed to MLG nanofluid droplets having better wettability.


(a)
(b)
(c)
(d)
(e)
(f)
(g)
(h)
$T_{gap,\ max}$ (°C)
DI Water 60 °C
DI Water 70 °C
DI Water 80 °C
MWCNTs 60 °C
MWCNTs 70 °C
MWCNTs 80 °C
MLG 60 °C
MLG 70 °C
MLG 80 °C

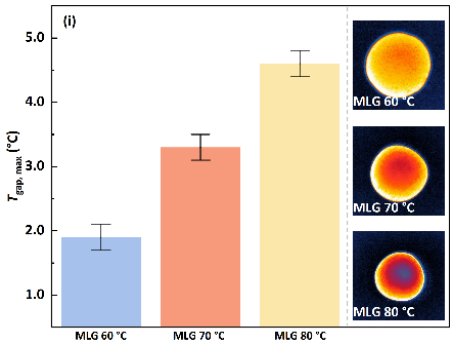
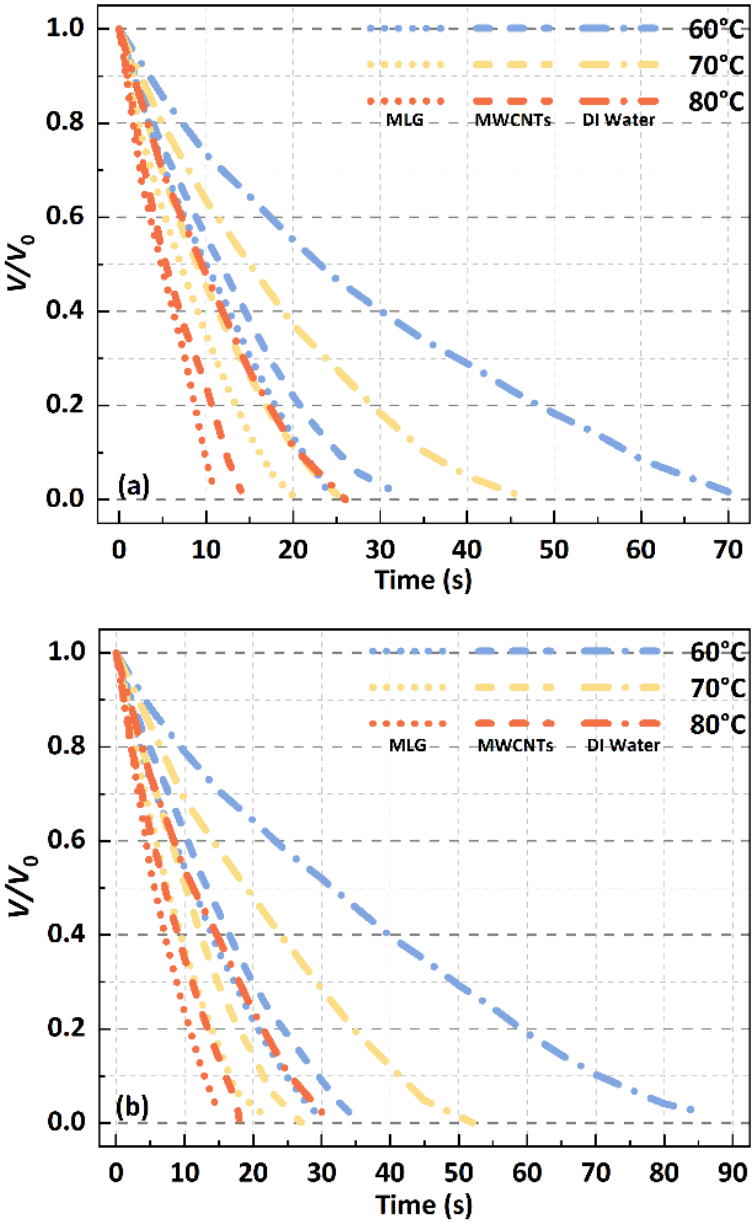


Fig. 6. 7 Based on different substrate temperatures, the maximum temperature difference between the top and edge of (a) 0.5 μL, (b) 1.0 μL, (c) 1.5 μL DI water droplet, (d) 0.5 μL, (e) 1.0 μL, (f) 1.5 μL MWCNTs nanofluid droplet, and (g) 0.5 μL, (h) 1.0 μL, (i) 1.5 μL MLG nanofluid droplet.

At the same time, the change in substrate temperature on the dimensionless volume (V/V_0) of the DI water and carbon-based nanofluid droplets is shown in Fig. 6.8 (a-d). It can be seen from Fig. 6.8 (a) that as the droplet volume is 0.5 μL, the substrate temperature would significantly affect the change of the V/V_0. With the increase in the substrate temperature, the slope of the curve gradually increases, which means that the droplet's evaporation rate also gradually increases. Similarly, when the droplet volume increases to 1.0 μL and 1.5 μL, the changing trend of V/V_0 of the droplets remains consistent, and the effect of temperature on V/V_0 is still pronounced. Moreover, the slope of the V/V_0 curve of the droplets loaded with MLG and MWCNTs is always greater than that of the DI water, indicating that adding carbon-based nanoparticles can significantly enhance evaporation. Meanwhile, the overall average evaporation rate change is shown in Fig. 6.8 (d) under the combined effect of droplet volume and substrate temperature. It can be seen that when the base temperature is 60 °C, 70 °C and 80 °C, the evaporation rate of the MLG-loaded droplets can be increased by up to 1.9, 1.3 and 1.2 times compared with DI water. Besides, the average evaporation rate of MLG nanofluid droplets is always higher than that of MWCNTs nanofluid droplets.

As shown in Fig. 6.8 (d), when the droplet volume is 0.5 μL, the average evaporation rate of MLG nanofluid droplets is 27% higher. When the droplet volume increases to 1.0 and 1.5 μL, this value becomes 20% and 25%, respectively. At the same time, when the substrate temperature increases, the difference in the average evaporation rates of MLG nanofluid droplets and MWCNTs nanofluid droplets becomes more extensive. That is, the enhanced heat transfer effect of MLG nanofluid droplets becomes more evident with the increase of the substrate temperature.



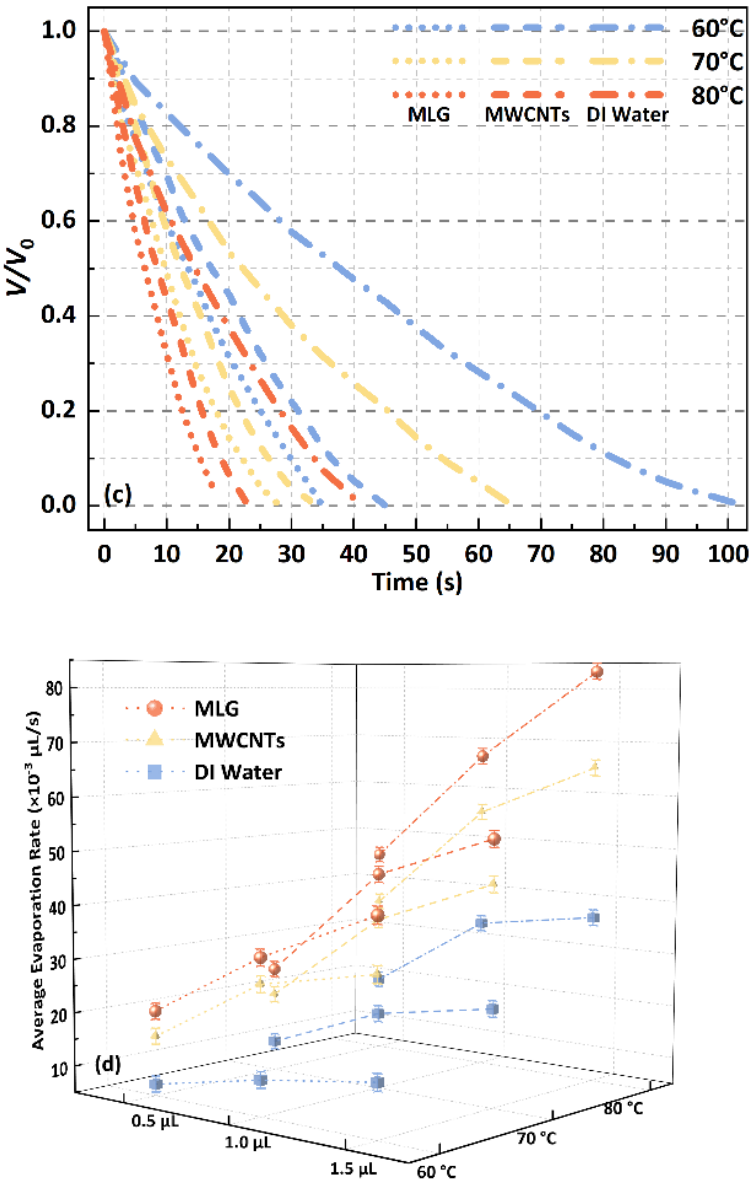


Fig. 6. 8 Dimensionless volume changes under different substrate temperatures of (a) 0.5 μL, (b) 1.0 μL (c) 1.5 μL DI water and carbon-based nanofluid droplets, (d) the average evaporation rate of DI water and carbon-based nanofluid droplets with different volume and temperature conditions.

6.3.3 Macroscopic effects of carbon-based materials on the sedimentary pattern

After evaporation, the nanoparticles loaded in the carbon-based nanofluid droplets will be deposited on the silicon wafer's surface, creating a coffee-ring effect. The sedimentary patterns formed after evaporation of carbon-based nanofluid droplets of

different volumes when the substrate temperature (T_{sub}) is 50 °C are shown in Fig. 6.9. It can be seen from Fig. 6.9 (a-c) that as the droplet volume increases, the area of the sedimentary pattern formed after the MLG nanofluid droplets evaporate also increases. The deposition pattern has an apparent coffee-ring effect. This is because MLG nanofluid droplets mainly follow the CCR evaporation mode during evaporation, so MLG nanoparticles will always accumulate in the contact line area through the Marangoni flows inside the droplet during the evaporation process, which will lead to a noticeable coffee-ring effect. At the same time, it can be seen from Fig. 6.9 (d-f) that the area of the sedimentary pattern formed after the MWCNTs nanofluid droplets evaporate also increases with the increase in droplet volume. However, compared with MLG nanofluid, the coffee ring effect of the deposited pattern is weaker. This phenomenon is because the droplets of MWCNTs nanofluids mainly follow the CCA and Mixed modes during evaporation, making the contact line shrink inward. Then, the loaded MWCNTs nanoparticles are evenly distributed throughout the deposition area through the Marangoni flows.

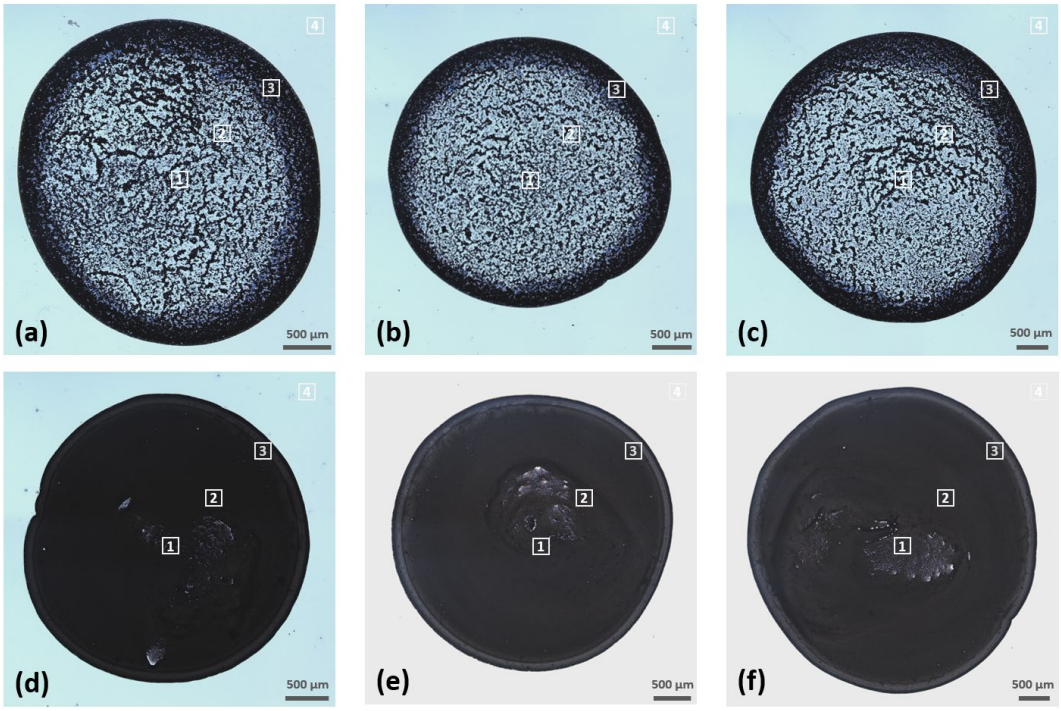


Fig. 6. 9 When the substrate temperature is 50 °C, the sedimentary pattern of (a) 0.5 µL, (b) 1.0 µL, (c) 1.5 µL MLG nanofluid droplets, and (d) 0.5 µL, (e) 1.0 µL; (f) 1.5 µL MWCNTs nanofluid droplets.

In addition, the effect of different nanoparticles on the surface roughness Sa is also shown in Fig. 6.10. At the same time, regions 1 and 2 are located inside the sedimentary pattern, region three near the coffee ring, and region four outside the sedimentary pattern. The comparison between Fig. 6. 10 (a) and (b) shows that the deposition of MLG particles leads to a rougher sedimentary pattern caused by the uneven deposition distribution inside the coffee ring. At the same time, it can be seen from Fig. 6. 10 (a) that in the deposition of MLG nanoparticles, the roughness decreases as it approaches the outside, and the surface roughness of region 3 decreases by an average of 28% compared with regions 1 and 2. Besides, Fig. 6. 10 (b) shows that in the deposition of MWCNT nanoparticles, the roughness in region 2 of the sedimentary pattern is the lowest, and an average of 32% reduces its surface roughness compared with regions 1

and 3.

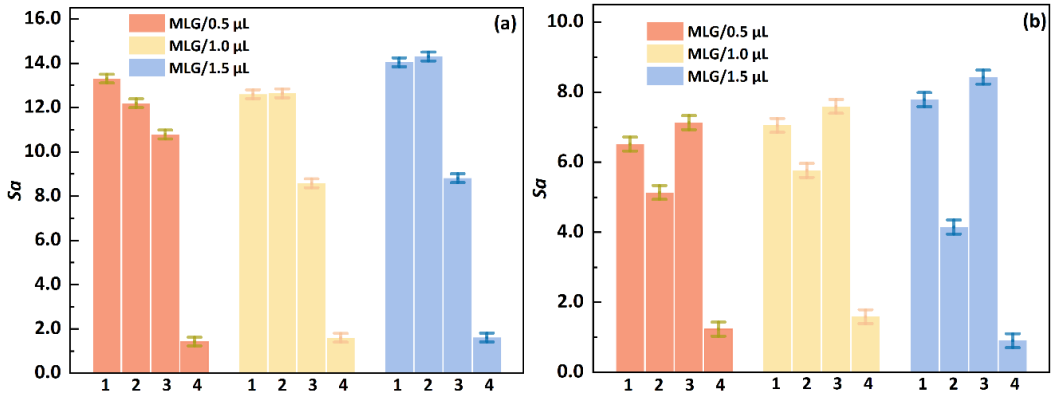


Fig. 6. 10 Effect of the deposition distribution of (a) MWCNTs nanoparticles and (b) MLG nanoparticles on the surface roughness of regions 1-4 under different volume conditions.

In addition, when the substrate temperature is increased from 60 to 80 °C, the sedimentary patterns of carbon-based nanofluid droplets of different volumes are shown in Fig. 6.11. The sedimentary pattern of MLG nanofluid droplets still shows a more apparent coffee-ring effect with increased substrate temperature. From the comparison of Fig. 6.11 (a), (c), and (e), the substrate temperature has no noticeable effect on the sedimentary pattern of MLG nanofluid droplets. However, with the increase in droplet volume, the number of nanoparticles deposited in the central region increases. This may be because as the volume increases, the number of loaded nanoparticles and the total evaporation time also increases, and they will be deposited in the central area based on gravity during the evaporation process. This can be attributed to the fact that as the volume increases, the number of loaded nanoparticles also increases and will be deposited in the central region based on gravity during evaporation. At the same time, from the comparison in Fig. 6.11 (b), (d), and (f), the volume change has no noticeable effect on the sedimentary process of MWCNTs

nanofluid droplets. Still, the change in the substrate temperature will have an impact on the sedimentary pattern. The deposition of MWCNT nanoparticles in the central area becomes lighter when the substrate temperature increases from 60 to 80 °C. This is because as the temperature increases, the duration of the CCA mode becomes shorter, and more nanoparticles accumulate toward the contact line area, which results in less deposition in the central area.

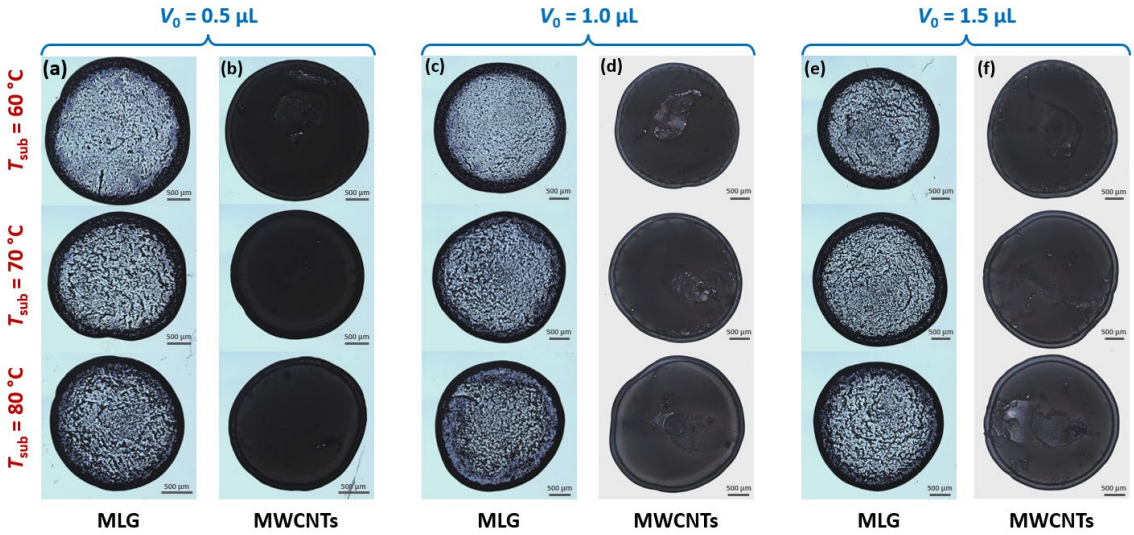


Fig. 6. 11 Under different volume conditions, the sedimentary patterns of MLG nanofluid droplets when the substrate temperature is (a) 60 °C, (c) 70 °C, (e) 80 °C, and the sedimentary patterns of MWCNTs nanofluid droplets when the substrate temperature is (b) 60 °, (d) 70 °C, (f) 80 °C.

In addition, Fig. 6. 12 (a-c) shows the effect of temperature change on the roughness of the sedimentary pattern. It can be seen that when the temperature increases, the average surface roughness in the MWCNTs sedimentary pattern increases slightly. From 60 to 80 ° C in each volume, the average increase in the Sa is about 25%. This phenomenon is caused by the uneven distribution of internal particle deposition caused by the rise in substrate temperature. At the same time, when the temperature increases, the average surface roughness of the MLG sedimentary pattern fluctuates, and the average fluctuation range is about 16% from 60 to 80 ° C in each volume. This shows that the

temperature change has little effect on the roughness distribution of the sedimentary pattern of the MLG droplet. In addition, it can be seen that no matter what the conditions are, the average surface roughness of the non-deposition area constantly fluctuates between 1.0-2.0, and the deposition of MLG particles always causes a greater surface roughness, which increases by about 1.8 times compared with MWCNTs.

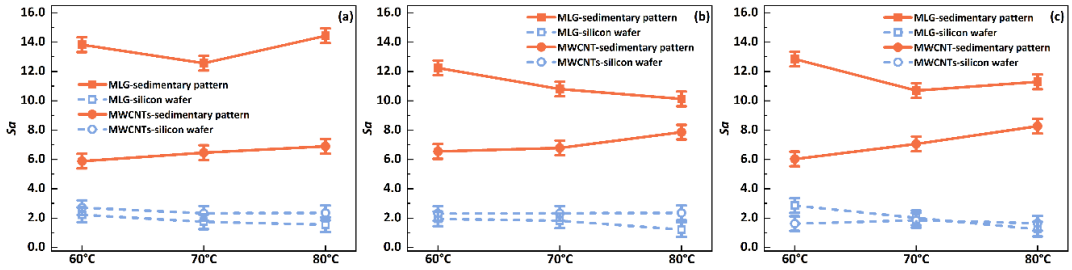


Fig. 6. 12 Variation trend of average surface roughness inside and outside the coffee ring in the deposition pattern of (a) 0.5 μL, (b) 1.0 μL, (c) 1.5 μL droplets under different substrate temperature conditions.

6.4 Chapter summary

This chapter compared the effects of two typical carbon-based nanomaterials, MLG and MWCNTs, on droplet evaporation dynamics with DI water droplets. At the same time, monocrystal silicon is selected as the substrate, and the substrate heating is controlled between 50 °C and 80 °C to better fit the thermal management situation of high heat flux electronic devices such as chips. These results show that adding carbon-based nanoparticles can significantly improve evaporation efficiency by up to 2.1 times compared with pure DI water, effectively enhancing the heat transfer process. At the same time, droplets loaded with MLG nanoparticles have the fastest evaporation

efficiency, owing to the MLG nanoparticles can make the droplets better wettability. At the same time, with the increase of substrate temperature, MLG nanofluid droplets always have a better heat transfer effect. As the substrate temperature increases, the initial contact angle of the carbon-based nanofluid droplets also increases, while that of the DI water droplets decreases slightly. At the same time, the change in substrate temperature has no noticeable effect on the evaporation mode of carbon-based nanofluid droplets. Still, the simultaneous change of droplet volume and substrate temperature significantly affects the jumping behaviour of the DI water droplets. Furthermore, based on various substrate temperatures and droplet volumes, MLG nanoparticles consistently have the best effect of suppressing the evaporative cooling phenomenon, reducing the initial $T_{diff, max}$ by up to 3.7 °C compared to DI water. In addition, after evaporation, the MLG and MWCNTs nanoparticles also had different effects on the sedimentary pattern. The sedimentary pattern of MLG nanofluid droplets showed a noticeable coffee-ring effect, while loaded MWCNTs nanoparticles inhibited the coffee-ring effect. This research will guide industrial applications such as spray cooling and inkjet printing based on carbon-based nanofluids.

Chapter 7. Conclusion and outlook

7.1 Conclusion

To summarise, sessile droplet evaporation continues to be widely applied in physics, chemistry, engineering, and medical research. Simultaneously, although it is a simple phenomenon to observe from the outside, it contains complicated internal physical mechanisms. The research methods also span from the micro-scale to the macro-scale for different research regions, making it more challenging to analyse the evaporation process. Even so, in the past few decades, researchers have put a lot of effort into studying the effect of various influencing factors on the evaporation process of sessile droplets.

According to the objective, this thesis first classified the influencing factors from the perspective of solid and liquid phases. It summarised the latest progress in experimental research on the influence of various factors on the change of droplet interface during evaporation, specifically the influence on evaporation rate, mode and deposition pattern. Therefore, the in-depth exploration of the droplet evaporation mechanism is a systematic problem of multidisciplinary collaborative research. Based on this, this thesis uses experimental research methods to study the influence mechanism of contact interface and liquid characteristics on the evaporation dynamics and deposition pattern of sessile droplets from several perspectives, such as surface roughness, bionic microstructure configuration and loaded nanoparticles. The main research conclusions of this thesis can be summarised as follows:

1. The study not only proves the feasibility of preparing hydrophilic biomimetic functional surfaces directly through photoresist materials and photolithography technology but also shows that by adjusting the structural parameters and arrangement of the surface micro-pillar structure, the wettability of the biomimetic surface can be significantly linearly regulated, thereby effectively affecting the heat and mass transfer process at the droplet liquid-vapour interface. Analysis of the results shows that by controlling the biomimetic surface microstructure, the wettability can be enhanced by about 22% at most, the uniformity of the temperature distribution at the liquid-vapour interface can be improved by about 34%, and the average evaporation rate can be increased by about 28%. This study also demonstrates the feasibility of biomimetic surface design based on photoresist materials.

2. The research results show that, based on the photoresist surface, the transformation of the surface microstructure shape (square or cylindrical) can change the hydrophilicity of the bionic surface. At the same time, the effects of surface microstructure configuration and roughness on the heat and mass transfer process of droplets were also comprehensively studied. The results show that the shape of the bionic microstructure affects the roughness factor, which in turn affects the droplet evaporation dynamics. For example, the biomimetic surface with cylindrical micro-pillars can effectively inhibit the evaporative cooling effect of the liquid-vapour interface. This effect becomes more evident with the increase in roughness, and an average of 18% can reduce the interface temperature difference. Similarly, the biomimetic surface with cylindrical micro-pillars can also effectively promote the evaporation rate of sessile droplets, and the difference is approximately 13%. In addition, the research also shows that

regardless of the structure, substrate temperature changes will significantly impact the wetting phenomenon of the biomimetic surface.

3. The results show that roughness significantly impacts copper surface wettability. As roughness decreases, the evaporation lifetime of silica nanofluid droplets would be prolonged by up to 75%. Increasing the roughness will also increase the temperature of the droplet apex and the temperature difference between the top of the droplet; the contact line area will also be reduced by up to 54%, inhibiting the evaporative cooling effect. Roughness also significantly impacts the deposition pattern of nanofluid droplets. The coffee ring effect is produced on all kinds of surfaces. Still, the coffee ring effect is suppressed as the roughness increases, and the coffee ring deposition has a very small number of fractures on smooth surfaces with more minor roughness. In contrast, on rough surfaces, the number of fractures increases significantly.

4. The experimental results show that droplets loaded with MLG nanoparticles and SDS could significantly improve the evaporation efficiency, which can be improved by up to about 2.1 times compared with DI water. Furthermore, compared with the variable evaporation mode of the DI water droplets, the evaporation process of MLG nanofluid droplets is dominated by constant contact radius mode. At the same time, it can also effectively suppress the evaporative cooling effect. Compared with DI water and MWCNTs, it can reduce the liquid-vapour interface temperature difference by up to 3.7 °C and 1.0 °C, respectively.

7.2 Outlook

Based on the abovementioned, droplet evaporation is a physical process with complex internal mechanisms, so it is necessary to carry out the study using two experimental and numerical simulations, which would make this problem more fully understood. For the experimental study, the equipment currently available in the laboratory can meet the needs of the droplet evaporation experiment. The CCD camera could record the droplet liquid-vapour interface's deformation and the contact line's movement during evaporation. Besides, the IR camera and macro lens also provide the ability to observe the droplet temperature distribution and change during evaporation in this research. In addition, other equipment in the Lab could also provide support to obtain other kinds of experimental conditions, such as heating temperature, surface wettability, inclined substrate, etc. On the other hand, many numerical simulation methods could study the droplet evaporation process. However, the interfacial heat and mass transfer would be the main focus of my research proposal, and the multi-scale issues will be involved if the interface issues have been addressed. Therefore, the LBM (Lattice Boltzmann Method) has been chosen to study the droplet interfacial heat and mass transfer during evaporation. The LBM has the advantage of studying fluid mechanics problems on the mesoscopic scale, which is between the micro and the macro scale and is very suitable for problems such as droplet evaporation. Based on the laboratory conditions and the numerical simulation method, the intrinsic physical mechanism of the droplet evaporation process and the effect of external factors will be studied fully and deeply.

All in all, combined with the aim and objectives proposed during the PhD study, the following research plans would be carried out, and the schedule is also listed:

1. Carry out a study on the influence of surface roughness on the evaporation rate and liquid-vapour interface deformation of the droplet and propose a mathematical model to describe it.

2. Clarify the influence mechanism of surface wettability on the droplet contact line movement and combine the Gibbs free energy principle to propose a more accurate prediction model.

3. Using the LBM to simulate the interfacial heat and mass transfer during droplet evaporation reveals the influence of various external conditions on the evaporation process.

4. Develop the liquid-solid two-phase flow LBM model to simulate the nanofluid droplet evaporation.

Reference

[1] J.C. Maxwell, Collected Scientific Papers. Vol. 1, CUP, 1890.

[2] R.D. Deegan, O. Bakajin, T.F. Dupont, G. Huber, S.R. Nagel, T.A. Witten, Capillary flow as the cause of ring stains from dried liquid drops, Nature, 389 (1997) 827-829.

[3] B. He, A.A. Darhuber, Evaporation of water droplets on photoresist surfaces–An experimental study of contact line pinning and evaporation residues, Colloids and Surfaces A: Physicochemical and Engineering Aspects, 583 (2019) 123912.

[4] S. Khandekar, G. Sahu, K. Muralidhar, E.Y. Gatapova, O.A. Kabov, R. Hu, X. Luo, L. Zhao, Cooling of High-Power LEDs by Liquid Sprays: Challenges and Prospects, Applied Thermal Engineering, (2020) 115640.

[5] A. Gao, J. Yan, Z. Wang, P. Liu, D. Wu, X. Tang, F. Fang, S. Ding, X. Li, J. Sun, Printable CsPbBr 3 perovskite quantum dot ink for coffee ring-free fluorescent microarrays using inkjet printing, Nanoscale, 12 (2020) 2569-2577.

[6] Y.J. Carreón, J. González-Gutiérrez, M. Pérez-Camacho, H. Mercado-Uribe, Patterns produced by dried droplets of protein binary mixtures suspended in water, Colloids and Surfaces B: Biointerfaces, 161 (2018) 103-110.

[7] D. Zhang, B. Gao, C. Zhao, H. Liu, Visualized quantitation of trace nucleic acids based on the coffee-ring effect on colloid-crystal substrates, Langmuir, 35 (2018) 248-253.

[8] S. Shiri, K.F. Martin, J.C. Bird, Surface coatings including fingerprint residues can significantly alter the size and shape of bloodstains, Forensic science international, 295 (2019) 189-198.

[9] W. Feng, E. Ueda, P.A. Levkin, Droplet Microarrays: From Surface Patterning to High-Throughput Applications, Advanced materials, 30 (2018) 1706111.

[10] J. Lim, W. Lee, D. Kwak, K. Cho, Evaporation-induced self-organization of inkjet-printed organic semiconductors on surface-modified dielectrics for high-performance organic transistors, Langmuir, 25 (2009) 5404-5410.

[11] F.S. Ligler, H.S. White, Nanomaterials in analytical chemistry, in, ACS Publications, 2013.

[12] C. Duke, The birth and evolution of surface science: Child of the union of science and technology, Proceedings of the National Academy of Sciences, 100 (2003) 3858-3864.

[13] D. Brutin, V. Starov, Recent advances in droplet wetting and evaporation, Chemical Society Reviews, 47 (2018) 558-585.

[14] T. Young, III. An essay on the cohesion of fluids, Philosophical transactions of the royal society of London, (1805) 65-87.

[15] L.M. de Laplace, Traite de Mecanique Celeste Volume 4, Courcier, Libraire pour les Mathematiques, 1805.

[16] J.L. Plawsky, M. Ojha, A. Chatterjee, P.C. Wayner Jr, Review of the effects of surface topography, surface chemistry, and fluid physics on evaporation at the contact line, Chemical Engineering Communications, 196 (2008) 658-696.

[17] M.R. Gunjan, R. Raj, Dynamic roughness ratio-based framework for modeling mixed mode of droplet evaporation, Langmuir, 33 (2017) 7191-7201.

[18] J. Wang, X. Huang, X. Qiao, D. Ju, C. Sun, Experimental study on effect of support fiber on fuel droplet vaporization at high temperatures, Fuel, 268 (2020) 117407.

[19] D. Mampallil, H.B. Eral, A review on suppression and utilization of the coffee-ring effect, Advances in colloid and interface science, 252 (2018) 38-54.

[20] J. Shi, L. Yang, C.D. Bain, Drying of ethanol/water droplets containing silica

nanoparticles, ACS Applied Materials & Interfaces, 11 (2019) 14275-14285.

[21] N. Kubochkin, J. Venzmer, T. Gambaryan-Roisman, Superspreading and drying of trisiloxane-laden quantum dot nanofluids on hydrophobic surfaces, Langmuir, 36 (2020) 3798-3813.

[22] W. Li, R. Chen, X. Zhu, Q. Liao, D. Ye, Y. Yang, D. Li, Photothermally Caused Propylene Glycol–Water Binary Droplet Evaporation on a Hydrophobic Surface, Industrial & Engineering Chemistry Research, (2021).

[23] X. Shao, F. Duan, Y. Hou, X. Zhong, Role of surfactant in controlling the deposition pattern of a particle-laden droplet: Fundamentals and strategies, Advances in colloid and interface science, 275 (2020) 102049.

[24] D.-O. Kim, A. Rokoni, P. Kaneelil, C. Cui, L.-H. Han, Y. Sun, Role of surfactant in evaporation and deposition of bisolvent biopolymer droplets, Langmuir, 35 (2019) 12773-12781.

[25] M.J. Inanlu, B. Shojaan, J. Farhadi, V. Bazargan, Effect of Particle Concentration on Surfactant-Induced Alteration of the Contact Line Deposition in Evaporating Sessile Droplets, Langmuir, (2021).

[26] T.A. Nguyen, S. Biggs, A. Doi, A.V. Nguyen, A new way of assessing droplet evaporation independently of the substrate hydrophobicity and contact line mode: A case study of sessile droplets with surfactants, Colloids and Surfaces A: Physicochemical and Engineering Aspects, 577 (2019) 396-404.

[27] J.M. Cameron, H.J. Butler, D.S. Palmer, M.J. Baker, Biofluid spectroscopic disease diagnostics: A review on the processes and spectral impact of drying, Journal of biophotonics, 11 (2018) e201700299.

[28] F. Smith, D. Brutin, Wetting and spreading of human blood: Recent advances and

applications, Current Opinion in Colloid & Interface Science, 36 (2018) 78-83.

[29] C. Habchi, V. Ebrahimian, Gravitational effects on multi-component droplet evaporation, Microgravity Science and Technology, 24 (2012) 229-235.

[30] L. Zhao, Y. Qi, P. Luzzatto-Fegiz, Y. Cui, Y. Zhu, COVID-19: effects of environmental conditions on the propagation of respiratory droplets, Nano letters, 20 (2020) 7744-7750.

[31] O. Al-Rawi, M. Wilson, Influence of forced convection on the evaporation and internal dynamics inside of an array of salt solution droplets, in: MATEC Web of Conferences, Vol. 240, EDP Sciences, 2018, pp. 01002.

[32] Y. Pomeau, E. Villermaux, Two hundred years of capillarity research, Physics Today, 59 (2006) 39.

[33] A. Marchand, J.H. Weijs, J.H. Snoeijer, B. Andreotti, Why is surface tension a force parallel to the interface?, American Journal of Physics, 79 (2011) 999-1008.

[34] J.H. Weijs, A. Marchand, B. Andreotti, D. Lohse, J.H. Snoeijer, Origin of line tension for a Lennard-Jones nanodroplet, Physics of fluids, 23 (2011) 022001.

[35] M.E. Shanahan, Simple theory of" stick-slip" wetting hysteresis, Langmuir, 11 (1995) 1041-1043.

[36] E.Y. Bormashenko, Wetting of real surfaces, Walter de Gruyter GmbH & Co KG, 2018.

[37] J.N. Israelachvili, Intermolecular and surface forces, Academic press, 2011.

[38] G.P. Shpenkov, Friction surface phenomena, Elsevier, 1995.

[39] J.-P. Ansermet, S.D. Bréchet, Principles of thermodynamics, Cambridge University Press, 2019.

[40] S. Ip, J. Toguri, The equivalency of surface tension, surface energy and surface

free energy, Journal of materials science, 29 (1994) 688-692.

[41] C. Borgnakke, R.E. Sonntag, Fundamentals of Thermodynamics, 8th Edition, Wiley, 2012.

[42] P.-G. De Gennes, F. Brochard-Wyart, D. Quéré, Capillarity and wetting phenomena: drops, bubbles, pearls, waves, Springer Science & Business Media, 2013.

[43] P.-G. De Gennes, Wetting: statics and dynamics, Reviews of modern physics, 57 (1985) 827.

[44] K. Kern, R. David, R.L. Palmer, G. Comsa, Complete wetting on ‘‘strong’’substrates: Xe/Pt (111), Physical review letters, 56 (1986) 2823.

[45] D. Bonn, J. Eggers, J. Indekeu, J. Meunier, E. Rolley, Wetting and spreading, Reviews of modern physics, 81 (2009) 739.

[46] R.N. Wenzel, Resistance of solid surfaces to wetting by water, Industrial & engineering chemistry, 28 (1936) 988-994.

[47] A. Cassie, S. Baxter, Wettability of porous surfaces, Transactions of the Faraday society, 40 (1944) 546-551.

[48] J. Berthier, P. Silberzan, Microfluidics for biotechnology, Artech House, 2010.

[49] A. Cassie, Contact angles, Discussions of the Faraday society, 3 (1948) 11-16.

[50] A. Marmur, Wetting on hydrophobic rough surfaces: to be heterogeneous or not to be?, Langmuir, 19 (2003) 8343-8348.

[51] T.D. Blake, The physics of moving wetting lines, Journal of Colloid and Interface Science, 299 (2006) 1-13.

[52] C. Huh, L.E. Scriven, Hydrodynamic model of steady movement of a solid/liquid/fluid contact line, Journal of Colloid and Interface Science, 35 (1971) 85-101.

[53] O. Voinov, Hydrodynamics of wetting, Fluid dynamics, 11 (1976) 714-721.

[54] E. Dussan, On the spreading of liquids on solid surfaces: static and dynamic contact lines, Annual Review of Fluid Mechanics, 11 (1979) 371-400.

[55] T. Blake, J. Haynes, Kinetics of liquidliquid displacement, Journal of Colloid and Interface Science, 30 (1969) 421-423.

[56] T.D. BLAKE, Dynamic contact angles and wetting kinetics, Wettability, 251 (1993).

[57] D. Duvivier, D. Seveno, R. Rioboo, T. Blake, J. De Coninck, Experimental evidence of the role of viscosity in the molecular kinetic theory of dynamic wetting, Langmuir, 27 (2011) 13015-13021.

[58] D. Seveno, N. Dinter, J. De Coninck, Wetting dynamics of drop spreading. New evidence for the microscopic validity of the molecular-kinetic theory, Langmuir, 26 (2010) 14642-14647.

[59] M.N. Popescu, G. Oshanin, S. Dietrich, A. Cazabat, Precursor films in wetting phenomena, Journal of Physics: Condensed Matter, 24 (2012) 243102.

[60] A. Hoang, H. Kavehpour, Dynamics of nanoscale precursor film near a moving contact line of spreading drops, Physical review letters, 106 (2011) 254501.

[61] P.G. de Gennes, Soft interfaces: the 1994 Dirac memorial lecture, Cambridge University Press, 2005.

[62] W.B. Hardy, III. The spreading of fluids on glass, The London, Edinburgh, and Dublin Philosophical Magazine and Journal of Science, 38 (1919) 49-55.

[63] R. Picknett, R. Bexon, The evaporation of sessile or pendant drops in still air, Journal of Colloid and Interface Science, 61 (1977) 336-350.

[64] D. Brutin, Droplet wetting and evaporation: from pure to complex fluids,

Academic Press, 2015.

[65] C. Bourges-Monnier, M. Shanahan, Influence of evaporation on contact angle, Langmuir, 11 (1995) 2820-2829.

[66] K.L. Mittal, Contact Angle, Wettability and Adhesion, Volume 6, CRC Press, 2009.

[67] E. Bormashenko, A. Musin, M. Zinigrad, Evaporation of droplets on strongly and weakly pinning surfaces and dynamics of the triple line, Colloids and Surfaces A: Physicochemical and Engineering Aspects, 385 (2011) 235-240.

[68] C. Zhao, C. Kwakernaak, Y. Pan, I. Richardson, Z. Saldi, S. Kenjeres, C. Kleijn, The effect of oxygen on transitional Marangoni flow in laser spot welding, Acta Materialia, 58 (2010) 6345-6357.

[69] H. Zhao, Z. Wang, G. Dong, L. Duan, Fabrication of highly oriented large-scale TIPS pentacene crystals and transistors by the Marangoni effect-controlled growth method, Physical Chemistry Chemical Physics, 17 (2015) 6274-6279.

[70] P. Lee, P. Quested, M. McLean, Modelling of Marangoni effects in electron beam melting, Philosophical Transactions of the Royal Society of London. Series A: Mathematical, Physical and Engineering Sciences, 356 (1998) 1027-1043.

[71] C. Marangoni, Sull'espansione delle goccie d'un liquido galleggianti sulla superfice di altro liquido, Fratelli Fusi, 1865.

[72] A. Nikolov, D. Wasan, J. Lee, Tears of wine: The dance of the droplets, Advances in colloid and interface science, 256 (2018) 94-100.

[73] H. Hu, R.G. Larson, Marangoni effect reverses coffee-ring depositions, The Journal of Physical Chemistry B, 110 (2006) 7090-7094.

[74] R.G. Larson, Re-Shaping the Coffee Ring, Angewandte Chemie International Edition, 51 (2012) 2546-2548.

[75] H.C. Kuhlmann, H.J. Rath, Free Surface Flows, Springer Vienna, 2014.

[76] H. Kuroki, How did Archimedes discover the law of buoyancy by experiment?, Frontiers of Mechanical Engineering, 11 (2016) 26-32.

[77] H.F. Oztop, K. Al-Salem, A review on entropy generation in natural and mixed convection heat transfer for energy systems, Renewable and Sustainable Energy Reviews, 16 (2012) 911-920.

[78] D. Huang, W. Li, A brief review on the buoyancy criteria for supercritical fluids, Applied Thermal Engineering, 131 (2018) 977-987.

[79] S. Dash, A. Chandramohan, J.A. Weibel, S.V. Garimella, Buoyancy-induced on-the-spot mixing in droplets evaporating on nonwetting surfaces, Physical Review E, 90 (2014) 062407.

[80] S. Dash, S.V. Garimella, Droplet evaporation dynamics on a superhydrophobic surface with negligible hysteresis, Langmuir, 29 (2013) 10785-10795.

[81] A. Fick, Ueber diffusion, Annalen der Physik, 170 (1855) 59-86.

[82] J. Li, L. Shan, B. Ma, X. Jiang, A. Solomon, M. Iyengar, J. Padilla, D. Agonafer, Investigation of the confinement effect on the evaporation behavior of a droplet pinned on a micropillar structure, Journal of Colloid and Interface Science, 555 (2019) 583-594.

[83] S.R. Turns, An Introduction to Combustion: Concepts and Applications, McGraw-Hill Education, 2011.

[84] S.S. Sazhin, Advanced models of fuel droplet heating and evaporation, Progress in energy and combustion science, 32 (2006) 162-214.

[85] D. Babenko, A. Dmitriev, I. Mikhailova, Thermohydrodynamic processes of droplet evaporation and boiling on functional nanomaterials surfaces, in: Journal of

Physics: Conference Series, Vol. 1565, IOP Publishing, 2020, pp. 012010.

[86] X. Wang, Z. Liu, L. Wang, Y. Yan, Investigation of droplet evaporation on copper substrate with different roughness, Journal of Bionic Engineering, 17 (2020) 835-842.

[87] S. Feng, J. Delannoy, A. Malod, H. Zheng, D. Quéré, Z. Wang, Tip-induced flipping of droplets on Janus pillars: From local reconfiguration to global transport, Science advances, 6 (2020) eabb4540.

[88] C. Piao, J.E. Winandy, T.F. Shupe, From hydrophilicity to hydrophobicity: A critical review: Part I. Wettability and surface behavior, Wood and Fiber Science, 42 (2010) 490-510.

[89] M. Edalatpour, L. Liu, A. Jacobi, K. Eid, A. Sommers, Managing water on heat transfer surfaces: A critical review of techniques to modify surface wettability for applications with condensation or evaporation, Applied Energy, 222 (2018) 967-992.

[90] Y. Takata, S. Hidaka, J. Cao, T. Nakamura, H. Yamamoto, M. Masuda, T. Ito, Effect of surface wettability on boiling and evaporation, Energy, 30 (2005) 209-220.

[91] E.Y. Gatapova, A.A. Semenov, D.V. Zaitsev, O.A. Kabov, Evaporation of a sessile water drop on a heated surface with controlled wettability, Colloids and Surfaces A: Physicochemical and Engineering Aspects, 441 (2014) 776-785.

[92] S. Misyura, G. Kuznetsov, D. Feoktistov, R. Volkov, V. Morozov, E. Orlova, The influence of the surface microtexture on wettability properties and drop evaporation, Surface and Coatings Technology, 375 (2019) 458-467.

[93] M. Gibbons, P. Di Marco, A. Robinson, Heat flux distribution beneath evaporating hydrophilic and superhydrophobic droplets, International Journal of Heat and Mass Transfer, 148 (2020) 119093.

[94] S. Dash, S.V. Garimella, Droplet evaporation on heated hydrophobic and

superhydrophobic surfaces, Physical Review E, 89 (2014) 042402.

[95] S. Misyura, Heat transfer and convection of evaporating sessile droplets in transition from superhydrophilic to superhydrophobic structured wall: Optimization of functional properties, International Communications in Heat and Mass Transfer, 112 (2020) 104474.

[96] M. Lee, W. Kim, S. Lee, S. Baek, K. Yong, S. Jeon, Water droplet evaporation from sticky superhydrophobic surfaces, Applied Physics Letters, 111 (2017) 021603.

[97] Z. Pan, J.A. Weibel, S.V. Garimella, Transport mechanisms during water droplet evaporation on heated substrates of different wettability, International Journal of Heat and Mass Transfer, 152 (2020) 119524.

[98] Z. Pan, J.A. Weibel, S.V. Garimella, Influence of surface wettability on transport mechanisms governing water droplet evaporation, Langmuir, 30 (2014) 9726-9730.

[99] B. Sobac, D. Brutin, Triple-line behavior and wettability controlled by nanocoated substrates: influence on sessile drop evaporation, Langmuir, 27 (2011) 14999-15007.

[100] X. He, J. Cheng, C.P. Collier, B.R. Srijanto, D.P. Briggs, Evaporation of squeezed water droplets between two parallel hydrophobic/superhydrophobic surfaces, Journal of Colloid and Interface Science, (2020).

[101] S. Kulinich, M. Farzaneh, Effect of contact angle hysteresis on water droplet evaporation from super-hydrophobic surfaces, Applied Surface Science, 255 (2009) 4056-4060.

[102] N. Kashaninejad, N.-T. Nguyen, W.K. Chan, Engineering Micropatterned Surfaces for Controlling the Evaporation Process of Sessile Droplets, Technologies, 8 (2020) 29.

[103] Y.-S. Yu, X. Huang, L. Sun, J.-Z. Zhou, A. Zhou, Evaporation of ethanol/water

mixture droplets on micro-patterned PDMS surfaces, International Journal of Heat and Mass Transfer, 144 (2019) 118708.

[104] M. Gibbons, P. Di Marco, A.J. Robinson, Local heat transfer to an evaporating superhydrophobic droplet, International Journal of Heat and Mass Transfer, 121 (2018) 641-652.

[105] H. Gelderblom, A.G. Marin, H. Nair, A. Van Houselt, L. Lefferts, J.H. Snoeijer, D. Lohse, How water droplets evaporate on a superhydrophobic substrate, Physical Review E, 83 (2011) 026306.

[106] W. Cui, J. Dong, N. Zhao, D. Liang, H. Ma, Sessile Droplet Evaporation on a Structurally Heterogeneous Multiwalled Carbon Nanotube Membrane, Journal of Thermophysics and Heat Transfer, 34 (2020) 150-153.

[107] M. Gao, P. Kong, L.-X. Zhang, J.-N. Liu, An experimental investigation of sessile droplets evaporation on hydrophilic and hydrophobic heating surface with constant heat flux, International Communications in Heat and Mass Transfer, 88 (2017) 262-268.

[108] D. Orejon, K. Sefiane, M.E. Shanahan, Stick–slip of evaporating droplets: substrate hydrophobicity and nanoparticle concentration, Langmuir, 27 (2011) 12834-12843.

[109] H.P. Jansen, H.J. Zandvliet, E.S. Kooij, Evaporation of elongated droplets on chemically stripe-patterned surfaces, International Journal of Heat and Mass Transfer, 82 (2015) 537-544.

[110] T.A. Nguyen, A.V. Nguyen, M.A. Hampton, Z.P. Xu, L. Huang, V. Rudolph, Theoretical and experimental analysis of droplet evaporation on solid surfaces, Chemical engineering science, 69 (2012) 522-529.

[111] M.A. Kadhim, N. Kapur, J.L. Summers, H. Thompson, Experimental and

Theoretical Investigation of Droplet Evaporation on Heated Hydrophilic and Hydrophobic Surfaces, Langmuir, 35 (2019) 6256-6266.

[112] H.-C. Cheng, T.-L. Chang, P.-H. Chen, Experimental investigation of inner bubble dynamics during water droplet evaporation from heated surfaces with different roughness and wettability levels, International Journal of Heat and Mass Transfer, 157 (2020) 119980.

[113] E.W. Washburn, The dynamics of capillary flow, Physical review, 17 (1921) 273.

[114] M. Auliano, D. Auliano, M. Fernandino, P. Asinari, C.A. Dorao, Can Wicking Control Droplet Cooling?, Langmuir, 35 (2019) 6562-6570.

[115] X. Chen, J. Chen, X. Ouyang, Y. Song, R. Xu, P. Jiang, Water droplet spreading and wicking on nanostructured surfaces, Langmuir, 33 (2017) 6701-6707.

[116] S. Poudel, A. Zou, S.C. Maroo, Droplet Evaporation on Porous Nanochannels for High Heat Flux Dissipation, ACS Applied Materials & Interfaces, (2020).

[117] S. Poudel, A. Zou, S.C. Maroo, Evaporation Dynamics in Buried Nanochannels with Micropores, Langmuir, 36 (2020) 7801-7807.

[118] Y. Shang, Y. Hou, M. Yu, S. Yao, Modeling and optimization of condensation heat transfer at biphilic interface, International Journal of Heat and Mass Transfer, 122 (2018) 117-127.

[119] Y. Wang, Z.-g. Wang, Droplets wetting and evaporating on ethanol-philic micro-structured surfaces, International Journal of Heat and Mass Transfer, 119 (2018) 704-708.

[120] M. Hartmann, S. Hardt, Stability of evaporating droplets on chemically patterned surfaces, Langmuir, 35 (2019) 4868-4875.

[121] A. Aboubakri, C. Yanik, Y. Akkuş, A. Koşar, A.K. Sadaghiani, Numerical and

Experimental Investigation on Evaporation of Water Droplet on Surfaces With Mixed Wettability, in: ASME 2020 18th International Conference on Nanochannels, Microchannels, and Minichannels collocated with the ASME 2020 Heat Transfer Summer Conference and the ASME 2020 Fluids Engineering Division Summer Meeting, American Society of Mechanical Engineers Digital Collection, 2020.

[122] X. Chen, R. Ma, J. Li, C. Hao, W. Guo, B.L. Luk, S.C. Li, S. Yao, Z. Wang, Evaporation of droplets on superhydrophobic surfaces: Surface roughness and small droplet size effects, Physical review letters, 109 (2012) 116101.

[123] S. Misyura, Contact angle and droplet heat transfer during evaporation on structured and smooth surfaces of heated wall, Applied Surface Science, 414 (2017) 188-196.

[124] Y. Shen, Y. Cheng, J. Xu, K. Zhang, Y. Sui, Theoretical analysis of sessile evaporating droplet on curved substrate with interfacial cooling effect, Langmuir, (2020).

[125] L. Shan, J. Li, B. Ma, X. Jiang, B. Dogruoz, D. Agonafer, Experimental investigation of evaporation from asymmetric microdroplets confined on heated micropillar structures, Experimental Thermal and Fluid Science, 109 (2019) 109889.

[126] P. Sáenz, A. Wray, Z. Che, O. Matar, P. Valluri, J. Kim, K. Sefiane, Dynamics and universal scaling law in geometrically-controlled sessile drop evaporation, Nature communications, 8 (2017) 1-9.

[127] G. Kuznetsov, D. Feoktistov, E. Orlova, I. Zykov, A. Islamova, Droplet state and mechanism of contact line movement on laser-textured aluminum alloy surfaces, Journal of Colloid and Interface Science, 553 (2019) 557-566.

[128] Z. Wang, K. Lin, Y.-P. Zhao, The effect of sharp solid edges on the droplet

wettability, Journal of Colloid and Interface Science, 552 (2019) 563-571.

[129] M. Kumar, R. Bhardwaj, K.C. Sahu, Wetting Dynamics of a Water Droplet on Micropillar Surfaces with Radially Varying Pitches, Langmuir, 36 (2020) 5312-5323.

[130] J. Lee, S.-H. Hwang, S.-S. Yoon, D.-Y. Khang, Evaporation characteristics of water droplets in Cassie, Wenzel, and mixed states on superhydrophobic pillared Si surface, Colloids and Surfaces A: Physicochemical and Engineering Aspects, 562 (2019) 304-309.

[131] Y. Jiang, Y. Sun, J.W. Drelich, C.-H. Choi, Topography-Dependent Effective Contact Line in Droplet Depinning, Physical review letters, 125 (2020) 184502.

[132] A.J. Petsi, V.N. Burganos, Temperature distribution inside an evaporating two-dimensional droplet lying on curved or flat substrates, Physical Review E, 84 (2011) 011201.

[133] G.G. Wells, É. Ruiz-Gutiérrez, Y. Le Lirzin, A. Nourry, B.V. Orme, M. Pradas, R. Ledesma-Aguilar, Snap evaporation of droplets on smooth topographies, Nature communications, 9 (2018) 1-7.

[134] A. Susarrey-Arce, A. Marin, A. Massey, A. Oknianska, Y. Díaz-Fernandez, J. Hernández-Sánchez, E. Griffiths, J.G. Gardeniers, J.H. Snoeijer, D. Lohse, Pattern formation by staphylococcus epidermidis via droplet evaporation on micropillars arrays at a surface, Langmuir, 32 (2016) 7159-7169.

[135] R.K. Annavarapu, S. Kim, M. Wang, A.J. Hart, H. Sojoudi, Explaining evaporation-triggered wetting transition using local force balance model and contact line-fraction, Scientific reports, 9 (2019) 1-17.

[136] T. Chau, W. Bruckard, P. Koh, A. Nguyen, A review of factors that affect contact angle and implications for flotation practice, Advances in colloid and interface science,

150 (2009) 106-115.

[137] S. Semal, T. Blake, V. Geskin, M.J. De Ruijter, G. Castelein, J. De Coninck, Influence of surface roughness on wetting dynamics, Langmuir, 15 (1999) 8765-8770.

[138] Q. Liu, J. Yu, H. Wang, The role of the substrate roughness in contact angle hysteresis and dynamic deviation, International Journal of Heat and Mass Transfer, 148 (2020) 118985.

[139] Y. Zhang, X. Chen, F. Liu, L. Li, J. Dai, T. Liu, Enhanced coffee-ring effect via substrate roughness in evaporation of colloidal droplets, Advances in Condensed Matter Physics, 2018 (2018).

[140] H. Hu, J.A. Weibel, S.V. Garimella, Role of nanoscale roughness in the heat transfer characteristics of thin film evaporation, International Journal of Heat and Mass Transfer, 150 (2020) 119306.

[141] S.Y. Misyura, The effect of Weber number, droplet sizes and wall roughness on crisis of droplet boiling, Experimental Thermal and Fluid Science, 84 (2017) 190-198.

[142] Y. Shen, Y. Cheng, J. Xu, K. Zhang, Y. Sui, Theoretical analysis of a sessile evaporating droplet on a curved substrate with an interfacial cooling effect, Langmuir, 36 (2020) 5618-5625.

[143] S. David, K. Sefiane, L. Tadrist, Experimental investigation of the effect of thermal properties of the substrate in the wetting and evaporation of sessile drops, Colloids and Surfaces A: Physicochemical and Engineering Aspects, 298 (2007) 108-114.

[144] G. Dunn, S. Wilson, B. Duffy, S. David, K. Sefiane, The strong influence of substrate conductivity on droplet evaporation, Journal of Fluid Mechanics, 623 (2009) 329-351.

[145] Y. Wang, L. Ma, X. Xu, J. Luo, Combined effects of underlying substrate and evaporative cooling on the evaporation of sessile liquid droplets, Soft Matter, 11 (2015) 5632-5640.

[146] K. Gleason, H. Voota, S.A. Putnam, Steady-state droplet evaporation: Contact angle influence on the evaporation efficiency, International Journal of Heat and Mass Transfer, 101 (2016) 418-426.

[147] P. Sáenz, K. Sefiane, J. Kim, O. Matar, P. Valluri, Evaporation of sessile drops: a three-dimensional approach, Journal of Fluid Mechanics, 772 (2015) 705-739.

[148] M.A. Saada, S. Chikh, L. Tadrist, Evaporation of a sessile drop with pinned or receding contact line on a substrate with different thermophysical properties, International Journal of Heat and Mass Transfer, 58 (2013) 197-208.

[149] M.C. Lopes, E. Bonaccurso, T. Gambaryan-Roisman, P. Stephan, Influence of the substrate thermal properties on sessile droplet evaporation: Effect of transient heat transport, Colloids and Surfaces A: Physicochemical and Engineering Aspects, 432 (2013) 64-70.

[150] B. Sobac, D. Brutin, Thermal effects of the substrate on water droplet evaporation, Physical review E, 86 (2012) 021602.

[151] L. Lecoq, D. Flick, O. Laguerre, Study of the water evaporation rate on stainless steel plate in controlled conditions, International Journal of Thermal Sciences, 111 (2017) 450-462.

[152] V. Borodulin, V. Letushko, M. Nizovtsev, A. Sterlyagov, Experimental study of water evaporation of sessile droplets on a solid substrate with different thermal conductivities, in: MATEC Web of Conferences, Vol. 115, EDP Sciences, 2017, pp. 08005.

[153] W. Ristenpart, P. Kim, C. Domingues, J. Wan, H.A. Stone, Influence of substrate conductivity on circulation reversal in evaporating drops, Physical review letters, 99 (2007) 234502.

[154] S.Y. Misyura, V.S. Morozov, Droplet evaporation on a heated structured wall, Thermal Science, 23 (2019) 673-681.

[155] A. Kaushal, V. Jaiswal, V. Mehandia, P. Dhar, Competing advection decelerates droplet evaporation on heated surfaces, arXiv preprint arXiv:2001.04317, (2020).

[156] M. Aleksandrovych, G. Castanet, A. Belarouci, O. Caballina, S. Burian, L. Bulavin, F. Lemoine, D. Lacroix, M. Isaiev, Evaporation of a sessile droplet resting on a thin vanadium dioxide film, in: AIP Conference Proceedings, Vol. 2170, AIP Publishing LLC, 2019, pp. 020001.

[157] M. Gao, D. Zhang, P. Kong, L.-x. Zhang, Experimental investigation of Marangoni convection in a sessile droplet at a constant heat flux condition, International Communications in Heat and Mass Transfer, 115 (2020) 104600.

[158] M. Gao, P. Kong, L.-x. Zhang, Evaporation dynamics of different sizes sessile droplets on hydrophilic and hydrophobic heating surface under constant wall heat fluxes conditions, International Communications in Heat and Mass Transfer, 93 (2018) 93-99.

[159] T.K. Pradhan, P.K. Panigrahi, Thermocapillary convection inside a stationary sessile water droplet on a horizontal surface with an imposed temperature gradient, Experiments in Fluids, 56 (2015) 178.

[160] L. Jiao, R. Chen, X. Zhu, Q. Liao, IR laser caused droplet evaporation on the hydrophobic surface, International Journal of Heat and Mass Transfer, 94 (2016) 180-190.

[161] Z. Liu, Y. Yan, X. Wang, X. Chen, Droplet deposition pattern affected by different heating directions, Journal of Bionic Engineering, 17 (2020) 795-801.

[162] D. Zabiegaj, F. Hajirasouliha, A. Duilio, S. Guido, S. Caserta, M. Kostoglou, M. Petala, T. Karapantsios, A. Trybala, Wetting/Spreading on Porous Media and on Deformable, Soluble Structured Substrates as a Model System for Studying the Effect of Morphology on Biofilms Wetting and for Assessing Anti-Biofilm Methods, Current Opinion in Colloid & Interface Science, (2021) 101426.

[163] O. Arjmandi-Tash, N.M. Kovalchuk, A. Trybala, I.V. Kuchin, V. Starov, Kinetics of wetting and spreading of droplets over various substrates, Langmuir, 33 (2017) 4367-4385.

[164] N.D. Patil, R. Bhardwaj, Recent developments on colloidal deposits obtained by evaporation of sessile droplets on a solid surface, Journal of the Indian Institute of Science, 99 (2019) 143-156.

[165] D. Zang, S. Tarafdar, Y.Y. Tarasevich, M.D. Choudhury, T. Dutta, Evaporation of a Droplet: From physics to applications, Physics Reports, 804 (2019) 1-56.

[166] J.H. Guan, G.G. Wells, B. Xu, G. McHale, D. Wood, J. Martin, S. Stuart-Cole, Evaporation of sessile droplets on slippery liquid-infused porous surfaces (slips), Langmuir, 31 (2015) 11781-11789.

[167] M. Sharma, S.S. Mondal, P.K. Roy, K. Khare, Evaporation dynamics of pure and binary mixture drops on dry and lubricant coated slippery surfaces, Journal of Colloid and Interface Science, 569 (2020) 244-253.

[168] Y. Chen, A. Askounis, V. Koutsos, P. Valluri, Y. Takata, S.K. Wilson, K. Sefiane, On the effect of substrate viscoelasticity on the evaporation kinetics and deposition patterns of nanosuspension drops, Langmuir, 36 (2019) 204-213.

[169] Q.N. Pham, S. Zhang, K. Montazeri, Y. Won, Droplets on Slippery Lubricant-Infused Porous Surfaces: A Macroscale to Nanoscale Perspective, Langmuir, 34 (2018) 14439-14447.

[170] G. Arrabito, V. Ferrara, A. Ottaviani, F. Cavaleri, S. Cubisino, P. Cancemi, Y. Ho, B. Knudsen, M. Hede, C. Pellerito, Imbibition of Femtoliter-Scale DNA-Rich Aqueous Droplets into Porous Nylon Substrates by Molecular Printing, Langmuir, 35 (2019) 17156-17165.

[171] H. Tan, Absorption of picoliter droplets by thin porous substrates, AIChE Journal, 63 (2017) 1690-1703.

[172] H. Zhou, R. Chang, E. Reichmanis, Y. Song, Wetting of inkjet polymer droplets on porous alumina substrates, Langmuir, 33 (2017) 130-137.

[173] F. Fu, P. Li, K. Wang, R. Wu, Numerical simulation of sessile droplet spreading and penetration on porous substrates, Langmuir, 35 (2019) 2917-2924.

[174] J.Y.H. Goh, Y.M. Hung, M.K. Tan, Extraordinarily enhanced evaporation of water droplets on graphene-nanostructured coated surfaces, International Journal of Heat and Mass Transfer, 163 (2020) 120396.

[175] S.U. Choi, J.A. Eastman, Enhancing thermal conductivity of fluids with nanoparticles, in, Argonne National Lab., IL (United States), 1995.

[176] R. Ganvir, P. Walke, V. Kriplani, Heat transfer characteristics in nanofluid—a review, Renewable and Sustainable Energy Reviews, 75 (2017) 451-460.

[177] X. Zhong, A. Crivoi, F. Duan, Sessile nanofluid droplet drying, Advances in colloid and interface science, 217 (2015) 13-30.

[178] Y. Wei, W. Deng, R.-H. Chen, Effects of insoluble nano-particles on nanofluid droplet evaporation, International Journal of Heat and Mass Transfer, 97 (2016) 725-

734.

[179] G.P. Zhu, K.S. Ong, K.S.L. Chong, J.F. Yao, H.L. Huang, F. Duan, Evaporative characteristics of sessile nanofluid droplet on micro-structured heated surface, Electrophoresis, 40 (2019) 845-850.

[180] R. Wang, G. Pan, S. Qian, L. Li, Z. Zhu, Influence of nanoparticles on the evaporation behavior of nanofluid droplets: A Dh law and underlying mechanism, Langmuir, 36 (2019) 919-930.

[181] K. Sefiane, R. Bennacer, Nanofluids droplets evaporation kinetics and wetting dynamics on rough heated substrates, Advances in colloid and interface science, 147 (2009) 263-271.

[182] D.H. Shin, C.K. Choi, Y.T. Kang, S.H. Lee, Local aggregation characteristics of a nanofluid droplet during evaporation, International Journal of Heat and Mass Transfer, 72 (2014) 336-344.

[183] I. Zaaroura, S. Harmand, J. Carlier, M. Toubal, A. Fasquelle, B. Nongaillard, Experimental studies on evaporation kinetics of gold nanofluid droplets: Influence of nanoparticle sizes and coating on thermal performance, Applied Thermal Engineering, 183 116180.

[184] J.-Z. Jiang, S. Zhang, X.-L. Fu, L. Liu, B.-M. Sun, Microscopic experimental study of nanoparticle motion for droplet evaporation enhancement in nanofluids, International Communications in Heat and Mass Transfer, 119 (2020) 104948.

[185] R.-H. Chen, T.X. Phuoc, D. Martello, Effects of nanoparticles on nanofluid droplet evaporation, International Journal of Heat and Mass Transfer, 53 (2010) 3677-3682.

[186] P. Chen, S. Harmand, S. Szunerits, R. Boukherroub, Evaporation behavior of

PEGylated graphene oxide nanofluid droplets on heated substrate, International Journal of Thermal Sciences, 135 (2019) 445-458.

[187] J. Xu, X. Yan, G. Liu, J. Xie, The critical nanofluid concentration as the crossover between changed and unchanged solar-driven droplet evaporation rates, Nano Energy, 57 (2019) 791-803.

[188] X. Yan, J. Xu, Z. Meng, J. Xie, A comprehensive comparison between substrate heating and light heating induced nanofluid droplet evaporations, Applied Thermal Engineering, (2020) 115389.

[189] F.R. Siddiqui, C.Y. Tso, S.C. Fu, H. Qiu, C.Y. Chao, Evaporation and wetting behavior of silver-graphene hybrid nanofluid droplet on its porous residue surface for various mixing ratios, International Journal of Heat and Mass Transfer, 153 (2020) 119618.

[190] S.K. Saroj, P.K. Panigrahi, Drying pattern and evaporation dynamics of sessile ferrofluid droplet on a PDMS substrate, Colloids and Surfaces A: Physicochemical and Engineering Aspects, 580 (2019) 123672.

[191] Y.C. Kim, Evaporation of nanofluid droplet on heated surface, Advances in Mechanical Engineering, 7 (2015) 1687814015578358.

[192] J. Ren, X. Zhong, L. Shen, F. Duan, Hydrodynamic pattern in drying saline droplet with suspended nanoparticles, Journal of Bionic Engineering, 17 (2020) 802-808.

[193] J.R. Moffat, K. Sefiane, M.E. Shanahan, Effect of TiO2 nanoparticles on contact line stick− slip behavior of volatile drops, The Journal of Physical Chemistry B, 113 (2009) 8860-8866.

[194] Y. Yamada, A. Horibe, Discontinuous contact line motion of evaporating particle-

laden droplet on superhydrophobic surfaces, Physical Review E, 97 (2018) 043113.

[195] D. Brutin, Influence of relative humidity and nano-particle concentration on pattern formation and evaporation rate of pinned drying drops of nanofluids, Colloids and Surfaces A: Physicochemical and Engineering Aspects, 429 (2013) 112-120.

[196] X. Yan, J. Xu, Z. Meng, J. Xie, G. Liu, Multiscale Characteristic in Symmetric/Asymmetric Solar-Driven Nanofluid Droplet Evaporation, Langmuir, 36 (2020) 1680-1690.

[197] B. Liu, S. Wang, L. Chai, G. El Achkar, A. Chen, P.E. Theodorakis, Experimental investigation of nanoparticles distribution mechanisms and deposition patterns during nanofluid droplet evaporation, The European Physical Journal Applied Physics, 92 (2020) 11101.

[198] J.R. Moffat, K. Sefiane, M.E. Shanahan, Nanofluid droplet evaporation kinetics and wetting dynamics on flat substrates, in: Journal of Nano Research, Vol. 7, Trans Tech Publ, 2009, pp. 75-80.

[199] A. Aboalhamayie, L. Festa, M. Ghamari, Evaporation rate of colloidal droplets of jet fuel and carbon-based nanoparticles: Effect of thermal conductivity, Nanomaterials, 9 (2019) 1297.

[200] K. Sakamoto, R. Lochhead, H. Maibach, Y. Yamashita, Cosmetic science and technology: theoretical principles and applications, Elsevier, 2017.

[201] M. Ahmadi, Q. Hou, Y. Wang, Z. Chen, Interfacial and molecular interactions between fractions of heavy oil and surfactants in porous media: Comprehensive review, Advances in colloid and interface science, (2020) 102242.

[202] A.A. Siyal, M.R. Shamsuddin, A. Low, N.E. Rabat, A review on recent developments in the adsorption of surfactants from wastewater, Journal of

environmental management, 254 (2020) 109797.

[203] Y. Moroi, M. Rusdi, I. Kubo, Difference in surface properties between insoluble monolayer and adsorbed film from kinetics of water evaporation and BAM image, The Journal of Physical Chemistry B, 108 (2004) 6351-6358.

[204] K. Lunkenheimer, M. Zembala, Attempts to study a water evaporation retardation by soluble surfactants, Journal of Colloid and Interface Science, 188 (1997) 363-371.

[205] G. Gutiérrez, J.M. Benito, J. Coca, C. Pazos, Vacuum evaporation of surfactant solutions and oil-in-water emulsions, Chemical Engineering Journal, 162 (2010) 201-207.

[206] X. Fang, A.B. Páhi, H. Li, P. Somasundaran, Enhancement of water transport through the liquid–vapor interface by surfactants, Soft Matter, 8 (2012) 8959-8964.

[207] K. Birdi, D. Vu, Wettability and the evaporation rates of fluids from solid surfaces, Journal of adhesion science and technology, 7 (1993) 485-493.

[208] S. Chandra, M. Di Marzo, Y. Qiao, P. Tartarini, Effect of liquid-solid contact angle on droplet evaporation, Fire safety journal, 27 (1996) 141-158.

[209] Z. Zhou, C. Cao, L. Cao, L. Zheng, J. Xu, F. Li, Q. Huang, Effect of surfactant concentration on the evaporation of droplets on cotton (Gossypium hirsutum L.) leaves, Colloids and Surfaces B: Biointerfaces, 167 (2018) 206-212.

[210] S.J. Gokhale, J.L. Plawsky, P.C. Wayner, Spreading, evaporation, and contact line dynamics of surfactant-laden microdrops, Langmuir, 21 (2005) 8188-8197.

[211] G.M. Kontogeorgis, S. Kiil, Introduction to applied colloid and surface chemistry, Wiley Online Library, 2016.

[212] S. Semenov, A. Trybala, H. Agogo, N. Kovalchuk, F. Ortega, R.n.G. Rubio, V.M. Starov, M.G. Velarde, Evaporation of droplets of surfactant solutions, Langmuir, 29

(2013) 10028-10036.

[213] A. Marin, R. Liepelt, M. Rossi, C.J. Kähler, Surfactant-driven flow transitions in evaporating droplets, Soft Matter, 12 (2016) 1593-1600.

[214] K. Sefiane, The coupling between evaporation and adsorbed surfactant accumulation and its effect on the wetting and spreading behaviour of volatile drops on a hot surface, Journal of Petroleum Science and Engineering, 51 (2006) 238-252.

[215] Y. Gong, J. Xu, R.C. Buchanan, Surface roughness: A review of its measurement at micro-/nano-scale, Physical Sciences Reviews, 3 (2018) 20170057.

[216] B. Bhushan, Biomimetics inspired surfaces for drag reduction and oleophobicity/philicity, Beilstein journal of nanotechnology, 2 (2011) 66-84.

[217] C. Li, J. Yang, W. He, M. Xiong, X. Niu, X. Li, D.G. Yu, A review on fabrication and application of tunable hybrid micro–nano array surfaces, Advanced Materials Interfaces, 10 (2023) 2202160.

[218] J.E. Park, S. Won, W. Cho, J.G. Kim, S. Jhang, J.G. Lee, J.J. Wie, Fabrication and applications of stimuli-responsive micro/nanopillar arrays, Journal of Polymer Science, 59 (2021) 1491-1517.

[219] C. Hao, Y. Liu, X. Chen, J. Li, M. Zhang, Y. Zhao, Z. Wang, Bioinspired interfacial materials with enhanced drop mobility: From fundamentals to multifunctional applications, Small, 12 (2016) 1825-1839.

[220] X. Yang, W. Zhang, X. Qin, M. Cui, Y. Guo, T. Wang, K. Wang, Z. Shi, C. Zhang, W. Li, Recent progress on bioinspired antibacterial surfaces for biomedical application, Biomimetics, 7 (2022) 88.

[221] B. Zhang, W. Xu, L. Peng, Y. Li, W. Zhang, Z. Wang, Nature-inspired interfacial engineering for energy harvesting, Nature Reviews Electrical Engineering, (2024) 1-

16.

[222] S.K. Mitra, S. Chakraborty, Microfluidics and nanofluidics handbook: fabrication, implementation, and applications, Taylor & Francis, 2012.

[223] C.J. Van Oss, Interfacial forces in aqueous media, CRC press, 2006.

[224] J. Berthier, Micro-drops and digital microfluidics, William Andrew, 2012.

[225] C.S. Buga, J.C. Viana, A review on materials and technologies for organic large-area electronics, Advanced Materials Technologies, 6 (2021) 2001016.

[226] C. Luo, C. Xu, L. Lv, H. Li, X. Huang, W. Liu, Review of recent advances in inorganic photoresists, RSC advances, 10 (2020) 8385-8395.

[227] S. Li, Y. Fan, Y. Liu, S. Niu, Z. Han, L. Ren, Smart bionic surfaces with switchable wettability and applications, Journal of Bionic Engineering, 18 (2021) 473-500.

[228] G. Liu, Z. Yuan, Z. Qiu, S. Feng, Y. Xie, D. Leng, X. Tian, A brief review of bio-inspired surface technology and application toward underwater drag reduction, Ocean Engineering, 199 (2020) 106962.

[229] T. Sun, L. Feng, X. Gao, L. Jiang, Bioinspired surfaces with special wettability, Accounts of chemical research, 38 (2005) 644-652.

[230] H. Shahsavan, D. Arunbabu, B. Zhao, Biomimetic modification of polymeric surfaces: A promising pathway for tuning of wetting and adhesion, Macromolecular Materials and Engineering, 297 (2012) 743-760.

[231] X. Gou, Z. Guo, Surface topographies of biomimetic superamphiphobic materials: design criteria, fabrication and performance, Advances in colloid and interface science, 269 (2019) 87-121.

[232] Y. Sun, Z. Guo, Recent advances of bioinspired functional materials with specific wettability: from nature and beyond nature, Nanoscale Horizons, 4 (2019) 52-76.

[233] A.P. Johnson, C. Sabu, K. Nivitha, R. Sankar, V.A. Shirin, T. Henna, V. Raphey, H. Gangadharappa, S. Kotta, K. Pramod, Bioinspired and biomimetic micro-and nanostructures in biomedicine, Journal of Controlled Release, 343 (2022) 724-754.

[234] H. Yu, J. Zhang, S. Zhang, Z. Han, Bionic structures and materials inspired by plant leaves: A comprehensive review for innovative problem-solving, Progress in Materials Science, (2023) 101181.

[235] E. Arzt, H. Quan, R.M. McMeeking, R. Hensel, Functional surface microstructures inspired by nature–From adhesion and wetting principles to sustainable new devices, Progress in Materials Science, 120 (2021) 100823.

[236] T. Xiang, J. Hou, H. Xie, X. Liu, T. Gong, S. Zhou, Biomimetic micro/nano structures for biomedical applications, Nano Today, 35 (2020) 100980.

[237] Z. Wang, D. Orejon, Y. Takata, K. Sefiane, Wetting and evaporation of multicomponent droplets, Physics Reports, 960 (2022) 1-37.

[238] P. Gurrala, S. Balusamy, S. Banerjee, K.C. Sahu, A review on the evaporation dynamics of sessile drops of binary mixtures: Challenges and opportunities, Fluid Dyn. Mater. Process, 17 (2021) 253-284.

[239] Y.T. Aksoy, Y. Zhu, P. Eneren, E. Koos, M.R. Vetrano, The impact of nanofluids on droplet/spray cooling of a heated surface: A critical review, Energies, 14 (2020) 80.

[240] G. Gold, K. Helmreich, A physical surface roughness model and its applications, IEEE Transactions on Microwave Theory and Techniques, 65 (2017) 3720-3732.

[241] A.A. Albert, H.S. DG, P. V, Review of stability enhanced nanofluids prepared by one-step methods—heat transfer mechanism and thermo-physical properties, Chemical Engineering Communications, 210 (2023) 1822-1852.

[242] R.K. Mudidana, V. Miditana, V. Rambabu, Synthesis of nanofluids preparation–

A review, Materials Today: Proceedings, (2023).

[243] J. Wang, X. Yang, J.J. Klemeš, K. Tian, T. Ma, B. Sunden, A review on nanofluid stability: preparation and application, Renewable and Sustainable Energy Reviews, 188 (2023) 113854.

[244] M. Bhuiyan, R. Saidur, M. Amalina, R. Mostafizur, A. Islam, Effect of nanoparticles concentration and their sizes on surface tension of nanofluids, Procedia Engineering, 105 (2015) 431-437.

[245] A. Kujawska, R. Mulka, S. Hamze, G. Żyła, B. Zajaczkowski, M.H. Buschmann, P. Estellé, The effect of boiling in a thermosyphon on surface tension and contact angle of silica and graphene oxide nanofluids, Colloids and Surfaces A: Physicochemical and Engineering Aspects, 627 (2021) 127082.

[246] X. He, J. Cheng, C.P. Collier, B.R. Srijanto, D.P. Briggs, Evaporation of squeezed water droplets between two parallel hydrophobic/superhydrophobic surfaces, Journal of colloid and Interface Science, 576 (2020) 127-138.

[247] H. Gelderblom, C. Diddens, A. Marin, Evaporation-driven liquid flow in sessile droplets, Soft matter, (2022).

[248] R. Mulka, A. Kujawska, B. Zajączkowski, S. Mancin, M. Buschmann, Drying silica-nanofluid droplets, Colloids and Surfaces A: Physicochemical and Engineering Aspects, 623 (2021) 126730.

[249] M.A. Hampton, T.A. Nguyen, A.V. Nguyen, Z.P. Xu, L. Huang, V. Rudolph, Influence of surface orientation on the organization of nanoparticles in drying nanofluid droplets, Journal of colloid and Interface Science, 377 (2012) 456-462.

[250] X.-Y. Yang, G.-H. Li, X. Huang, Y.-S. Yu, Evaporative deposition of surfactant-laden nanofluid droplets over a silicon surface, Langmuir, 38 (2022) 11666-11674.

[251] N. Jain, E. Gupta, N.J. Kanu, Plethora of Carbon nanotubes applications in various fields–A state-of-the-art-review, Smart Science, 10 (2022) 1-24.

[252] A. Razaq, F. Bibi, X. Zheng, R. Papadakis, S.H.M. Jafri, H. Li, Review on graphene-, graphene oxide-, reduced graphene oxide-based flexible composites: From fabrication to applications, Materials, 15 (2022) 1012.

[253] H.W. Tan, Y.Y.C. Choong, C.N. Kuo, H.Y. Low, C.K. Chua, 3D printed electronics: Processes, materials and future trends, Progress in Materials Science, 127 (2022) 100945.

[254] W. Li, C. Zhang, D. Lan, W. Ji, Y. Wang, Solution Printing of Electronics and Sensors: Applicability and Application in Space, Advanced Engineering Materials, 24 (2022) 2200173.

[255] H. Abdolmaleki, P. Kidmose, S. Agarwala, Droplet-based techniques for printing of functional inks for flexible physical sensors, Advanced Materials, 33 (2021) 2006792.

[256] Z. Han, A. Fina, Thermal conductivity of carbon nanotubes and their polymer nanocomposites: A review, Progress in polymer science, 36 (2011) 914-944.

[257] S. Ghosh, W. Bao, D.L. Nika, S. Subrina, E.P. Pokatilov, C.N. Lau, A.A. Balandin, Dimensional crossover of thermal transport in few-layer graphene, Nature materials, 9 (2010) 555-558.

[258] K.M. Al Balushi, G. Duursma, P. Valluri, K. Sefiane, D. Orejon, Binary mixture droplet evaporation on microstructured decorated surfaces and the mixed stick–slip modes, Langmuir, 39 (2023) 8323-8338.